

# A study on wide bandgap oxide semiconductors



March 2017

Department of Science and Advanced Technology  
Graduate School of Science and Engineering  
Saga University

Xu WANG



# **A study on wide bandgap oxide semiconductors**

## **Abstract**

In recent years, wide bandgap oxide semiconductor has attracted considerable attention owing to its application in ultraviolet (UV) optoelectronic devices, especially in deep UV light emitters and detectors, due to their potential application in Ozone hole detection, chemical-biological agent sensors, missile plume sensors and space-to-space communications. Among all the wide bandgap oxide semiconductors, MgZnO alloy films are ideal materials for developing the UV optoelectronic devices because of their particular advantages, such as wide bandgap, low growth temperature, availability of lattice-matched single-crystal substrates, and high radiation hardness.

Since the ionic radius of  $\text{Mg}^{2+}$  (0.057 nm) is similar to that of  $\text{Zn}^{2+}$  (0.060 nm), there can be some replacement in either structure without changing the original structure when alloying. However, there is large crystal structure dissimilarity between wurtzite hexagonal ZnO and rock-salt-cubic MgO, which leads to phase separation. It limited the application of MgZnO alloy in deep UV region. In comparison with ZnO semiconductor,  $\text{Ga}_2\text{O}_3$  has a wider bandgap of about 4.9 eV. The bandgap of In-Al-Ga-O system which is obtained by alloying In or Al element into  $\text{Ga}_2\text{O}_3$  can be tuned from 3.5-8.6 eV, thus In-Al-Ga-O system can be used as deep UV light-emitting diode, deep UV detector, and deep UV transparent electrode.

In Chapter 1, the review of studies on the wide bandgap oxide semiconductors were

described. The purpose of this study was also presented.

In Chapter 2, film growth and characterization methods were introduced.

In Chapter 3, the influence of Mg content on crystal structure and properties of single phase MgZnO films grown in all Mg content was been discussed. The structural transition from hexagonal to cubic phase has been observed at the Mg content around 0.4. We have also investigated the effect of the substrate temperature and oxygen pressure on crystal structure and properties of MgZnO films grown by using pulsed laser deposition (PLD) method.

In Chapter 4, we reported on bandgap bowing parameters for wurtzite and cubic MgZnO alloys from a study of high quality and single phase films in all Mg content range. The Mg contents in the MgZnO films were accurately determined using the Energy dispersive spectrometer and X-ray photoelectron spectroscopy (XPS). The measurement of bandgap energies by examining the onset of inelastic energy loss in core-level atomic spectra from XPS was proved to be valid for determining the bandgap of MgZnO films. The dependence of the energy bandgap on Mg content was found to deviate downwards from linearity. Fitting of the bandgap energies resulted in two bowing parameters of 2.01 and 1.48 eV corresponding to wurtzite and cubic MgZnO films, respectively.

In Chapter 5, (1) (AlGa)<sub>2</sub>O<sub>3</sub> thin films were deposited on (0001) sapphire substrates by PLD at different substrate temperatures. The influence of substrate temperature on surface morphology, optical properties, and crystal quality has been systematically investigated by atomic force microscope, transmission spectra, X-ray diffraction, and

Raman spectroscopy. The results revealed that all the  $(\text{AlGa})_2\text{O}_3$  films had smooth surface and high transmittance. The  $(\text{AlGa})_2\text{O}_3$  film with the better crystal quality can be obtain at a substrate temperature of 400 °C. (2) We also report a detailed investigation on temperature-dependent Raman scattering of  $\beta$ - $(\text{AlGa})_2\text{O}_3$  thin films with different Al content (0-0.72) under the temperature range of 77-300 K. The temperature-dependent Raman shifts and linewidths of the phonon modes were obtained by employing Lorentz fitting. The linewidths broadening of phonon modes with the temperature can be well explained by a model involving the effects of thermal expansion, lattice-mismatch-induced strain, and decay of optical phonon into two and three phonons. It is clearly demonstrated dependence of the linewidths and decay process on the Al content in  $\beta$ - $(\text{AlGa})_2\text{O}_3$  thin films.

In Chapter 6, we reported measurements of Raman scattering of cubic  $\text{In}_2\text{O}_3$  and  $(\text{In}_{0.83}\text{Ga}_{0.17})_2\text{O}_3$  films grown on sapphire substrates by PLD as a function of temperature (77-500 K). We analyzed the temperature-dependent Raman shifts and linewidths of six Raman modes in  $\text{In}_2\text{O}_3$  film and  $A_g^{(1)}$  and  $A_g^{(2)}/T_g^{(2)}$  modes in  $(\text{In}_{0.83}\text{Ga}_{0.17})_2\text{O}_3$  film. The Raman shifts of phonon modes were found to vary linearly with temperature. The temperature coefficients for six Raman modes of  $\text{In}_2\text{O}_3$  film were in the range of -0.014 and -0.006  $\text{cm}^{-1}/\text{K}$ , while temperature coefficients of  $A_g^{(1)}$  and  $A_g^{(2)}/T_g^{(2)}$  modes in  $(\text{In}_{0.83}\text{Ga}_{0.17})_2\text{O}_3$  film were -0.017 and -0.024  $\text{cm}^{-1}/\text{K}$ , respectively. Through the aid of a model involving three- and four-phonon coupling, the effects of temperature on linewidths were clearly illustrated, which demonstrated that three-phonon process always dominated in the decay process for all the modes in

both  $\text{In}_2\text{O}_3$  and  $(\text{In}_{0.83}\text{Ga}_{0.17})_2\text{O}_3$  films.

# Contents

<b>1 Introduction.....</b>	<b>1</b>
1.1 Background.....	1
1.2 Review of study on wide bandgap oxide semiconductor.....	2
1.2.1 Group II oxides.....	2
1.2.2 Group III oxides.....	11
1.3 Purpose and Outline.....	19
References.....	23
<b>2 Growth and characterization methods.....</b>	<b>29</b>
2.1 PLD.....	29
2.2 Characterization method.....	34
<b>3 Growth and characterization of MgZnO films.....</b>	<b>40</b>
3.1 Mg content influence.....	40
3.2 Substrate temperature influence.....	50
3.3 Oxygen pressure influence.....	59
3.4 Conclusions.....	62
References.....	63
<b>4 Bandgap engineering of Mg<sub>x</sub>Zn<sub>1-x</sub>O films.....</b>	<b>65</b>

4.1 Introduction.....	65
4.2 Experiment.....	67
4.3 Results and discussion.....	68
4.4 Conclusions.....	75
References.....	76
<b>5 Raman scattering in <math>(Al_xGa_{1-x})_2O_3</math> films.....</b>	<b>78</b>
5.1 Substrate temperature effect.....	78
5.2 Raman scattering.....	91
5.3 Conclusions.....	107
References.....	109
<b>6 Raman scattering in <math>(In_xGa_{1-x})_2O_3</math> films.....</b>	<b>113</b>
6.1 Introduction.....	113
6.2 Experiment.....	114
6.3 Results and discussion.....	115
6.4 Conclusions.....	127
References.....	128
<b>7 Summary.....</b>	<b>131</b>
Acknowledgments.....	134
List of publications.....	135

# Chapter 1

## Introduction

### 1.1 Background

With the increase in demand for ultraviolet (UV) optoelectronic devices, piezoelectric sensors, power device application, and thin film transistors, wide bandgap oxide semiconductors become the hot spot of recent research due to their particular properties such as wide bandgap, high conductivity, and high transmittance. In addition, they can be easily prepared by common methods such as pulsed laser deposition (PLD), molecular beam epitaxy (MBE), magnetron sputtering, and metal-organic chemical vapor deposition (MOCVD).

Figure 1.1 is a comparison of the bandgap energies and lattice constants ( $a$ ) of wide bandgap oxide semiconductors and other well-known oxide semiconductors. The two main types of wide bandgap oxide semiconductors are: (1) Group II oxides such as ZnO and MgO, (2) Group III oxides such as Ga<sub>2</sub>O<sub>3</sub>, Al<sub>2</sub>O<sub>3</sub>, and In<sub>2</sub>O<sub>3</sub>. The bandgap engineering is an indispensable issue to be achieved for developing these applications. For Group II oxides, alloying ZnO with MgO can tune the bandgap from 3.31 eV to 7.8 eV. MgZnO alloy material has received much attention due to their potential applications in the short-wavelength optoelectronic devices such as UV light-emitting diodes and laser diodes. For Group III oxides, the bandgap of In-Al-Ga-O system which is obtained by alloying In or Al element into Ga<sub>2</sub>O<sub>3</sub> can be tuned from 3.5-8.6 eV, thus In-Al-Ga-O system can be used as deep UV light-emitting diode, deep UV

detector, and deep UV transparent electrode.

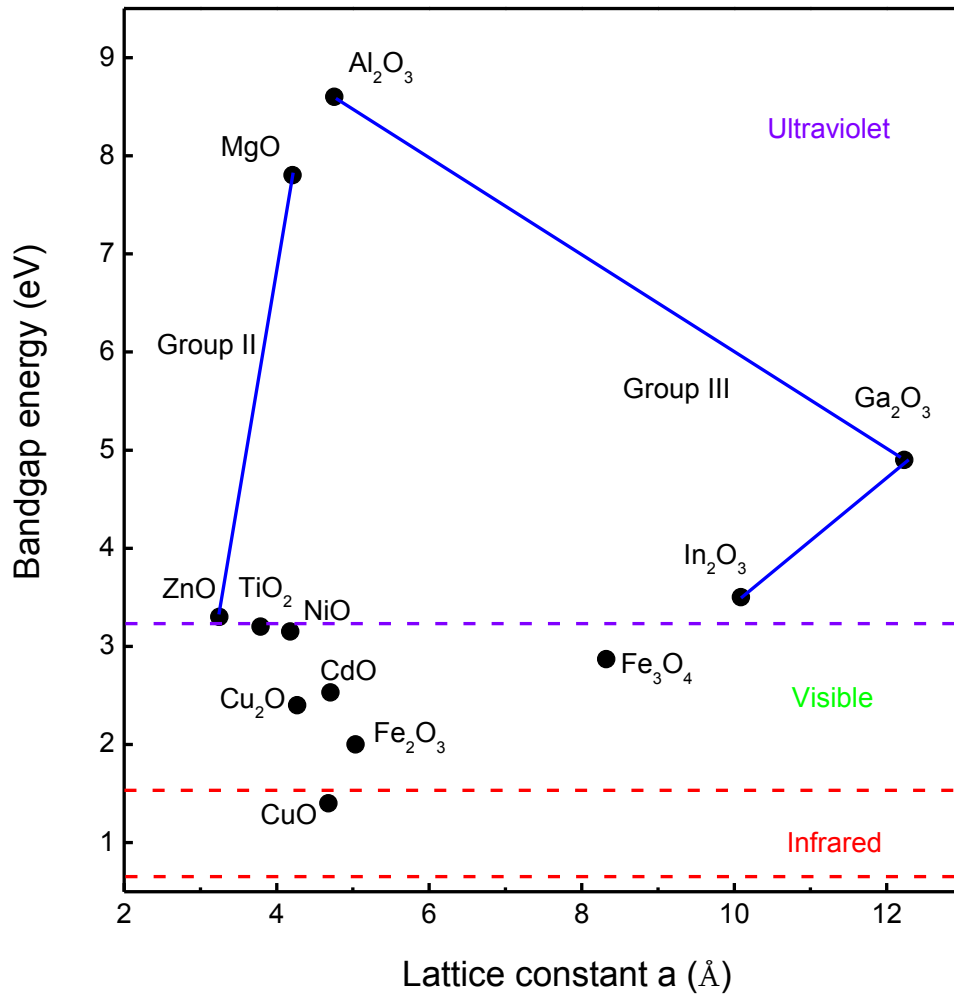


Figure 1.1 The relationship between energy bandgap and lattice constant ( $a$ ) of oxide semiconductors.

## 1.2 Review of study on wide bandgap oxide semiconductor

### 1.2.1 Group II oxides

#### (1) ZnO

Owing to its direct wide bandgap of 3.3 eV and large exciton binding energy of 60 meV at room temperature, ZnO semiconductor has attracted tremendous attention for applications in blue and UV light-emitting diodes, which is expected to be an

alternative to those based on GaN ( $E_g \sim 3.4$  eV at 300 K). In general, II-VI binary semiconductors crystallize in hexagonal wurtzite structure or cubic zinc-blende structure in which four cations surrounded one anion at the corners of tetrahedron. The crystal structures which ZnO shares are cubic, zinc-blende, and wurtzite<sup>1</sup>, as shown in Table 1.1.

Table 1.1 Space group, crystal structure, lattice parameters of ZnO.

Space group	Crystal structure	Lattice parameters	Density ( $\text{g} \cdot \text{cm}^{-3}$ )	Reference
$Fm\bar{3}m$	Cubic	$a = 4.28 \text{ \AA}$	-	PDF#77-0191
$F\bar{4}3m$	Zinc-blende	$a = 4.62 \text{ \AA}$	-	Ref. 2
$P6_3mc$	Hexagonal	$a = 3.25 \text{ \AA}$ $c = 5.21 \text{ \AA}$	5.61	PDF#36-1451

Cubic ZnO belongs to space group  $Fm\bar{3}m$  and this cubic structure is sixfold coordinated. However, the stabilized ZnO with cubic structure can't be obtained by the epitaxial growth. Same with other II-VI oxide semiconductors, hexagonal ZnO can be transformed into the cubic structure at relatively high pressures, because the reduction of the lattice dimensions leads to the interionic Coulomb interaction to favor the ionicity more over the covalent nature. For ZnO, the phase transition from the wurtzite to the cubic induced by high pressure was found at 10 GPa by Bates *et al.*<sup>3</sup>, and a large volume decreased of around 17 %. Decremps *et al.*<sup>4</sup> have investigated the

structure of ZnO transformed from hexagonal to cubic at around 9 GPa by Raman spectroscopy.

In the zinc-blende structure, each Zn atom has four nearest neighbors. The in-plane bonds are stronger than the out-of-plane bonds. The zinc-blende structure ZnO has the highest symmetry compatible with the existence of piezoelectric polarization under the strain in the  $c$ -axis direction.<sup>3</sup> Moreover, it possesses technological advantages such as easier laser cavity growth along the [110] direction, which is evidence for higher optical gain. Ashrafi *et al.*<sup>5</sup> grew the zinc-blend ZnO on GaAs (001) substrates with a ZnS buffer layer by using microwave-plasma-assisted metalorganic molecular-beam epitaxy.

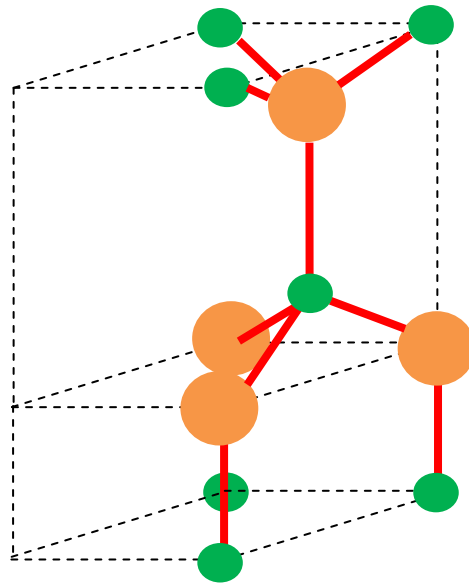


Figure 1.2 Schematic representation of the ZnO with wurtzite structure. The shaded green and orange spheres denote O and Zn atoms respectively.

Among these structures, hexagonal wurtzite structure ZnO has been dominantly observed and is thought to be the most stable structure. ZnO with wurtzite structure

has a hexagonal unit cell with lattice parameters  $a$  and  $c$  ( $c/a=1.633$ ). As shown in Table 1.1, it belongs to space group of  $C_{6v}^4$  ( $P6_3mc$ ). Figure 1.2 shows the schematic representation of the ZnO with wurtzite structure. In an ideal wurtzite structure, the structure includes two interpenetrating hexagonal close packed sub-lattice which consists of one type of atom displaced with respect to each other along the threefold  $c$ -axis by the value of  $u = 3/8 = 0.375$  ( $u$  is defined as the length of the bond parallel to the axis, in units of  $c$ ).<sup>6</sup> One sub-lattice includes four atoms per unit cell and each group-II atom is surrounded by four group-VI atoms. In a real ZnO crystal, the structure deviates from the ideal one by changing the value of  $c/a$  or  $u$ . It is worth noting that a correlation is between the  $c/a$  ration and the parameter  $u$  value. The value of parameter  $u$  increases with the decrease of  $c/a$  ration in such the way that four tetrahedral distances remain nearly constant through a distortion of tetrahedral angles because of long range polar interactions.

## (2) MgO

MgO is used as a catalyst for isotope exchange reactions, dehydrogenation reactions and the oxidative coupling of methane. It can also serve as a substrate or buffer layer for growth of epitaxial ferroelectric films. MgO buffer layers were deposited on GaAs substrates by PLD for epitaxial growth of BaTiO<sub>3</sub> for the first time. The best crystallographic quality was obtained at 350 °C in  $5 \times 10^{-6}$  Torr. In the report of Hsu *et al.*<sup>7</sup>, MgO epitaxial thin films were grown on (100) GaAs by magnetron sputtering as a substrate for the growth of oriented PbTiO<sub>3</sub> and highly

oriented crystalline MgO films were obtained when the substrate temperature range from 500 to 530 °C.

MgO has a wide bandgap of 7.8 eV and cubic unit cell with lattice parameters of 4.21 Å.<sup>8</sup> Cubic MgO belongs to space group of  $Fm\bar{3}m$ . Figure 1.3 shows schematic representation of the MgO with cubic structure. The shaded green and blue spheres denote O and Mg atoms, respectively.

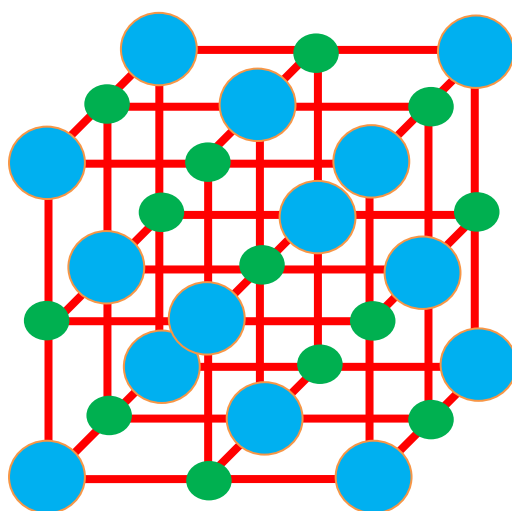


Figure 1.3 Schematic representation of the MgO with cubic structure. The shaded green and blue spheres denote O and Mg atoms, respectively.

MgO films were usually grown by evaporating the metallic component in a moderate oxygen atmosphere on an adequate metallic substrate. The lattice match plays an important role in epitaxial growth, in which the planarity of the overlayer and the detailed nature of the oxide-metal bonding depend on the extent of interface strain. According to previous report, due to the reduction of lattice mismatch, Ag and Mo substrates were regarded as good candidates for the growth of MgO epitaxial layers.

The lattice structure and optical property of epitaxial MgO layers grown on Ag and Mo substrates have been studied.<sup>9</sup> Wollshlager *et al.*<sup>10</sup> studied the stoichiometry and the morphology of MgO layers epitaxially grown on Ag (100) by means of X-ray photoelectron and high-resolution spot profile analysis low-energy electron diffraction. Strong differences have been found for epitaxy of MgO films, depending on the preparation condition. Ultra-thin MgO films have been synthesized under UHV conditions by evaporating Mg onto Mo (100) various background pressures of oxygen. Low-energy electron diffraction studies indicated that MgO films grow epitaxially in the 200-600 K substrate temperature range with the (100) face of MgO oriented parallel to Mo (100).<sup>11</sup> In recent years, MgO films were also grown by other methods such as PLD, MBE, magnetron sputtering, and sol-gel method on various substrates. Susaki *et al.*<sup>12</sup> have found that epitaxial MgO (111) films grow under a wide range of deposition conditions (substrate temperature of 400 -800 °C, oxygen partial pressures of 10<sup>-4</sup>-100 Pa) on Al<sub>2</sub>O<sub>3</sub> substrates by PLD. Chen *et al.*<sup>13</sup> reported about selective growth of singly oriented (110)-, (100)-, and (111)-MgO films on Si (100) substrates by PLD and the mechanism of the orientation selection is attributed to the energy balance between the surface and interface energies.

### (3) MgZnO

Group-II elements such as Mg and Cd are extensively used in adjusting the bandgap of ZnO. Since radii of Zn<sup>2+</sup> is 0.60 Å and Radii of Mg<sup>2+</sup> is 0.57 Å,<sup>14</sup> therefore, Mg can be easily incorporated in to the ZnO lattice with smaller structural

deformations.<sup>15</sup> MgZnO alloy material is considered to be one the best candidate to increase the bandgap energy of ZnO from 3.3 to 7.8 eV by alloying it with different content of MgO.<sup>16</sup> MgZnO is a promising material for optoelectronic applications in the UV and deep UV region. MgZnO alloy has two different crystal structures, hexagonal wurzite ( $a = 3.24 \text{ \AA}$  and  $b = 5.20 \text{ \AA}$ ) and rock-salt cubic ( $a = 4.24 \text{ \AA}$ ) structure. According to the phase diagram of the ZnO-MgO solid solution, the thermodynamic solubility limit of ZnO in MgO is ~40 %, while that of MgO in ZnO is very small ~ 4 %.<sup>16</sup> MgZnO films grown via the PLD growth technique were found to exceed the low solubility limit of MgO in ZnO, and single phase films with the hexagonal wurzite structure if up to ~35 % Mg were achieved.<sup>17</sup> On the other hand, the thermal stability of the cubic-phase MgZnO films was studied by annealing the films at high temperatures. In the report of Chen *et al.*<sup>18</sup>, for the MgZnO films with the Mg content exceeding 0.55, the films had stable cubic phase after annealing at high temperature of 1000 °C.

It requires accurate information of fundamental properties, in particular, the emission property, bandgap energy, and the index of transmission for designing MgZnO-based UV optoelectronic devices. Optical research about MgZnO, including the photoluminescence measurements for emission behaviour and transmission spectra for bandgap energy, indicated that the bandgap energy of MgZnO has a blueshift with the increase of the Mg content. Ohtomo *et al.*<sup>19</sup> found the bandgap energy increased from 3.30 to 3.99 eV with Mg content up to 33% in hexagonal MgZnO films. Similar results were also reported by Narayan *et al.*<sup>20</sup> The

investigation reported by Choopun *et al.* indicated that MgZnO films with Mg content exceeding 50 % showed a wide bandgap larger than 5.0 eV.<sup>21</sup> In the work of Thapa *et al.*<sup>22</sup> MgZnO films with bandgaps that span the UV range of 3.2-5.7 eV were realized.

For fabrication of MgZnO films, growth conditions such as substrate temperature and oxygen pressure have a great influence on crystal structure, optical properties, and electrical properties. Liu *et al.*<sup>23</sup> have found that as the substrate temperature increases from 300 to 900 °C, Mg content in single-phase wurtzite MgZnO films increased significantly from 27 close to 46 %, and the bandgap is shifted from 3.49 to 3.88 eV. Han *et al.*<sup>24</sup> investigated the effect of oxygen pressure on preferred deposition orientations and optical properties of cubic MgZnO thin films. It indicated that the preferred orientation of cubic MgZnO changed from (200) to (111) when deposition pressure increased and the absorption edges of which shift to longer wavelength direction due to the decrease of Mg content in the MgZnO film. Moreover, in spite of the lattice mismatch between epitaxial films and substrate, MgZnO can be grown on many substrates, such as sapphire, Si, GaN, GaAs, ScAlMgO<sub>4</sub>, and ITO as well as ZnO or MgO layers.

Up to now, a lot of common deposition methods succeeded in preparing the high-quality MgZnO alloy films, such as MBE,<sup>25</sup> MOCVD,<sup>26</sup> electrophoretic deposition (EPD),<sup>27</sup> reactive electron beam evaporation deposition (REBED),<sup>28</sup> RF magnetron sputtering,<sup>22</sup> and PLD.<sup>29,30</sup>

Ohtomo *et al.*<sup>19</sup> reported the *c*-axis MgZnO films were epitaxially grown by PLD on ZnO epitaxial films and sapphire (0001) substrates using ceramic tagerts. The

MgZnO film with the Mg content of 0.33 had a bandgap energy of 3.99 eV at room temperature. When the Mg content was above 0.36, MgO impurity phase separation can be observed. Sharma *et al.*<sup>31</sup> investigated the optical and structural properties of high-quality single-crystal epitaxial MgZnO films grown by PLD method. The intense UV band edge was observed at room temperature and 77 K with the Mg content up to 36% in the films. Moreover, post-deposition annealing in oxygen was found to reduce the number of defects and to improve the optical properties of the films. In the work of Teng *et al.*,<sup>32</sup> indices of refraction for MgZnO epitaxial films grown by PLD on sapphire substrates with Mg content up to 36 % were determined in the range of wavelength 457-968 nm by analysis of optical transmission spectra and prism-coupled waveguide measurement. Choopun *et al.*<sup>21</sup> reported on the realization of wide bandgap (5-6 eV), single-phase, metastable, and epitaxial MgZnO thin film alloys grown on sapphire by PLD. It was found that the Mg content, structure, and bandgap of MgZnO film alloys depended critically on the growth temperature. A wurtzite N-doped MgZnO film with the Mg content of 20 % was grown by plasma-assisted MBE on *c*-plane sapphire using radical NO as oxygen source and nitrogen dopant. A hole concentration of  $6.1 \times 10^{17} \text{ cm}^{-3}$  and a mobility of  $6.42 \text{ cm}^2/\text{V}\cdot\text{s}$  were observed in *p*-type MgZnO:N by Wei *et al.*<sup>33</sup> Ju *et al.*<sup>34</sup> grew the phase stability of cubic  $\text{Mg}_{0.55}\text{Zn}_{0.45}\text{O}$  thin film by MOCVD and studied this film by continuous thermal annealing. A continuous thermal annealing at 750 °C can improved the crystal quality and surface smoothness greatly. However, the phase separation occurred when the sample was annealed at a higher temperature. A lower pumping threshold was

expected, if an exciton-related recombination rather than an electron-hole plasma recombination is employed. The quantum well structure is effective toward this goal. Ohtomo *et al.*<sup>35</sup> succeeded in growing ZnO/Mg<sub>0.2</sub>Zn<sub>0.8</sub>O quantum well structure with a bandgap offset of about 0.5 eV by using MBE on sapphire substrate. The thickness of well layer was in the range of 1.7-12 nm and the thickness of barrier layer is 6.2 nm. As the well layer thickness decreased below 5 nm, the emission peak and absorption edge show a blueshift due to the quantum-size effect. MgZnO-based solar-blind UV detectors have attracted increasing attention. In the report of Han *et al.*<sup>36</sup>, an UV photodetector was fabricated on MgZnO thin film grown by MOCVD. The peak response of the device centers at 238 nm and the cutoff wavelength is 253 nm. The peak responsivity is 129 mA/W at 15 V bias and the UV/visible reject ratio is 4 orders of magnitude. High mobility in two-dimensional electron systems were observed in high quality MgZnO/ZnO heterojunctions. Solovyev *et al.*<sup>37</sup> studied the optical transitions present in two-dimensional electron systems confined at MgZnO/ZnO heterojunctions by using low temperature PL and reflectance measurement. The first excited electron subband is shown to be empty of electrons. Falson *et al.*<sup>38</sup> found the carrier mobility exceeded  $1 \times 10^6$  cm<sup>2</sup>/Vs in MgZnO/ZnO heterostructures grown at 730 °C by using MBE method.

## 1.2.2 Group III oxides

### (1) Ga<sub>2</sub>O<sub>3</sub>

Owing to its large bandgap energy (~ 4.9 eV),<sup>39</sup> Ga<sub>2</sub>O<sub>3</sub> has recently attracted

focused interest as a promising material for UV optical and power-electronic devices.  $\text{Ga}_2\text{O}_3$  has five phases classified as  $\alpha$ ,  $\beta$ ,  $\gamma$ ,  $\delta$ , and  $\epsilon$ . Among these five phases,  $\beta$ - $\text{Ga}_2\text{O}_3$  is the thermally most stable. Heat treatment of the other metastable transition phases can convert to  $\beta$ - $\text{Ga}_2\text{O}_3$ . Figure 1.4 shows the conversion relationships among these five phases.

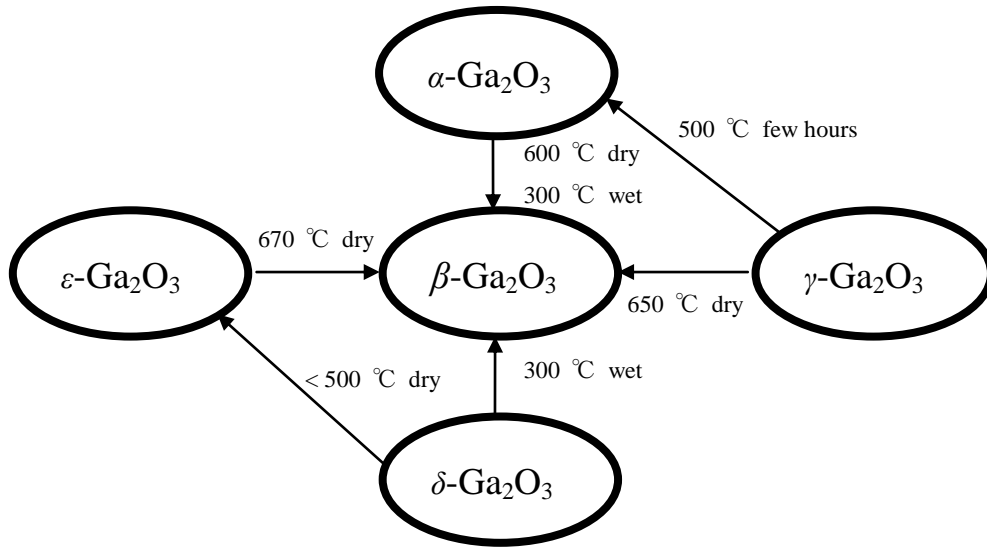


Figure 1.4 Conversion relationships among the five phases of  $\text{Ga}_2\text{O}_3$ .

Monoclinic  $\beta$ - $\text{Ga}_2\text{O}_3$  has a melting point of 1740 °C. It belongs to the monoclinic system and lattice parameters are  $a = 1.22$  nm,  $b = 0.30$  nm,  $c = 0.58$  nm,  $\alpha = \gamma = 90^\circ$ , and  $\beta = 103.83^\circ$ .<sup>10</sup> The Ga ions are in distorted octahedral and tetrahedral sites with Ga-O bond distances of 2.00 and 1.83 Å, respectively, and the O ions are in a distorted cubic closest packing arrangement. Distortions in  $\text{Ga}_2\text{O}_3$  structure are the reasons for the level of stability. Figure 1.5 shows schematic representation of monoclinic  $\beta$ - $\text{Ga}_2\text{O}_3$ . The tetrahedral coordination Ga ions named Ga (IV) and the octahedral

coordinational Ga ions called Ga (VI) are shown in figure 1.5. The chains are connected by GaO<sub>4</sub> tetrahedral chains, and the doubly connected straight chains of GaO<sub>6</sub> edge shared octahedral run along *b*. Moreover, since octahedral Ga (VI) chain which can constitute the paths followed by carrier electrons is present in the lattice along the *b* axis, thus (-201) oriented  $\beta$ -Ga<sub>2</sub>O<sub>3</sub> film in which the *b* axis is parallel to the substrate is considered to enhance the conductivity.<sup>41</sup>

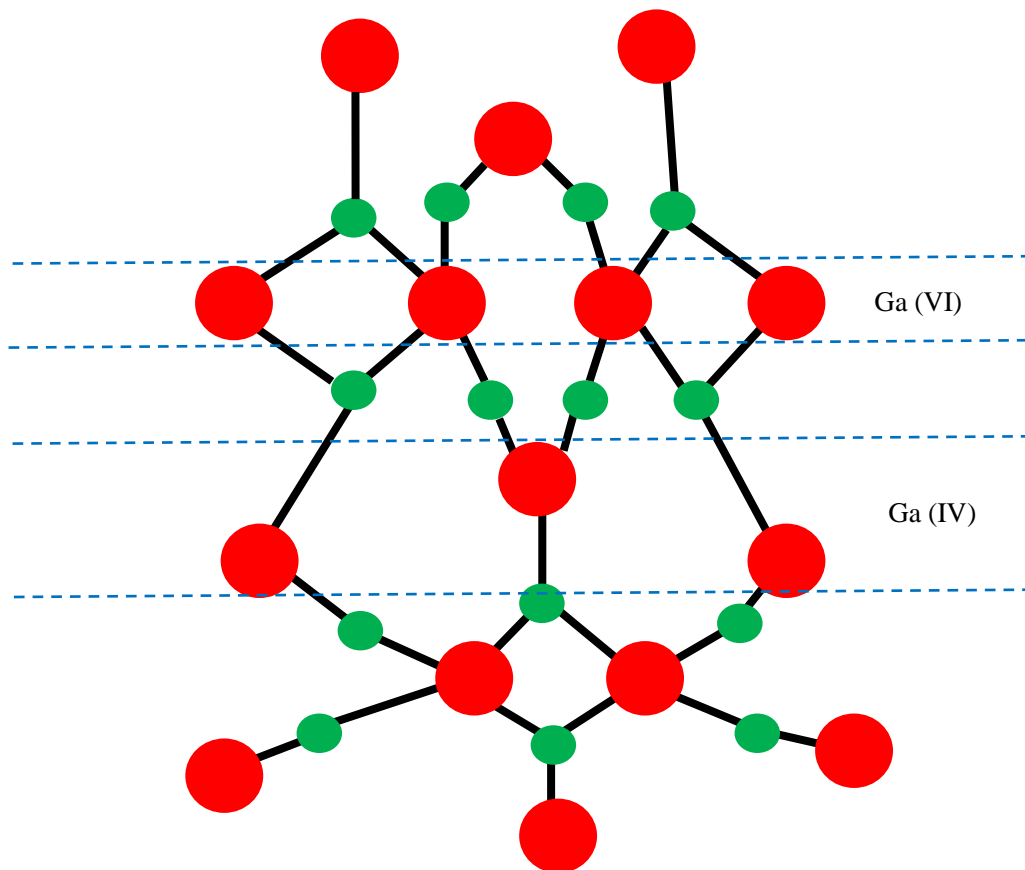


Figure 1.5 Schematic representation of monoclinic  $\beta$ -Ga<sub>2</sub>O<sub>3</sub>. The shaded green and red spheres denote O and Ga atoms, respectively.

Ga<sub>2</sub>O<sub>3</sub> films have been grown by various methods such as sputtering, spray

pyrolysis, sol-gel method, MBE, and PLD.<sup>42-43</sup> In our previous work, Ga<sub>2</sub>O<sub>3</sub> films were grown on (0001) sapphire substrates by PLD method. The effect of substrate temperature on crystal structure, surface morphology, and transmittance has been systematically investigated. The (-201) oriented Ga<sub>2</sub>O<sub>3</sub> films can be obtained at substrate temperature of 500 °C.<sup>39</sup>

## (2) Al<sub>2</sub>O<sub>3</sub>

Al<sub>2</sub>O<sub>3</sub> is a technically important material with chemical and thermal stability, excellent dielectric properties, and the strong adhesion to various materials.<sup>44</sup> It is widely used as buffer layers, gate oxides, and other electronic circuit elements.<sup>45</sup> Moreover, Al<sub>2</sub>O<sub>3</sub> has paid increasing attention to explore its potential applications in high energy storage density capacitors due to its wide bandgap, high dielectric strength and large permittivity.<sup>46</sup>

Table 1.2 Common methods for formation of metastable structure and the stable

### $\alpha$ -Al<sub>2</sub>O<sub>3</sub> phase.

	$\gamma$ -AlOOH (boehmite)	$\xrightarrow{300-500\text{ }^\circ\text{C}}$	$\gamma$	$\xrightarrow{700-800\text{ }^\circ\text{C}}$	$\delta$	$\xrightarrow{900-1000\text{ }^\circ\text{C}}$	$\theta$	$\xrightarrow{1000-1100\text{ }^\circ\text{C}}$	$\alpha$ -Al <sub>2</sub> O <sub>3</sub>
fcc	$\alpha$ -Al(OH) <sub>3</sub> (bayerite)	$\xrightarrow{200-300\text{ }^\circ\text{C}}$	$\eta$	$\xrightarrow{600-800\text{ }^\circ\text{C}}$	$\theta$	$\xrightarrow{1000-1100\text{ }^\circ\text{C}}$			$\alpha$ -Al <sub>2</sub> O <sub>3</sub>
	Melting Al	$\longrightarrow$	$\gamma$	$\longrightarrow$	$\delta$	$\longrightarrow$	$\theta$	$\longrightarrow$	$\alpha$ -Al <sub>2</sub> O <sub>3</sub>
	$\alpha$ -AlOOH (diaspore)	$\xrightarrow{700-800\text{ }^\circ\text{C}}$							$\alpha$ -Al <sub>2</sub> O <sub>3</sub>
hcp	$\gamma$ -Al(OH) <sub>3</sub> (gibbsite)	$\xrightarrow{150-300\text{ }^\circ\text{C}}$	$\chi$	$\xrightarrow{650-750\text{ }^\circ\text{C}}$	$\kappa$	$\xrightarrow{1000\text{ }^\circ\text{C}}$			$\alpha$ -Al <sub>2</sub> O <sub>3</sub>
	5 Al <sub>2</sub> O <sub>3</sub> · H <sub>2</sub> O	$\xrightarrow{700-800\text{ }^\circ\text{C}}$	$\kappa$	$\xrightarrow{1000\text{ }^\circ\text{C}}$					$\alpha$ -Al <sub>2</sub> O <sub>3</sub>

$\text{Al}_2\text{O}_3$  has many metastable polymorphs besides the thermodynamically stable  $\alpha$ - $\text{Al}_2\text{O}_3$ . These metastable structures can be divided into two broad categories a face-centered cubic (fcc) and a hexagonal close-packed (hcp) arrangement of O anion.<sup>47</sup> The different polymorphs are caused by the distribution of cations within each subgroup. The structures based on packing of O anion include  $\gamma$ ,  $\delta$  (orthorhombic or tetragonal),  $\theta$  (monoclinic), and  $\eta$  (cubic), while structures in hcp packing include  $\chi$  (hexagonal),  $\alpha$  (trigonal), and  $\kappa$  (orthorhombic) phases. Heat treatments designed to promote stable scale formation depend on an understanding of the metastable intermediate structures and the transformation mechanisms that lead to the formation of  $\alpha$ - $\text{Al}_2\text{O}_3$ . Table 1.2 shows common methods for formation of metastable structure and the stable  $\alpha$ - $\text{Al}_2\text{O}_3$  phase.  $\alpha$ - $\text{Al}_2\text{O}_3$  possesses 10 unit atoms in the unit cell and has trigonal symmetry with rhombohedral Bravais centering. The crystallography of  $\alpha$ - $\text{Al}_2\text{O}_3$  has been analyzed by Kronberg *et al.*<sup>48</sup> The structure of  $\alpha$ - $\text{Al}_2\text{O}_3$  can be considered as hcp sublattice of O anions, with 2/3 of the octahedral interstices filled with Al cations in an ordered array. The O anions in  $\alpha$ - $\text{Al}_2\text{O}_3$  structure occupy 18c Wyckoff positions with the coordinate of (0.306, 0, 0.25), whereas the Al cations are at the position of 12c with the coordinate of (0, 0, 0.347).

Up to now,  $\text{Al}_2\text{O}_3$  films have been prepared by various methods such as atomic layer deposition (ALD), MOCVD, MBE, and PLD. Groner *et al.*<sup>49</sup> reported detailed leakage current and breakdown electric-field characteristics of ultrathin  $\text{Al}_2\text{O}_3$  dielectrics on GaAs grown by ALD and found the leakage current in ultrathin  $\text{Al}_2\text{O}_3$  dielectrics on GaAs is comparable to or even lower than that of state-of-the-art  $\text{SiO}_2$

on Si. In the works of Balakrishnan *et al.*<sup>50</sup>, highly oriented Al<sub>2</sub>O<sub>3</sub> thin films were grown on SrTiO<sub>3</sub> (100),  $\alpha$ -Al<sub>2</sub>O<sub>3</sub> (1102),  $\alpha$ -Al<sub>2</sub>O<sub>3</sub> (0001) and MgO (100) single crystal substrates at an optimized oxygen partial pressure of  $3.5 \times 10^{-3}$  mbar and 700 °C by PLD. It was found that the phase formation of the Al<sub>2</sub>O<sub>3</sub> thin films depends on the nature of the substrates, deposition method and processing parameters. According to the report of Wu *et al.*<sup>51</sup>, single-phase Al<sub>2</sub>O<sub>3</sub> thin films have been epitaxially grown by MBE on Si (111) substrates despite a lattice mismatch of more than 30%. Dimethyl, diethyl, and di-iso-butyl aluminum acetylacetonate compounds were used to grow Al<sub>2</sub>O<sub>3</sub> thin films by MOCVD. Al<sub>2</sub>O<sub>3</sub> films were grown in the temperature range 400-520 °C under an oxygen or water vapor atmosphere.

### (3) In<sub>2</sub>O<sub>3</sub>

Due to its unique properties of high transparency and simultaneously metallic conductivity, In<sub>2</sub>O<sub>3</sub> is of great interest for various technological applications ranging from chemical sensors to optoelectronics.<sup>52,53</sup> It has been satisfied some important demands for direct photoelectrolysis of water splitting. With excellent conductivity and stability, its position of the conduction and valence band edges right bracket the redox potentials of water. In<sub>2</sub>O<sub>3</sub> has a wide bandgap of 3.5 eV, which makes it inefficient in utilizing visible light, thus not much research focus on the application of In<sub>2</sub>O<sub>3</sub> as a photovoltaic material. Sn-doped In<sub>2</sub>O<sub>3</sub> (In<sub>2</sub>O<sub>3</sub> or ITO) is currently the industry standard *n*-type transparent conducting oxides, having transparency as high as 90%, carrier concentrations exceeding  $10^{21}$  cm<sup>-3</sup>, and resistivity below  $10^{-5}$   $\Omega \cdot \text{cm}$ .

Four In<sub>2</sub>O<sub>3</sub> polymorphs have been synthesized to date, which includes cubic

bixbyite-type  $c\text{-In}_2\text{O}_3$  (C-type structure of rare-earth oxides), rhombohedral corundum-type  $\text{rh-In}_2\text{O}_3$ , orthorhombic  $\text{Rh}_2\text{O}_3$  (II)-type  $o'\text{-In}_2\text{O}_3$ , and orthorhombic  $\text{Gd}_2\text{S}_3$  (II)-type  $o''\text{-In}_2\text{O}_3$ , respectively.<sup>54</sup>  $c\text{-In}_2\text{O}_3$  and  $\text{rh-In}_2\text{O}_3$  can be obtained by solution-based and solvothermal routes. The growth method and stability of  $o'\text{-In}_2\text{O}_3$  face some controversy. According to the report,  $o'\text{-In}_2\text{O}_3$  is stable in the pressure range from 8.1 to 19.9 GPa. Orthorhombic  $\text{Gd}_2\text{S}_3$  (II)-type  $o''\text{-In}_2\text{O}_3$  structure can be observed at the pressure over 19.9 GPa, and it transforms to  $\text{rh-In}_2\text{O}_3$  when decompression.

#### (4) $(\text{AlGa})_2\text{O}_3$ and $(\text{InGa})_2\text{O}_3$

In order to further increasing the bandgap energy of  $\text{Ga}_2\text{O}_3$ , e.g. for designing of heterostructures like quantum wells or light detectors which are sensitive even deeper in the UV spectral range, the  $(\text{AlGa})_2\text{O}_3$  alloy material is a promising candidate due to the tunable bandgap from 4.9 ( $\text{Ga}_2\text{O}_3$ ) to 8.6 eV ( $\text{Al}_2\text{O}_3$ ).<sup>55</sup>

$\alpha\text{-Al}_2\text{O}_3$  has a crystal structure of corundum which is different from that of  $\text{Ga}_2\text{O}_3$ . It suggests that  $(\text{AlGa})_2\text{O}_3$  alloys exhibit phase separation at certain Al content. According to previous works, different upper limits of the incorporation of Al atoms into the  $\text{Ga}_2\text{O}_3$  lattice were reported. For powder materials this limits is around 78 % and for film samples approximately 60 % were found. Several thin-film growth methods have been used to develop for the epitaxial growth of  $(\text{AlGa})_2\text{O}_3$  alloys. Among these growth methods, PLD has many advantages such as relative high kinetic energies that the ablated species have and completely compositional consistency

between a target and a deposited film. Therefore, it is one of the promising growth technologies for obtained  $(\text{AlGa})_2\text{O}_3$  alloy thin film.

In 2009, Oshima *et al.*<sup>56</sup> grew  $\beta$ - $(\text{AlGa})_2\text{O}_3$  alloy thin films on (100)-oriented  $\beta$ - $\text{Ga}_2\text{O}_3$  substrates by plasma-assisted MBE. The  $\beta$  phase structure can be observed in the Al content range from 0 to 0.61. When the Al content is below 0.4, step-flow growth was realized and carrier accumulation can be observed in the heterointerface. In the work of Watanabe *et al.*,<sup>57</sup> the  $\gamma$ - $\text{Ga}_2\text{O}_3$ - $\text{Al}_2\text{O}_3$  solid solutions were grown by spray pyrolysis. For Ga rich composition,  $\gamma$ - $\text{Ga}_2\text{O}_3$ - $\text{Al}_2\text{O}_3$  solid solutions can be directly grown, while for Al rich composition a sufficient thermal energy needed to be supplied during the spray pyrolysis. Moreover, the spray pyrolysis conditions had a great effect on the physical properties of  $\gamma$ - $\text{Ga}_2\text{O}_3$ - $\text{Al}_2\text{O}_3$  solid solutions. Ito *et al.*<sup>58</sup> showed the deposition of the  $(\text{AlGa})_2\text{O}_3$  with corundum structure by the spray-assisted mist CVD method. In their work, the control of the Al content and bandgap energy were also reported. Zhang *et al.*<sup>59</sup> prepared the  $(\text{AlGa})_2\text{O}_3$  films on sapphire substrates by using the PLD method. The bandgap energies of  $(\text{AlGa})_2\text{O}_3$  films increased from 5 to 7 eV with the Al content with the increase of Al content in all Al content range. Kranert *et al.*<sup>60</sup> presented the investigations about XRD and Raman spectroscopy of  $(\text{AlGa})_2\text{O}_3$  films grown with different Al content on MgO (100) substrate and bulk-like ceramics. Grund *et al.*<sup>61</sup> determined the dielectric function of the  $(\text{AlGa})_2\text{O}_3$  alloy material with the Al content from 0.11 to 0.55 by using spectroscopic ellipsometry within a spectral range from 0.5 to 8.5 eV. Wakabayashi *et al.*<sup>62</sup> reported on impacts of oxygen-radical ( $\text{O}^*$ ) atmosphere for PLD of  $(\text{AlGa})_2\text{O}_3$  alloy films on

(010)  $\beta$ -Ga<sub>2</sub>O<sub>3</sub> substrate in comparison with conventional PLD in O<sub>2</sub> atmosphere.

Due to its wide bandgap between 3.6 to 4.9 eV,<sup>11</sup> the (InGa)<sub>2</sub>O<sub>3</sub> alloy material can be promising for use in applications such as transparent electronics, high-power devices, and solar-blind UV detectors. In order to realize a photodetector that exhibits high responsivity in the deep UV region, the bandgap need to be decreased. One way of decreasing the bandgap is by alloying with materials with a smaller bandgap. In<sub>2</sub>O<sub>3</sub> having a bandgap of 3.5 eV with cubic structure can be used to alloy Ga<sub>2</sub>O<sub>3</sub>. The structure of (InGa)<sub>2</sub>O<sub>3</sub> alloys were that of either cubic In<sub>2</sub>O<sub>3</sub> or  $\beta$ -Ga<sub>2</sub>O<sub>3</sub>, which depended on the Ga/In ratio in it.

Recently, (InGa)<sub>2</sub>O<sub>3</sub> alloy films have been grown by various methods, such a sputtering, MOCVD, MBE, sol-gel method, and PLD. In our previous work, (InGa)<sub>2</sub>O<sub>3</sub> films were grown on (0001) sapphire substrates by using PLD method. The bandgap energies of (InGa)<sub>2</sub>O<sub>3</sub> films can be adjusted from 3.8 to 5.1 eV. The thermal annealing effects on the (InGa)<sub>2</sub>O<sub>3</sub> films with In content of 0.3. Moreover, in order to understand the annealing effect, the further research on the (InGa)<sub>2</sub>O<sub>3</sub> films with same nominal indium content of 0.3 was carried out by studying the annealing gas ambient and temperature influences.

### **1.3 Purpose and Outline**

As has discussed above, MgZnO with a tunable bandgap in the range from 3.3-7.8 eV is a promising candidate for UV and deep UV optoelectronic devices which have attracted much attention for their potential application in convert communications,

missile plume sensing, chemical/biological agents detection, flame sensing, and water purification. In order to realize MgZnO optoelectronic devices, great efforts have made remarkable progress for growing this alloy material. However, the structural difference between hexagonal ZnO and cubic MgO leads to phase separation, which greatly degraded the crystalline quality of MgZnO films. It limited the application of MgZnO alloy in deep UV region. Therefore, it is very necessary to grow single phase MgZnO alloy thin films in all Mg content range. Moreover, in order to calculate the band alignment for designing and engineering a device, it is important to investigate the fundamental bandgap of single phase MgZnO epitaxial films grown in all Mg content range. The determination of bandgap bowing parameter which characterizes the nonlinear dependence of the fundamental bandgap on the alloy composition is also needed for the design of optoelectronic devices.

Due to the phase separation and poor crystalline quality, the application of MgZnO alloy was limited in deep UV region. In comparison with ZnO, Ga<sub>2</sub>O<sub>3</sub> has a wider bandgap (4.9 eV) at room temperature. Therefore, it has attracted much attention as the most promising materials for fabricating deep UV optoelectronic devices such as light detectors and emitters. A crucial step for designing optoelectronic devices is to develop quantum well structures according to bandgap engineering. The doping into wide bandgap binary semiconductors like Ga<sub>2</sub>O<sub>3</sub> with selective elements provides an effective method to engineer the bandgap of alloys. Group III indium and aluminum are extensively used to tailor the bandgap of Ga<sub>2</sub>O<sub>3</sub>. Indium doping was studied by some researchers for narrowing the bandgap of Ga<sub>2</sub>O<sub>3</sub> and aluminum doping in Ga<sub>2</sub>O<sub>3</sub>

was explored for enlarging the bandgap. In our previous work, bandgap engineering in  $(\text{AlGa})_2\text{O}_3$  and  $(\text{InGa})_2\text{O}_3$  alloys has been realized. For further developing the  $(\text{AlGa})_2\text{O}_3$  and  $(\text{InGa})_2\text{O}_3$ -based optoelectronic devices, detailed and reliable experimental data on the optical properties of  $(\text{AlGa})_2\text{O}_3$  and  $(\text{InGa})_2\text{O}_3$  thin films must be clearly investigated. Raman spectroscopy, as a convenient, effective, and nondestructive method for studying the lattice vibration characteristics, has been widely employed for semiconductors. It is well known that temperature-dependent Raman scattering can be used to obtain the information of phonon decay which is an essential aspect to understand the phonon behaviors. Moreover, the particular temperature coefficients for different Raman active modes can also be estimated by temperature-dependent Raman scattering, which can be used to obtain structural information. Therefore, the temperature-dependent Raman scattering of  $(\text{AlGa})_2\text{O}_3$  and  $(\text{InGa})_2\text{O}_3$  thin films were studied.

The purpose of this dissertation mainly includes:

- (1) Growth of single phase MgZnO thin films.
- (2) Bandgap engineering of MgZnO thin films grown in all Mg content.
- (3) Temperature dependence of Raman scattering in  $(\text{AlGa})_2\text{O}_3$  thin films.
- (4) Temperature dependence of Raman scattering in  $(\text{InGa})_2\text{O}_3$  thin films.

My dissertation is divided into seven chapters, and the outline is as follows,

In Chapter 1, the background of MgZnO,  $(\text{AlGa})_2\text{O}_3$  and  $(\text{InGa})_2\text{O}_3$  alloys is presented, and the purpose of this research is also presented.

In Chapter 2, the PLD system and characterization methods are introduced.

In Chapter 3, the effects of Mg content, oxygen pressure, and substrate temperature on structure and optical properties of single MgZnO films grown in all Mg content by PLD are described. The influence of different substrate is also been discussed.

In Chapter 4, bandgap tunable MgZnO films are grown on sapphire substrates by using PLD. Bandgap energies of MgZnO films are determined by examining the onset of inelastic energy loss in core-level atomic spectra. Fitting of the bandgap energies resulted in two bowing parameters of wurtzite and cubic MgZnO films.

In Chapter 5, the effects of the substrate temperature on surface morphology, optical properties, and crystal quality were studied. Temperature dependence of Raman scattering in  $(\text{AlGa})_2\text{O}_3$  thin films has been measured. The decay process of phonon is discussed in detail.

In Chapter 6, temperature dependence of Raman scattering in  $(\text{InGa})_2\text{O}_3$  thin films has been measured. The decay process of phonon is discussed in detail.

In Chapter 7, the summary of my work is described.

## References

- [1] A. Segura, J. A. Sans, F. J. Manjon, A. Munoz, and M. J. Herrera-Gabrera, *Appl. Phys. Lett.*, 83, 278 (2003).
- [2] F. J. Manjon, K. Syassen, and R. Lauck, *High Press. Res.*, 22, 299 (2002).
- [3] C. H. Bates, W. B. White, and R. Roy, *Science*, 137, 993 (1962).
- [4] F. Decremps, J. Pellicer-Porres, F. Datchi, J.P. Itie, A. Polian, F. Baudelet, and J. Z. Jiang, *Appl. Phys. Lett.*, 81, 4820 (2002).
- [5] A. B. M. A. Ashrafi, A. Ueta, A. Avramescu, H. Kumano, and I. Suemune, *Appl. Phys. Lett.*, 76, 550 (2000).
- [6] U. Ozgur, Y. I. Alivov, C. Liu, A. Teke, M. A. Reshchikov, S. Dogan, V. Avrutin, S. J. Cho, and H. Morkoc, *J. Appl. Phys.*, 98, 041301 (2005).
- [7] W. Y. Hsu, and R. Raj, *Appl. Phys. Lett.*, 60, 3105 (1992).
- [8] K. J. Chang and M. L. Cohen, *Phys. Rev. B*, 15, 4774 (1984).
- [9] T. Kado, *J. Cryst. Growth*, 144, 329 (1994).
- [10] J. Wollschlager, J. Viernow, C. Tegenkamp, D. Erdos, K. M. Schroder, and H. Pfnur, *Appl. Surf. Sci.*, 142, 129 (1999).
- [11] M. C. Wu, J. S. Corneille, C. A. Estrada, J. W. He, and D. W. Goodman, *Chem. Phys. Lett.*, 182, 472 (1991).
- [12] T. Susaki, S. Kumada, T. Katase, K. Matsuzaki, M. Miyakawa, and H. Hosono, *Appl. Phys. Express*, 2, 1403 (2009).
- [13] X. Y. Chen, K. H. Wong, C. L. Mak, X. B. Yin, M. Wang, J. M. Liu, and Z. G. Liu, *J. Appl. Phys.*, 91, 5728 (2002).

- [14] H. Zhang, T. Zhao, G. Hu, L. Miao, and Y. Yang, *J. Mater. Sci: Mater. Electron*, 23, 1933 (2012).
- [15] W. L. Bond, *J. Appl. Phys.*, 36, 1674 (1965).
- [16] X. Gu, M. A. Reshchikov, A. Teke, D. Johnstone, H. Morkoc, B. Nemeth, and J. Nause, *Appl. Phys. Lett.*, 84, 2268 (2004).
- [17] E. Ohshima, H. Ogino, I. Niikura, K. Maeda, M. Sato, M. Ito, and T. Fukuda, *J. Cryst. Growth*, 260, 166 (2004).
- [18] J. Chen, W. Z. Chen, N. B. Chen, D. J. Qiu, and H. Z. Wu, *J. Phys.: Condens. Matter*, 15, L475 (2003).
- [19] A. Ohtomo, M. Kawasaki, T. Koida, K. Masubuchi, H. koinuma, Y. Sakurai, Y. Yoshida, T. Yasuda, and Y. Segawa, *Appl. Phys. Lett.*, 72, 2466 (1998).
- [20] J. Narayan, A. K. Sharama, A. Kvit, C. Jin, J. F. Muth, O. W. Holland, *Solid state Commun.*, 121, 9 (2002).
- [21] S. Choopun, R. D. Vispute, W. Yang, R. P. Sharma, T. Venkatesan, and H. Shen, *Appl. Phys. Lett.*, 80, 1529 (2002).
- [22] D. Thapa, J. Huso, H. Che, M. Huso, J.L. Morrison, D. Gutierrez, M.G. Norton, and L. Bergman, *Appl. Phys. Lett.*, 102, 191902 (2013).
- [23] C. Y. Liu, H. Y. Xu, L. Wang, X. H. Li, and Y. C. Liu, *J. Appl. Phys.*, 106, 073518 (2009).
- [24] S. Han, Y. K. Shao, Y. M. Lu, P. J. Cao, W. J. Liu, Y. X. Zeng, F. Jia, and D. L. Zhu, *Mater. Res. Bull.*, 64, 76 (2015).
- [25] H. D. Sun, T. Makino, Y. Segawa, M. Kawasaki, A. Ohtomo, K. Tamura, H.

- Koinuma, J. Appl. Phys., 91, 1993 (2002).
- [26] W. I. Park, G. C. Yi, H. M. Jang, Appl. Phys. Lett., 79, 2002 (2001).
- [27] Y. B. Jin, B. Zhang, S. M. Yang, Y. Z. Wang, J. Chen, H. Z. Zhang, C. H. Huang, C. Q. Cao, H. Cao, R. P. H. Chang, Solid state Commun., 119, 409 (2001).
- [28] N. B. Chen, H. Z. Wu, T. N. Xu, J. Appl. Phys., 97, 023515 (2005).
- [29] X. Wang, K. Saito, T. Tanaka, M. Nishio, Q. Guo, J. Alloy. Compd., 627, 383 (2015).
- [30] X. Wang, K. Saito, T. Tanaka, M. Nishio, T. Nagaoka, M. Arita, and Q. Guo, Appl. Phys. Lett., 107, 022111 (2015).
- [31] A. K. Sharma, J. Narayan, J. F. Muth, C. W. Teng, C. Jin, A. Kvit, R. M. Kolbas, and, O. W. Holland, Appl. Phys. Lett., 75, 21 (1999).
- [32] C. W. Teng, J. F. Muth, U. Ozgur, M. J. Bergmann, H. O. Everitt, A. K. Sharma, C. Jin, and J. Narayan, Appl. Phys. Lett., 76, 979 (2000).
- [33] Z. P. Wei, B. Yao, Z. Z. Zhang, Y. M. Lu, D. Z. Shen, B. H. Li, X. H. Wang, J. Y. Zhang, D. X. Zhao, and X. W. Fan, Appl. Phys. Lett., 89, 102104 (2006).
- [34] Z. G. Ju, C. X. Shan, C. L. Yang, J. Y. Zhang, B. Yao, D. X. Shen, and X. W. Fan, Appl. Phys. Lett., 94, 10192 (2009).
- [35] A. Ohtomo, M. Kawasaki, I. Ohkubo, H. Koinuma, T. Yasuda, and Y. Segawa, Appl. Phys. Lett., 75, 980 (1999).
- [36] S. Han, Z. Zhang, J. Zhang, L. Wang, J. Zheng, H. Zhao, Y. Zhang, M. Jiang, S. Wang, D. Zhao, C. Shan, B. Li, and D. Shen, Appl. Phys. Lett., 99, 242105 (2011).
- [37] V. V. Solovyev, A. B. Vankov, I. V. Kukushkin, J. Falson, D. Zhang, D. Maryenko,

- Y. Kozuka, A. Tsukazaki, J. H. Smet, and M. Kawasaki, *Appl. Phys. Lett.*, 106, 082102 (2015).
- [38] J. Falson, Y. Kozuka, M. Uchida, J. H. Smet, T. Arima, A. Tsukazaki, and M. Kawasaki, *Sci. Rep.*, 6, 26598 (2016).
- [39] F. Zhang, K. Saito, T. Tanaka, M. Nishio, and Q. Guo, *J. Cryst. Growth*, 387, 96 (2014).
- [40] V. G. H. Roy, E. F. Osborn, *J. Am. Chem. Soc.*, 74, 719 (1952).
- [41] N. Ueda, H. Hosono, R. Waseda and H. Kawazoe, *Appl. Phys. Lett.*, 71, 933 (1997).
- [42] D. Shinohara, S. Fujita, *Jpn. J. Appl. Phys.*, 47, 7311 (2008).
- [43] A. Ortiz, J. C. Alonso, E. Andrade, C. Urbiola, *Jpn. J. Appl. Phys.*, 148, F26 (2008).
- [44] Y. Peng, M. Yao, R. Xiao, X. Yao, *J. Mater. Sci: Mater. Electron.*, 27, 11495 (2016).
- [45] H. Fujikawa, Y. Taga, *J. Appl. Phys.*, 75, 2538 (1994).
- [46] R. B. V. Dover, *Appl. Phys. Lett.*, 74, 3041 (1999).
- [47] I. Levin, and D. Brandon, *J. Am. Ceram. Soc.*, 81, 1995 (1998).
- [48] M. L. Kronberg, *Acta Metall.*, 5, 507 (1957).
- [49] M. D. Groner, F. H. Fabreguette, J. W. Elam, and S. M George, *Chem. Mater.*, 16 639 (2003).
- [50] G. Balakrishnan, R. Venkatesh Babu, K.S. Shin, J. I. Song, *Opt. Laser Technol.*, 56, 317 (2014).

- [51] S. Y. Wu, M. Hong, A. R. Kortan, J. Kwo, J. P. Mannaerts, W. C. Lee, and Y. L. Huang, *Appl. Phys. Lett.*, 87, 091908 (2005).
- [52] J. Gan, X. Lu, J. Wu, S. Xie, T. Zhai, M. Yu, Z. Zhang, Y. Mao, S. C. Wang, Y. Shen, and T. Tong, *Sci. Rep.*, 3, 1021 (2013).
- [53] D. Scanlon, A. Regoutz, R. Egdell, D. Morgan, and G. Watson, *Appl. Phys. Lett.*, 103, 262108 (2013).
- [54] M. F. Bekheet, M. R. Schwarz, S. Lauterbach, H. Kleebe, P. Kroll, R. Riedel, and A. Gurlo, *Angew. Chem. Int. Ed.*, 52, 6531(2013).
- [55] F. Zhang, K. Saito, T. Tanaka, M. Nishio, M. Arita, and Q. Guo, *Appl. Phys. Lett.*, 105, 162107 (2014).
- [56] T. Oshima, T. Okuno, N. Arai, Y. Kobayashi, and S. Fujita, *J. Appl. Phys.*, 48, 070202 (2009).
- [57] T. Wantanabe, Y. Miki, T. Masuda, H. Deguch, H. Kanai, S. Hosokawa, K. Wada, M. Inoue, *Ceramics International*, 37, 3183 (2011).
- [58] H. Ito, K. Kaneko, and S. Fujita, *Jpn. J. Appl. Phys.*, 51, 1002047 (2012).
- [59] F. Zhang, K. Saito, T. Tanaka, M. Nishio, M. Arita, and Q. Guo, *Appl. Phys. Lett.*, 105, 162107 (2014).
- [60] C. Kranert, M. Jenderka, J. Lenzner, M. Lorenz, H. Wenckstern, R. S. Grund, and M. Grundmann, *J. Appl. Phys.*, 117, 1257031 (2015).
- [61] R. Grund, C. Kranert , H. Wenckstern, V. Zviagin, M. Lorenz, and M. Grundmann, *J. Appl. Phys.*, 117, 165371 (2015).
- [62] R. Wakabayashi, T. Oshima, M. Hattori, K. Sasaki, T. Masui, A. Kuramata, S.

Yamakoshi, K. Yoshimatsu, A. Ohtomo, *J. Cryst. Growth*, 387, 77 (2015).

## **Chapter 2**

### **Growth and characterization methods**

#### **2.1 PLD**

##### 2.1.1 Introduction

The method of PLD has been used to obtain high quality films of materials for more than a decade. The PLD system melts, evaporates and ionizes material from the surface of a target by using high power laser pulses (typically  $\sim 10^8 \text{ Wcm}^{-2}$ ). The "ablation" event leads to a transient, highly luminous plasma plume which expands rapidly away from the target surface. The ablated material is deposited on an appropriately placed substrate upon which it condenses and the thin film grows. The PLD method can be used in the production of superconducting and insulating circuit components to improved wear and biocompatibility for medical applications. It can also be used to grow semiconductor thin film for scientific research. Figure 2.1 shows the schematic diagram of the main chamber.

Several features make PLD particularly attractive for growing complex material films, such as generation of energetic species, stoichiometric transfer of material from the target, compatibility with background pressures ranging from ultrahigh vacuum (UHV) to 1 Torr, and hyperthermal reaction between the ablated cations and the background gas in the ablation plasma. Films can be deposited with PLD using single, stoichiometric targets of the material of interest, or with multiple targets for different elements.

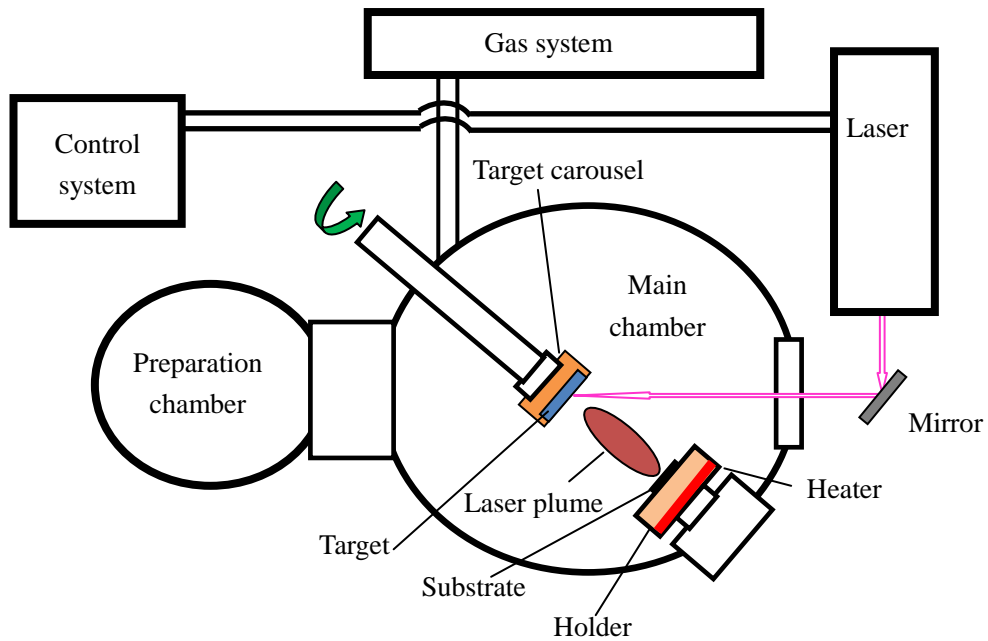


Figure 2.1 Schematic diagram of the Main chamber.

The most important and enabling characteristic in PLD is the ability for realizing stoichiometric transfer of ablated material from multication targets for many materials. It causes by the nonequilibrium nature of the ablation process itself because of absorption of high laser energy density by a small volume of material. For low laser fluence or low absorption at the laser wavelength, the laser pulse can easily heat the targets, with ejected flux because of thermal evaporation of target species. The evaporative flux from a multicomponent target can be determined by the vapor pressure. With the laser fluence increasing, an ablation threshold is reached where laser energy absorption is higher than that for evaporation. The ablation threshold is dependent on the absorption coefficient of the material and is thus wavelength dependent. At higher laser fluence, absorption by the ablated species occurs, leading

to the formation of the plasma at the surface of target. With appropriate choice of ablation wavelength and absorbing target material, high-energy densities are absorbed by a small volume of material, leading to vaporization that is not dependent on the vapor pressures of the constituent cations.

In growth process of PLD, a background gas is often introduced which has two purposes. First, the formation of thin film materials often needs a reactive species as a component of the flux. The amount of reactant gas required for phase formation will depend on the thermodynamic stability of the desired phase. Interaction of ablated species with the background gas often produces molecular species in the ablation plume. These species facilitate multication phase formation. In addition to actively participating in the chemistry of film growth, the background gas can also be used to reduce the kinetic energies of the ablated species. Time-resolved spectroscopy studies of ablation plume expansion have shown that kinetic energies on the order of several hundred electron volts can be observed. A background gas can moderate the plume energies to much less than 1 eV. The vapor formed by laser ablation compresses the surrounding background gas resulting in the formation of a shock wave. Interaction with the ambient gas slows the ablation plume expansion.

### 2.1.2 PLD equipment in our laboratory

Figure 2.2 shows the appearance of the PLD equipment in our laboratory. This PLD system is composed of control system, laser, main chamber, preparation chamber, and gases.

(1) The control system

The control system of PLD possesses many functions, as shown in figure 2.3. It can be used to adjust the substrate temperature, to adjust the pressure of main chamber and preparation chamber. The control system can also be used to control pumps in the main chamber and preparation chamber. The target carousel is controlled by control system. Moreover, the substrate temperature is programmable by employing this system.

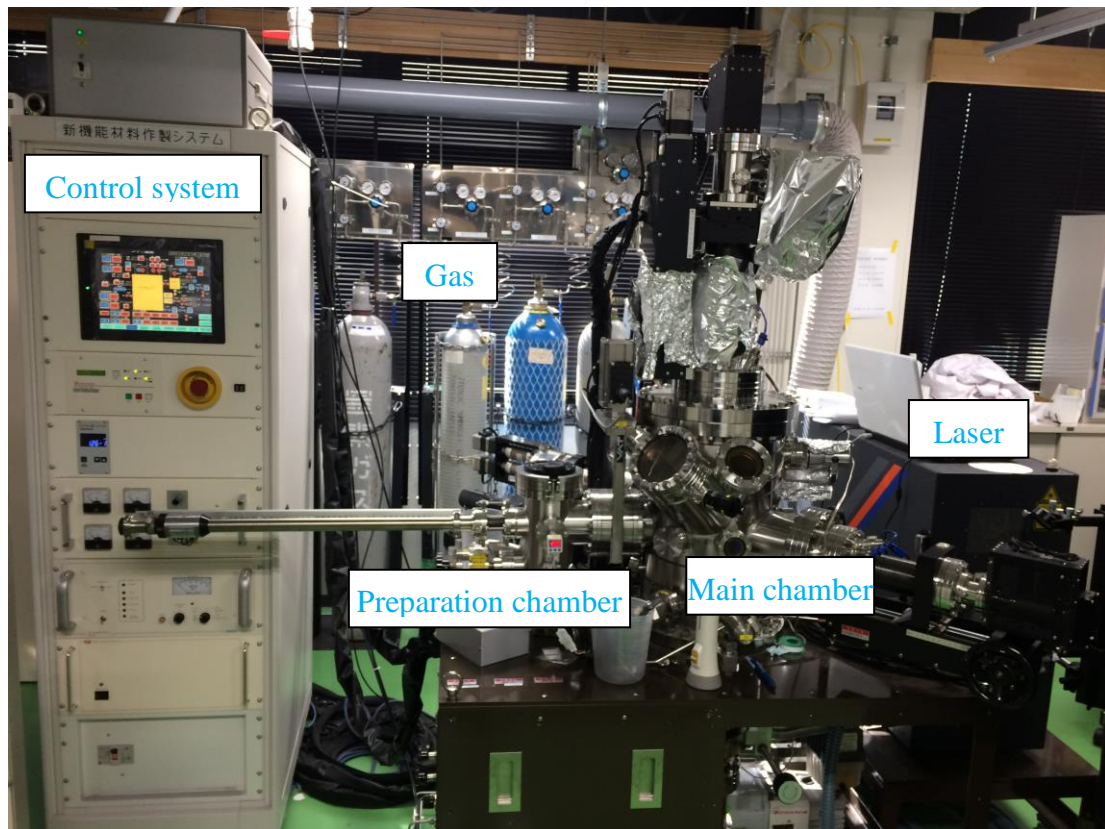


Figure 2.2 The appearance of the PLD equipment.

(2) Laser

The KrF laser (248 nm) uses combination of a noble krypton and a reactive fluorine gas. In an excited state (high energy electron beams or induced by an electrical, with

can make high energy pulses), noble gas krypton can form temporarily bound molecules with themselves or fluorine. The excited gas can lose energy by the way of emission or spontaneous, inducing a strongly repulsive ground state molecule that very quickly dissociates back into two unbound atoms. It causes a population inversion. The reflection mirrors can adjust the direction of the laser towards the growth chamber. The laser is focused by using a lens before it enters the chamber.

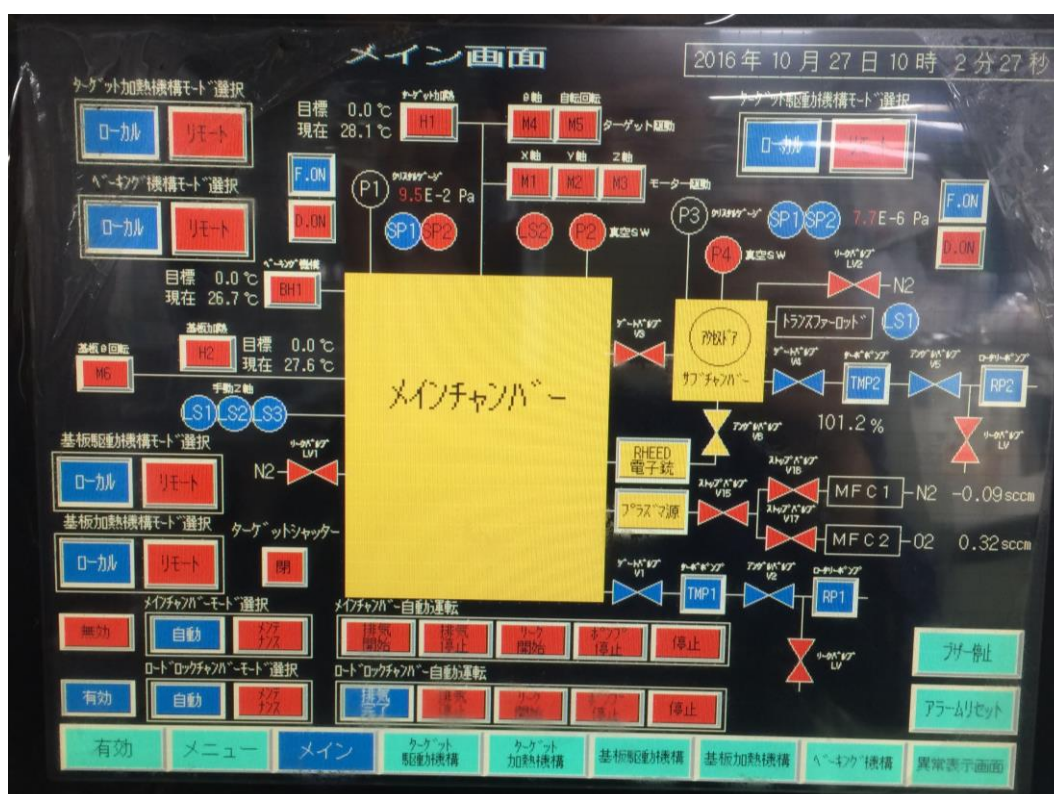


Figure 2.3 The view of the control panel.

### (3) Main chamber

The main chamber is equipped with rotary pump (RP) and turbo molecular pump (TMP) for evacuation. The pressure for the deposition is in the range from  $10^{-6}$  Pa to 10 Pa. Targets can revolve around the center of target rotation system and can also spin. In the growth process, one target is exposed and faced to the laser and the

substrate. The others are shield. The heater which is made from pyrolytic boron nitride (PBN) resistance is used to heat the samples. The temperature range can be adjusted from room temperature to 1200 °C. It has many advantages such as: low thermal mass, tailored thermal gradients for specific requirements and ultra-fast response, unaffected by vibration, thermally shock resistant, mechanically durable, high resistance for low cost power supplies, dimensionally and electrically stable, long life, liquids, chemically inert to most corrosive gases, and superior performance in ultra-high vacuum. The substrate can be heated by a surface contacted substrate holder that is on the heater.

#### (4) Preparation chamber

The preparation chamber is also equipped with RP and TMP for evacuation. Before the substrate is changed, the preparation chamber need be leaked with nitrogen. In order to keep the main chamber in vacuum when the load chamber is leaked, there is a valve between the preparation chamber and main chamber.

#### (5) Gas adjusting system

High purity nitrogen and oxygen are used to adjust the pressure of chambers during the film growth. The purity nitrogen is used for the leak of the preparation chamber and main chamber. The hafnium, neon, and krypton and helium are used for laser.

## **2.2 Characterization method**

### 2.2.1 X-ray diffraction

XRD can provide information on unit cell dimensions. It is a rapid non-destructive

technique that primarily used for obtaining the structural information of the material. The chemical composition, the crystallographic structure, and physical properties can be studied by observing the intensity of an X-ray beam hitting a sample as a function of incident angle. PANalytical X'Pert Materials Research XRD system was used for XRD measurement. This system can be used to investigate the structure of thin film, nanomaterials, and advanced semiconductors. A wide variety of X-ray scattering methods, such as nonambient analysis, stress, grazing incidence small angle X-ray scattering, wafer mapping, thin film phase analysis, and high resolution diffraction, can be carried out in this system. Compared the XRD diffractogram with the international center for diffraction data base, identification of the patterns can be achieved. Moreover, the crystalline quality can be evaluated by X-ray rocking curve.



Figure 2.4 The appearance of the XRD equipment.

### 2.2.2 Atomic Force Microscopy

A multi-mode scanning probe microscope (MM-SPM) was used in my work. MM-SPM can be used to be measured small samples by employing a series of interchangeable scanners and can provide images from the atomic scale to the size of about 175  $\mu\text{m}$ . A triangular probe is employed to scan the surface of the sample by measuring forces between the surface and the probe at a very short distance during the measuring process of AFM.

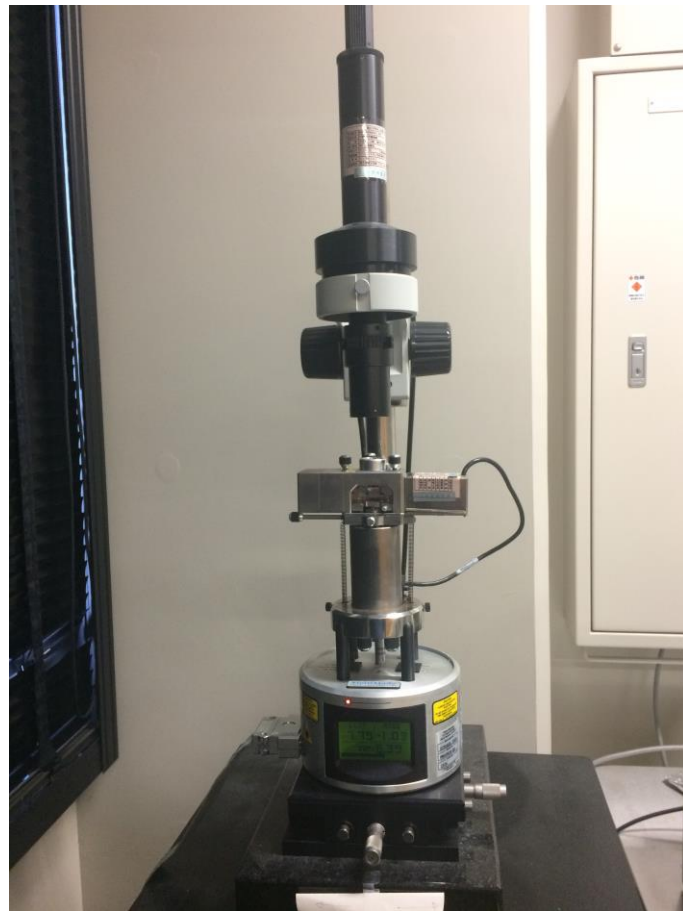


Figure 2.5 The appearance of the AFM equipment.

### 2.2.3 Scanning Electron Microscope

Scanning Electron Microscope (SEM) in our laboratory is Philips XL30 FED SEM.

It can be used to obtain the morphological information of materials. SEM with built-in energy-dispersive X-ray spectroscopy (EDS) analysis capability can be used to measure the component of samples. A field emission high resolution scanning electron microscope which can be carried out both at high acceleration voltage of 30 kV and low acceleration voltage of 200 V. The cathodoluminescence (CL) spectra can also be measured in SEM system by using an Oxford instrument monoCL system.



Figure 2.6 The appearance of the SEM equipment.

#### 2.2.4 Spectrophotometer

A Jasco V-570 spectrophotometer is used to measure the transmittance of films in our laboratory. This system has a double beam system with single monochromatic. The measured wavelength is in the range from 190 to 2500 nm with a wavelength

accuracy of 1.5 nm.

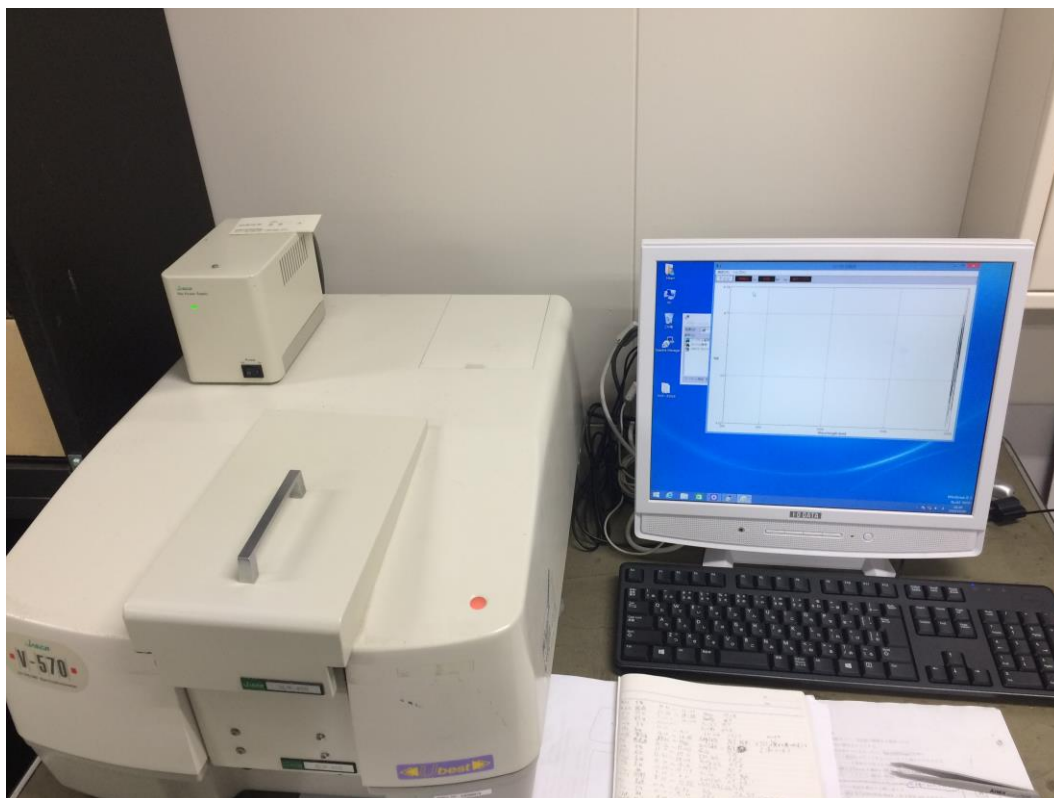


Figure 2.7 The appearance of the spectrophotometer equipment.

### 2.2.5 Raman devices

The Raman spectra were recorded in the back-scattering geometry of the  $z(x, -)\bar{z}$  configuration by using a Horiba Jobin Yvon LabRAM HR 800 system equipped with an Andor DU420 classic charge-coupled device detector. The 488 nm line of Ar laser was used to excite the samples. The employment of a  $50\times$  optical microscopy objective with a numerical aperture of 0.5 will yield a laser spot size of  $\sim 0.8\ \mu\text{m}$ . A Microstat<sup>HE</sup> hot/cold stage (Oxford instruments) with a quartz window was used to heat the samples from 77 K to 300 K under flowing nitrogen. The temperature was controlled by a K-type thermocouple which has an accuracy of better than  $\pm 1\ \text{K}$ . For

each measurement point, the temperature was kept for 10 min to avoid temperature fluctuations before acquiring a spectrum for 15 min.

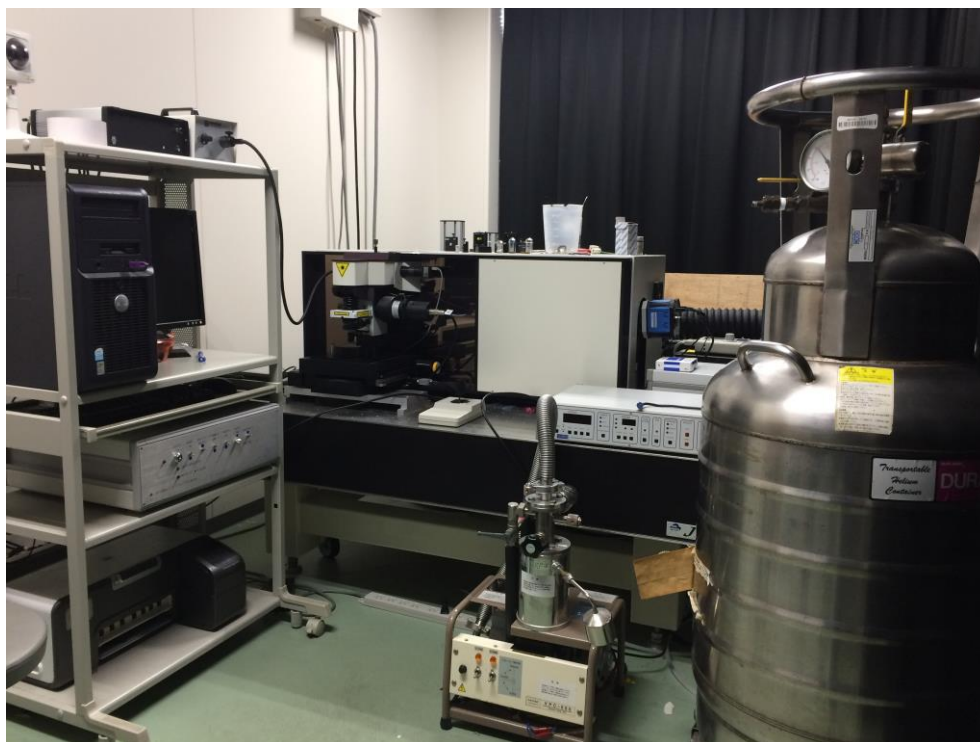


Figure 2.8 The appearance of Raman spectrometer.

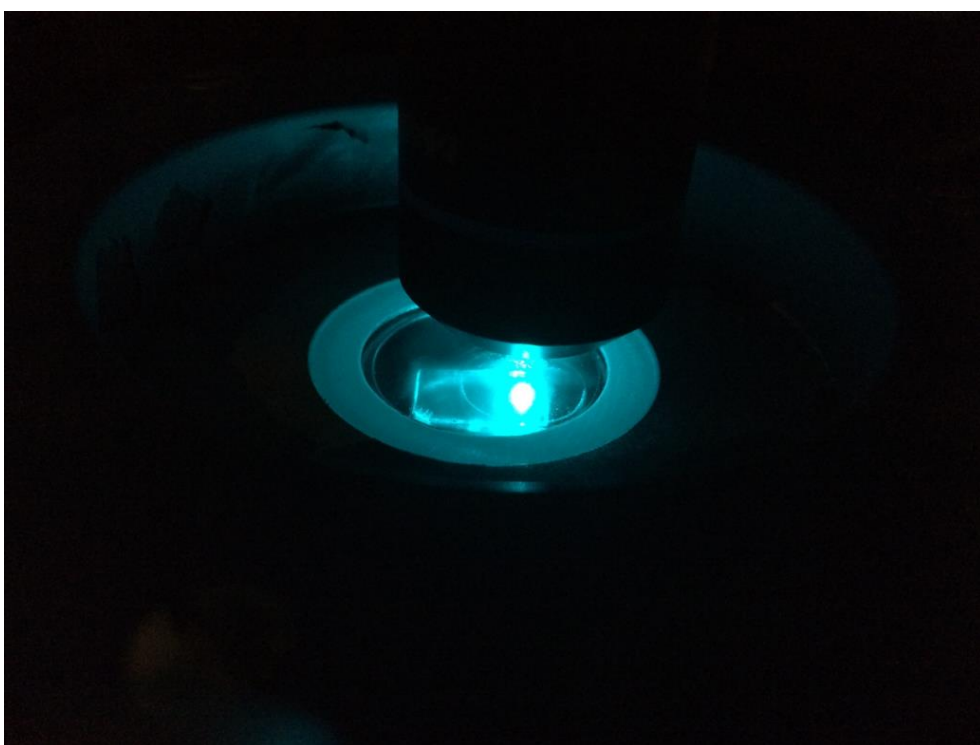


Figure 2.9 The photo taken in temperature-dependent Raman measurement

## Chapter 3

### Growth and characterization of MgZnO films

#### 3.1 Mg content influence

ZnO is an II-VI wide bandgap (3.37 eV) semiconductor with a large exciton binding energy of 60 meV. It is expected that alloying ZnO with MgO can tune the bandgap from 3.37 eV to 7.8 eV.<sup>1,2</sup> Therefore, MgZnO alloy material has received much attention due to their potential applications in the short-wavelength optoelectronic devices such as light-emitting diodes (LEDs) and laser diodes.<sup>3-6</sup>

Since the ionic radius of Mg<sup>2+</sup> (0.057 nm) is similar to that of Zn<sup>2+</sup> (0.060 nm), there can be some replacement in either structure without changing the original structure when alloying.<sup>7</sup> However, there is large crystal structure dissimilarity between wurtzite hexagonal ZnO and rock-salt-cubic MgO, which leads to unstable phase mixing. In the phase diagram of the ZnO-MgO binary system, the thermodynamic solubility limit of MgO in ZnO is only 4 at. % and MgO allows a maximum of 56 at. % ZnO solubility at 1600 °C.<sup>8</sup> Vashaei *et al.*<sup>9</sup> have tried to use plasma-assisted molecular-beam epitaxy (MBE) for growing MgZnO films over a wide Mg composition range from 0 to 0.97 and have found that phase separation occurs in MgZnO films with Mg content from 0.34 to 0.65. Similar results have been reported for the MgZnO films obtained by sputtering growth technique.<sup>10, 11</sup> Pulsed laser deposition (PLD) is an effective growth method for fabricating such metastable phase films due to the relative high kinetic energies that the ablated species have.<sup>12-14,</sup>

Using this method, Ohtomo *et al.* have succeeded in growing single phase wurtzite MgZnO films with Mg content up to 0.33.<sup>15</sup> In this paper, we report on the successful growth of single phase MgZnO films without phase separation in all Mg content range by PLD.

A series of MgZnO films were fabricated by PLD using a KrF laser source ( $\lambda = 248$  nm) on (0001) sapphire substrates. MgZnO bulks with different Mg content were used as targets. Before growth, the sapphire substrates were cleaned in organic solvents ultrasonically, chemically etched in a hot H<sub>2</sub>SO<sub>4</sub>:H<sub>3</sub>PO<sub>4</sub> (3:1) solution, then rinsed in deionized water. The pulsed laser with a frequency of 2 Hz was irradiated and the distance between targets and substrates was about 30 mm. Pure oxygen gas (99.999%) was introduced through mass flow controllers after the growth chamber was evacuated below  $5 \times 10^{-6}$  Pa. The oxygen pressure during the growth was maintained at  $1 \times 10^{-1}$  Pa while the substrate temperatures were kept at 400 °C or 500 °C. The deposition time was 40 min for all samples.

The element contents in the prepared MgZnO films were determined by energy dispersive X-ray spectroscopy (EDS). The thicknesses of the MgZnO films were measured by using a surface step profile analyzer. The crystal structures of the layers were examined by conventional  $\theta$ - $2\theta$  XRD using Cu K $\alpha$  emission line. The optical transmission spectra were measured with a spectrophotometer at room temperature.

Figure 3.1(a) and (b) show the EDS of MgZnO films grown using various Mg content in the targets ( $x$ ) at substrate temperature of 400°C and 500°C, respectively. From the spectra, elements of O, Zn, Mg, and Al are observed. The peak related to Al

is attributed to the sapphire substrate due to the thickness of the films were smaller than 600 nm. It is obvious that the intensity ratio of Mg/Zn in the MgZnO films increases with the increase of Mg content in the targets both for substrate temperatures of 400 and 500 °C.

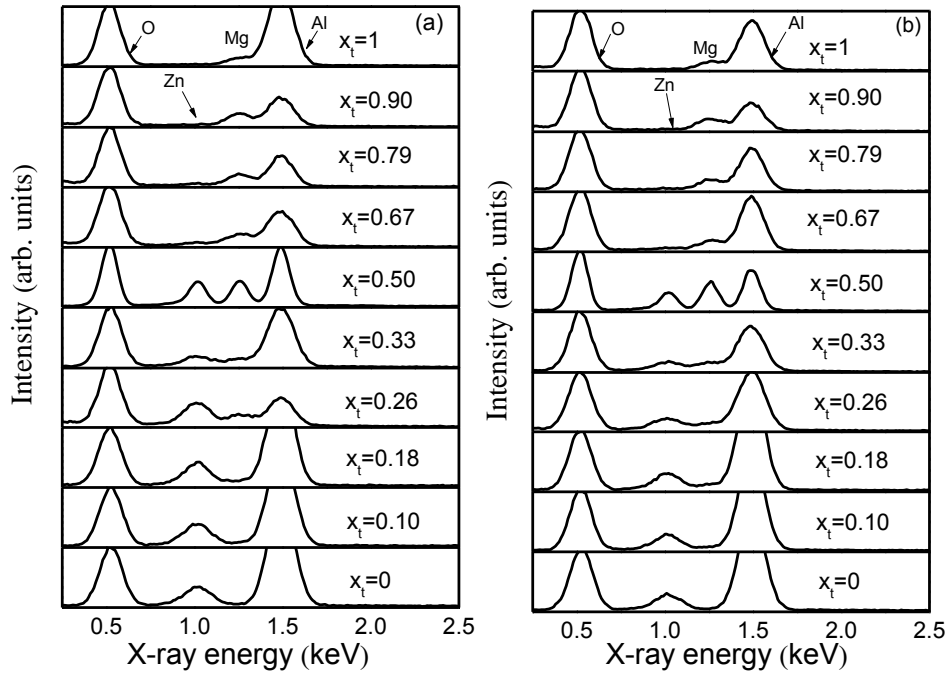


Figure 3.1 EDS of MgZnO films grown at substrate temperatures of (a) 400 °C and (b) 500 °C by using MgZnO targets with various Mg content  $x$ .

Figure 3.2 presents the dependence of Mg content  $x$  in MgZnO films obtained from the EDS spectra on Mg content in the MgZnO targets. The Mg content in the films increases almost linearly with the increase of Mg content in the targets, suggesting the composition of MgZnO films can be controlled by adjusting Mg content in the targets. From Fig. 3.13, it is clear that the Mg content in the MgZnO films grown at substrate temperature of 400 °C is smaller than that of MgZnO films grown at substrate temperature of 500 °C for same Mg content in the MgZnO targets, indicating that

substrate temperature is also an important parameter to affect the composition of MgZnO films in the PLD process.

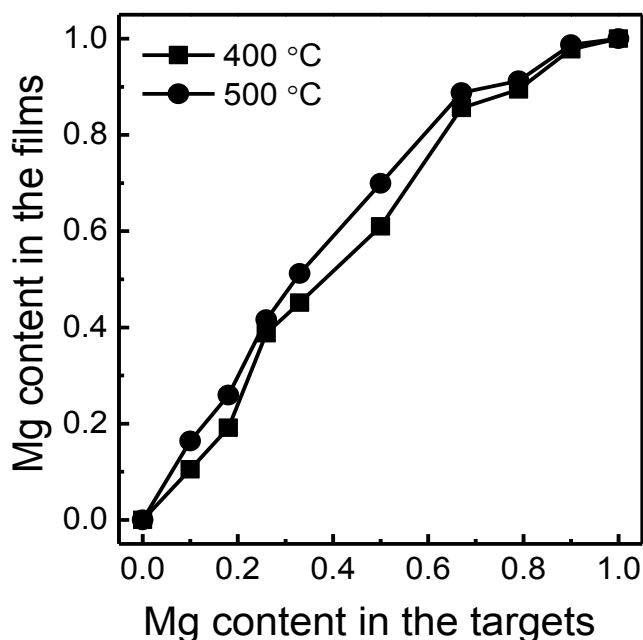


Figure 3.2 Dependence of the Mg content in the MgZnO films grown at the substrate temperatures of 400 °C and 500 °C on the Mg content in the MgZnO targets.

Choopun *et al.*<sup>16</sup> have fabricated MgZnO films onto c-plane sapphire by PLD. The Mg content is range from 0.5 to 1 by controlling the substrate temperature from room temperature to 750 °C using one MgZnO target with Mg content of 0.5. This phenomenon can be explained by the difference of vapor pressure between Mg and Zn species. Zn species have a higher vapor pressure and can be desorbed more easily than that of Mg species at same growth temperature which results in the more Mg enriched films at high growth temperatures. In order to verify this phenomenon, we investigated the growth rate of MgZnO films at the substrate temperature 400 °C and 500 °C as shown in figure 3.3. The growth rate of the MgZnO films grown at the

substrate temperature 500 °C is clearly lower than that at 400 °C for a given MgZnO target in the low Mg content region due to the Zn desorption. However, the growth rates for both of substrate temperature 400 °C and 500 °C are almost same in the high Mg content region. The results are consistent with that reported by Choopun *et al.*<sup>16</sup>.

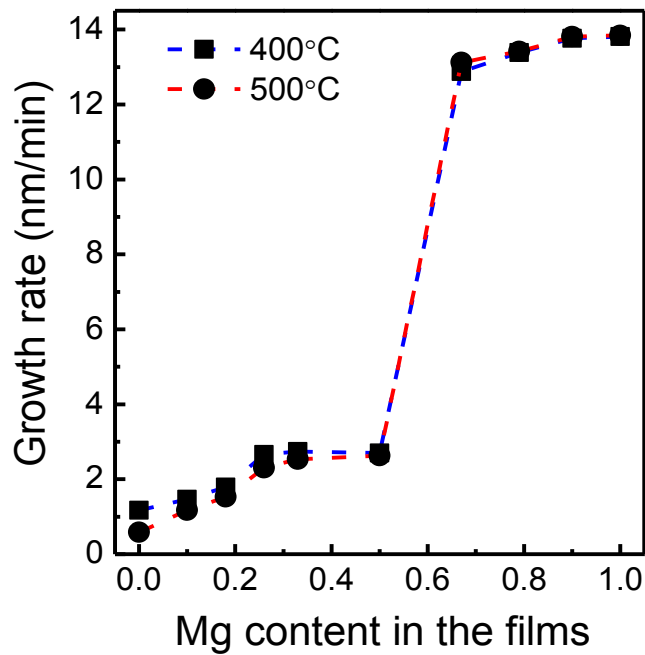


Figure 3.3 Dependence of the growth rate of MgZnO films grown at the substrate temperatures of 400 °C and 500 °C on the Mg content in the MgZnO targets.

Figure 3.4(a) shows the XRD patterns of MgZnO films deposited on (0001) sapphire substrates at substrate temperature of 400 °C. When the Mg content in the target is lower than 0.26, the (0002) diffraction peaks of MgZnO films are observed together with the peak of (0006) reflection from sapphire substrate. None of the (100), (101) and (102) peaks of MgZnO film can be detected within the searched angle ( $30^\circ \leq 2\theta \leq 80^\circ$ ), indicating that the grown MgZnO films are highly *c*-axis oriented

and wurtzite in structure. With the increase of Mg content, this peak has a weak right shift as shown in figure 3.5(a), which reflects the decrease of  $c$ -axis length. This is caused by the  $Mg^{2+}$  incorporation into ZnO lattice since the ionic radius of  $Zn^{2+}$  (0.060 nm) is slightly longer than that of  $Mg^{2+}$  (0.057 nm).<sup>25</sup> The appearance of (111) and (222) diffraction peaks of MgZnO films for Mg target content above 0.33 is a sign of single cubic phase as shown in figure 3.4(a). The (111) peak at around  $2\theta = 36.4^\circ$  is close to that of MgO.<sup>18</sup> With the increase of Mg content, the  $a$ -axis length of cubic MgZnO films reduces gradually, resulting in right shift of the (111) peak as shown in figure 3.5(a).

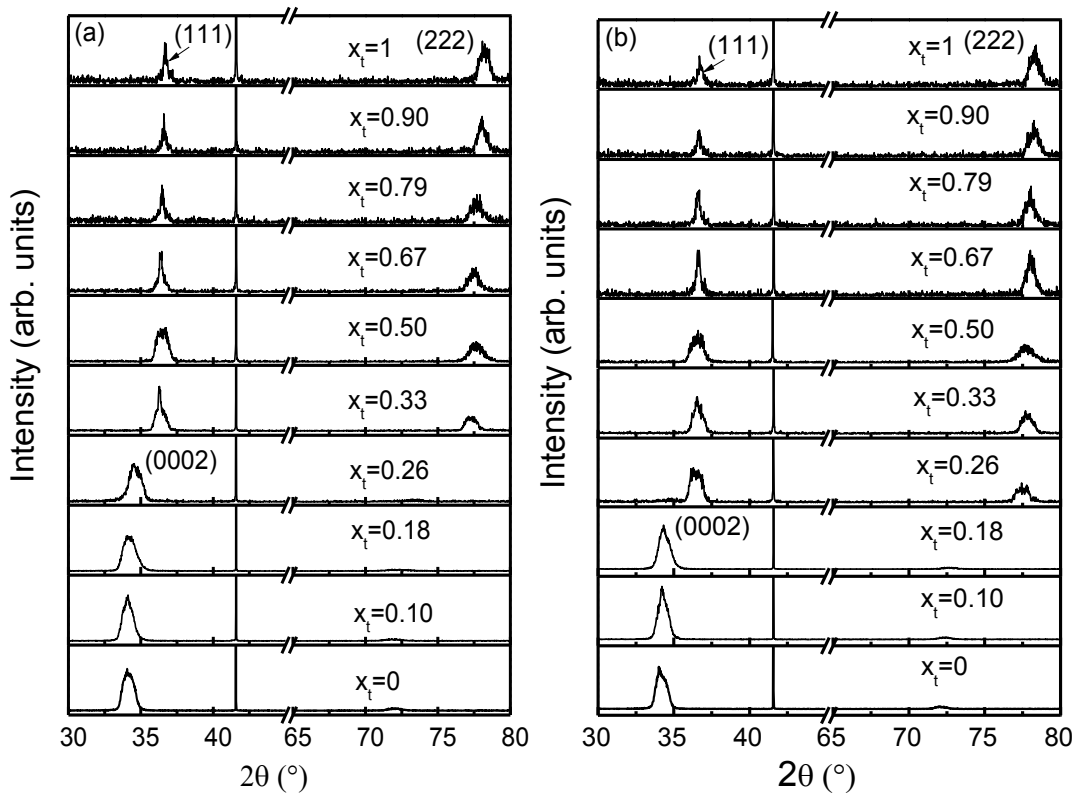


Figure 3.4 XRD patterns of the MgZnO films grown at substrate temperatures of (a) 400 °C and (b) 500 °C by using MgZnO targets with various Mg content  $x$ .

Figure 3.4(b) shows the XRD patterns of MgZnO films deposited on (0001)

sapphire substrates at substrate temperature of 500 °C. It has the similar tendency with figure 3.4(a). However, it is clear that when the Mg target content is 0.26, the MgZnO films grown at 500 °C has cubic structure while the MgZnO films grown at 400 °C is of hexagonal structure. This difference is due to the different Mg content in the MgZnO films (0.42 for 500 °C and 0.39 for 400 °C) as shown in figure 3.2. Based to figure 3.2 and 3.4, it is obvious that the phase transformation from hexagonal wurtzite to cubic structure occurs in the Mg content between 0.39 and 0.42. According to the phase diagram of the MgZnO alloy system, the MgZnO films can keep stable hexagonal phase in a solid solution state when the Mg content is in the range  $0 \leq x \leq 0.04$  and the cubic phase has the Mg content range of  $0.56 \leq x \leq 1$ . When the Mg content  $x$  is outside these two ranges, a mixed phase is observed.<sup>19</sup> However, it is known that the solid solubility can be significantly modified in films form, and it is also influenced by the growth conditions. For example, Ohtomo *et al.*<sup>15</sup> have demonstrated that the MgZnO films which have a single hexagonal phase can be prepared by PLD with the Mg content up to 0.33 at a temperature of 600 °C. Using the same technique Yang *et al.*<sup>20</sup> reported the single hexagonal phase is in the Mg content range of 0-0.34 at substrate temperature of 750 °C. Takeuchi *et al.*<sup>21</sup> have fabricated MgZnO films by PLD at substrate temperature of 600 °C and found the phase separation region of the phase diagram in the range of  $0.37 \leq x \leq 0.6$ . In our work, the lower substrate temperatures (400 and 500 °C) lead kinetics instead of thermodynamics dominate the growth process. Thus most radicals do not have enough energy to reach their energy-minimum sites,<sup>22</sup> which results in the almost no phase

separation observed in our MgZnO films.

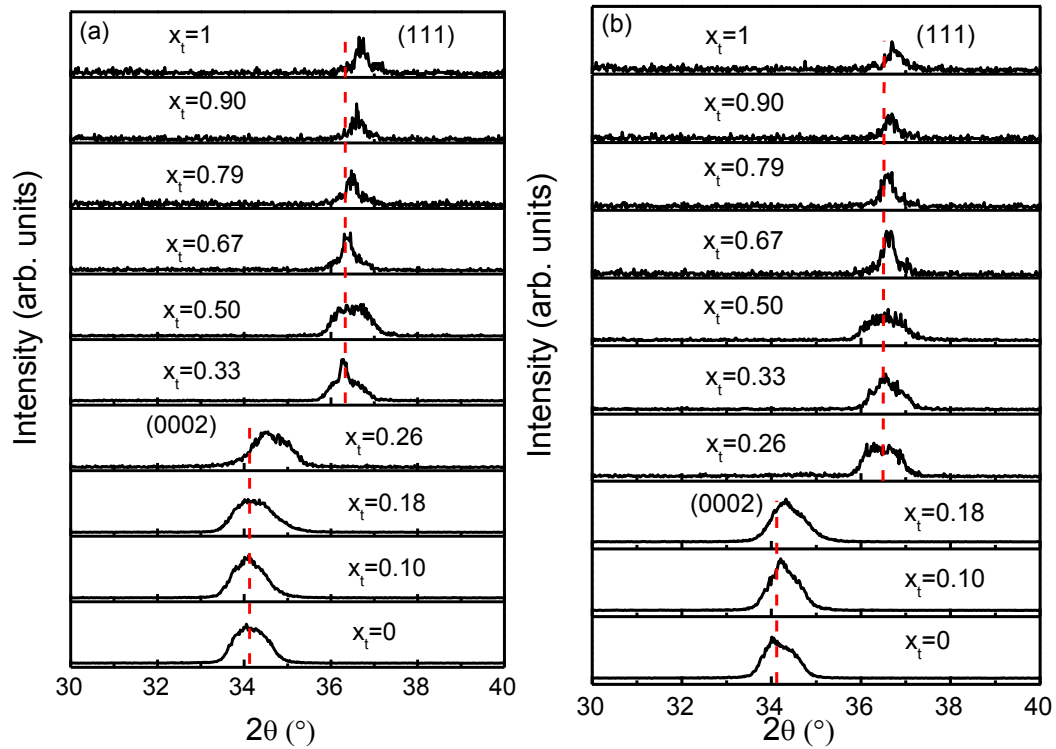


Figure 3.5 Enlarged XRD patterns of the single MgZnO films grown at substrate temperatures of (a) 400 °C and (b) 500 °C.

The transmittance spectra of typical MgZnO films are obtained as shown in figure 3.6. The transmittances of the MgZnO films in all Mg content range are above 80% in the wavelength range from 400 to 1000 nm. The absorption edges of the MgZnO films have a shift to short wavelength direction with the increase of Mg content.

It is well known that for layers with direct bandgap, the absorption follows a power law of the form:

$$(\alpha hv) = A(hv - E_g)^{1/2}$$

Where  $hv$  is the energy of the incident photon,  $\alpha$  is the absorption coefficient,  $A$  is the absorption edge width parameter, and  $E_g$  is the bandgap. The optical absorption

coefficient  $\alpha$  of the layers is evaluated using the standard relation taking the film thickness into account. The plot of  $(\alpha h\nu)^2$  as a function of photon energy is shown in figure 3.7. The absorption coefficient increases rapidly at the photon energy range around 3.31-5.9 eV depending on the Mg content  $x$ , and  $(\alpha h\nu)^2$  as a function of  $h\nu$  fits the straight line quite well, indicating that the obtained MgZnO films are of direct transition. The bandgap value about 3.31eV with Mg content  $x = 0$  agrees with that of bulk ZnO.<sup>15</sup>

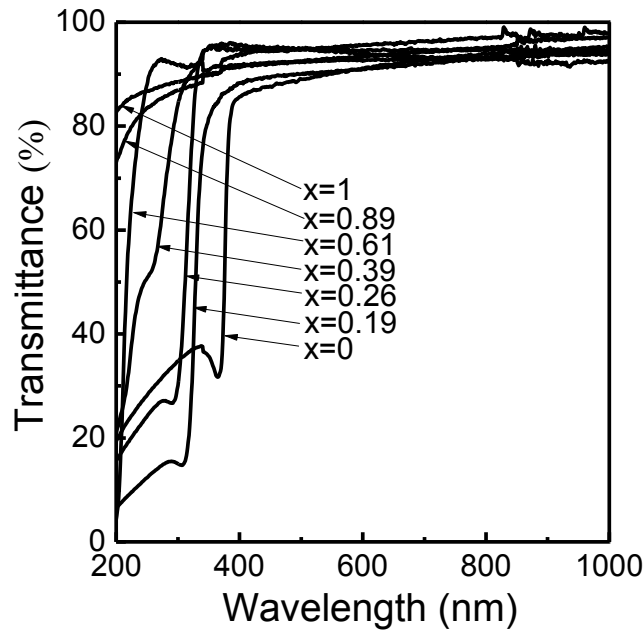


Figure 3.6 Transmittance spectra of typical MgZnO films with Mg content  $x$  in the films.

Figure 3.8 is the summary of the bandgap energy as a function of Mg content in the films. For comparison, the bandgaps of MgZnO films reported by previous researches in Refs. 15 and 16 are also shown in the figure. The bandgaps in our work have the similar result with that reported by other groups in the Mg content ranges of 0-0.26 and 0.5-0.70. However, the bandgaps of single phase MgZnO films grown by PLD with the Mg content from 0.33-0.5 are reported for the first time due to almost no phase separation region as shown in figure 3.8. The result indicates that the bandgap of MgZnO film can be controlled by adjusting the Mg content in the films.

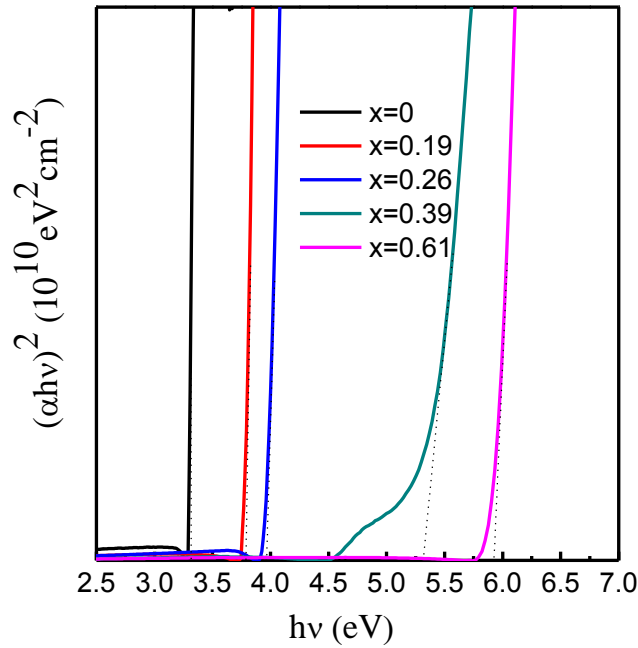


Figure 3.7  $(\alpha hv)^2$  vs.  $hv$  plot of MgZnO films with different Mg content  $x$ .

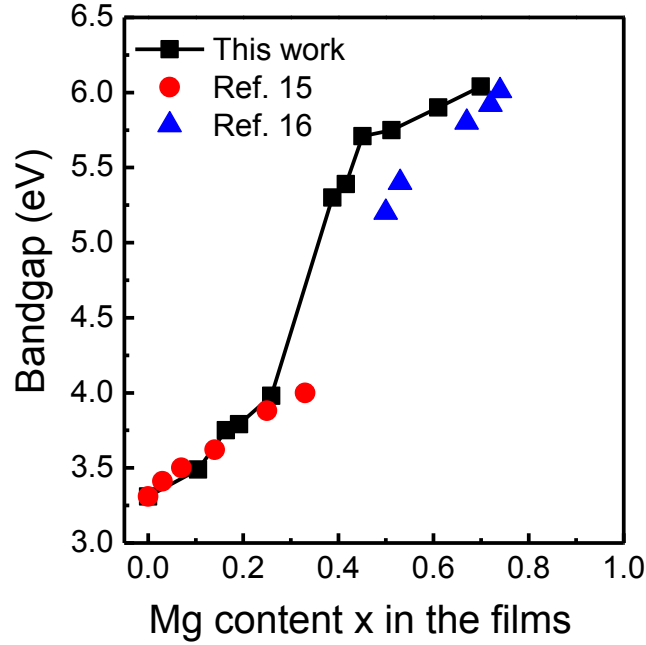


Figure 3.8 Dependence of the bandgap of MgZnO on Mg content  $x$  in the films.

### 3.2 Substrate temperature influence

MgZnO films were prepared by PLD using a KrF laser source ( $\lambda=248\text{nm}$ ) on  $c$ -plane sapphire substrates. Before the deposition, the sapphire substrates were cleaned in carbinol solution and acetone solution by an ultrasonic cleaning system, and then chemically etched in a hot  $\text{H}_3\text{PO}_4:\text{H}_2\text{SO}_4$  (1:3) solution. In the growth chamber, facing the substrate the  $\text{Mg}_x\text{Zn}_{1-x}\text{O}$  alloys target was set. The Mg composition in the target was 0.5. The pulsed laser with a frequency of 2 Hz was irradiated and the distance between target and substrate was about 30 mm. The laser energy was set 190 mJ. The oxygen pressure of the growth chamber was  $1 \times 10^{-1}$  Pa by introducing high purity oxygen gas (99.999%). In the deposition, the substrate temperature was varied from room temperature (RT) to 500 °C. The deposition time was 40 min for all the layers.

The composition of MgZnO films were determined by energy dispersive EDS. The

thickness of the films was measured by using a surface step profile analyzer. The structural properties of the films were examined by conventional  $\theta$ - $2\theta$  XRD. The optical transmission spectra were measured with a spectrophotometer. The surface morphology and roughness were studied by atomic force microscope (AFM).

Figure 3.9 shows the EDS of MgZnO films which were grown on *c*-plane sapphire substrates at different substrate temperatures. In the spectra the elements of oxygen, zinc, magnesium and aluminum have been observed. When the substrate temperature was below 200 °C, the Mg content in the MgZnO films were almost same. And it was obvious that the Mg content increased with the increase of substrate temperature when the substrate temperature was higher than 300 °C. Figure 3.10 shows the dependence of Mg content in the Mg<sub>x</sub>Zn<sub>1-x</sub>O films on the substrate temperature. At the low substrate temperature, the Mg content in the Mg<sub>x</sub>Zn<sub>1-x</sub>O films was equal to that in the target. The rise started from 300 °C. The Mg content in the film was linear growth with the increase of the substrate temperature by a slope factor of 0.00063. The content variation between film and target can be owing to the difference of vapor pressure between Zn and Mg species at higher substrate temperatures. Zn-related species have a higher vapor pressure and are easily desorbed at higher substrate temperatures. It leads to Mg enrichment on the substrates.

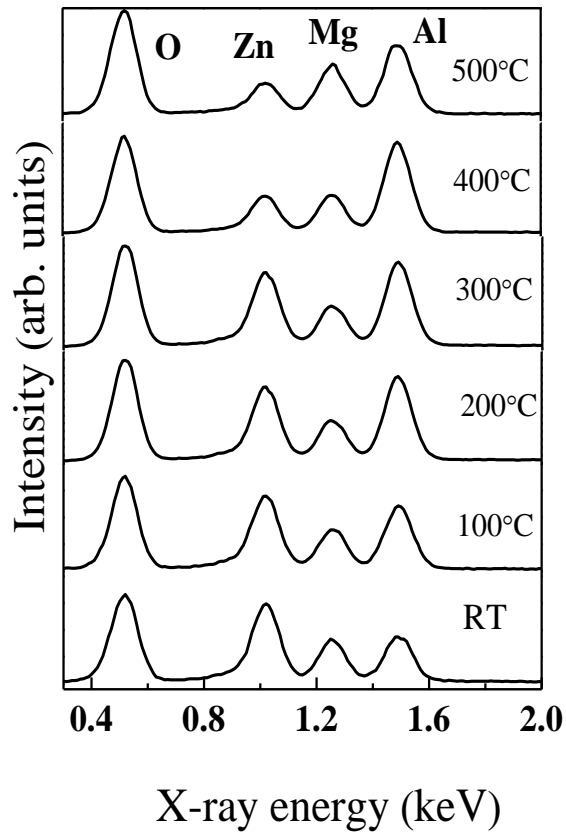


Figure 3.9 EDS of MgZnO films grown at different substrate temperatures.

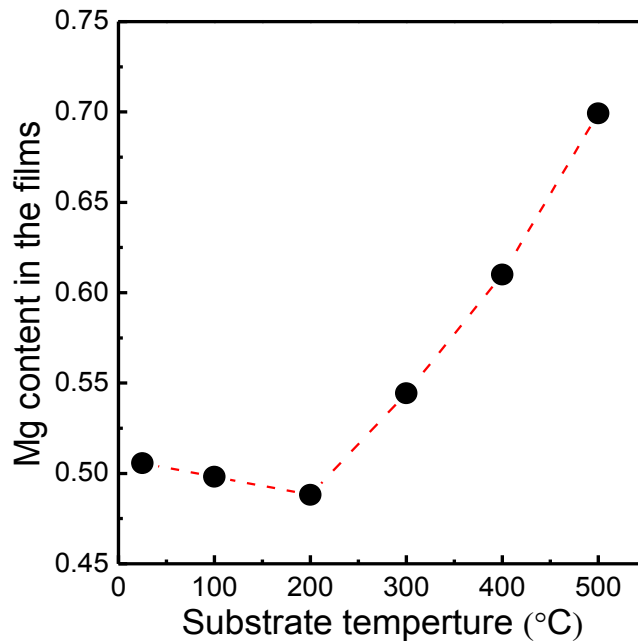


Figure 3.10 Dependence of the Mg content in MgZnO films grown at different substrate temperatures on the Mg content in the MgZnO targets.

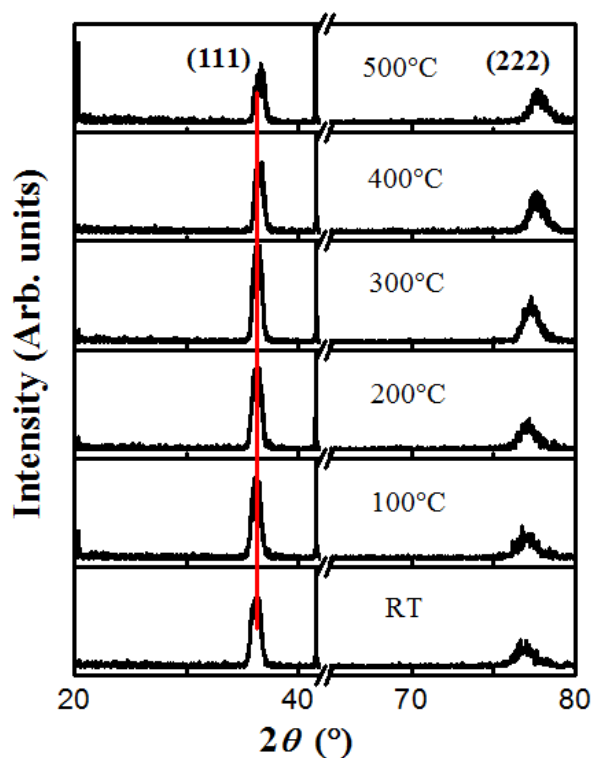


Figure 3.11 XRD patterns of the MgZnO films at different substrate temperatures.

Figure 3.11 shows the variation of the XRD patterns of MgZnO films which were grown on *c*-plane sapphire at different substrate temperature. The pure cubic phase MgZnO films were observed. The cubic MgZnO peaks appeared at the  $2\theta$  values of around  $36.26^\circ$  and  $76.87^\circ$ , corresponding to the lattice orientation (111) and (222). There was no phase segregation observed. The (111) peaks had a weak right shift with the increase of substrate temperature. The shift was more obvious to observe for the lattice orientation (222). This right shift can be ascribed to the increase of the Mg content in the films with the increase of substrate temperature.

Figure 3.12 is the growth rate of MgZnO films grown with different substrate temperatures. The thickness of MgZnO films were around 150 nm at the low substrate

temperatures. The growth rate was about 3.7 nm/min. And the thickness started to reduce from 300°C with a growth rate of 3.15 nm/min. While the substrate temperature was above 400°C, the thickness was about 105 nm and the growth rate was about 2.63 nm/min. The decline of the thickness was attributed to the release of the Zn at the high substrate temperature.

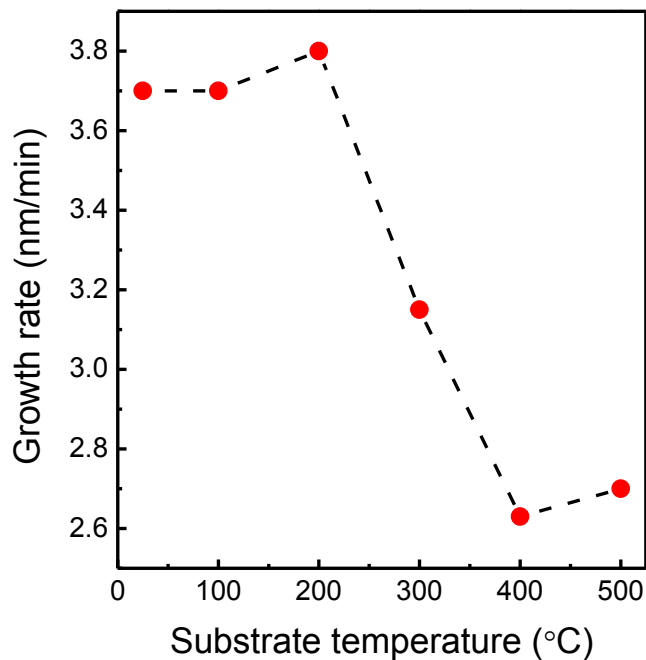


Figure 3.12 Growth rates of MgZnO films grown with different substrate temperatures

Figure 3.13 is the AFM morphologies of the cubic MgZnO films grown at different substrate temperatures. The surface of  $Mg_xZn_{1-x}O$  films were smooth at the substrate temperature below 200 °C. The crystal islands were observed with the temperature increasing to 300 °C. The diameter of the crystal islands grew with increasing the substrate temperature.

Figure 3.14 is the roughness of MgZnO films prepared at different substrate

temperatures. The roughness of MgZnO films increases almost linearly with the increase of the substrate temperature above 100 °C, and it was in the range from 0.3 to 0.65 nm with different substrate temperatures.

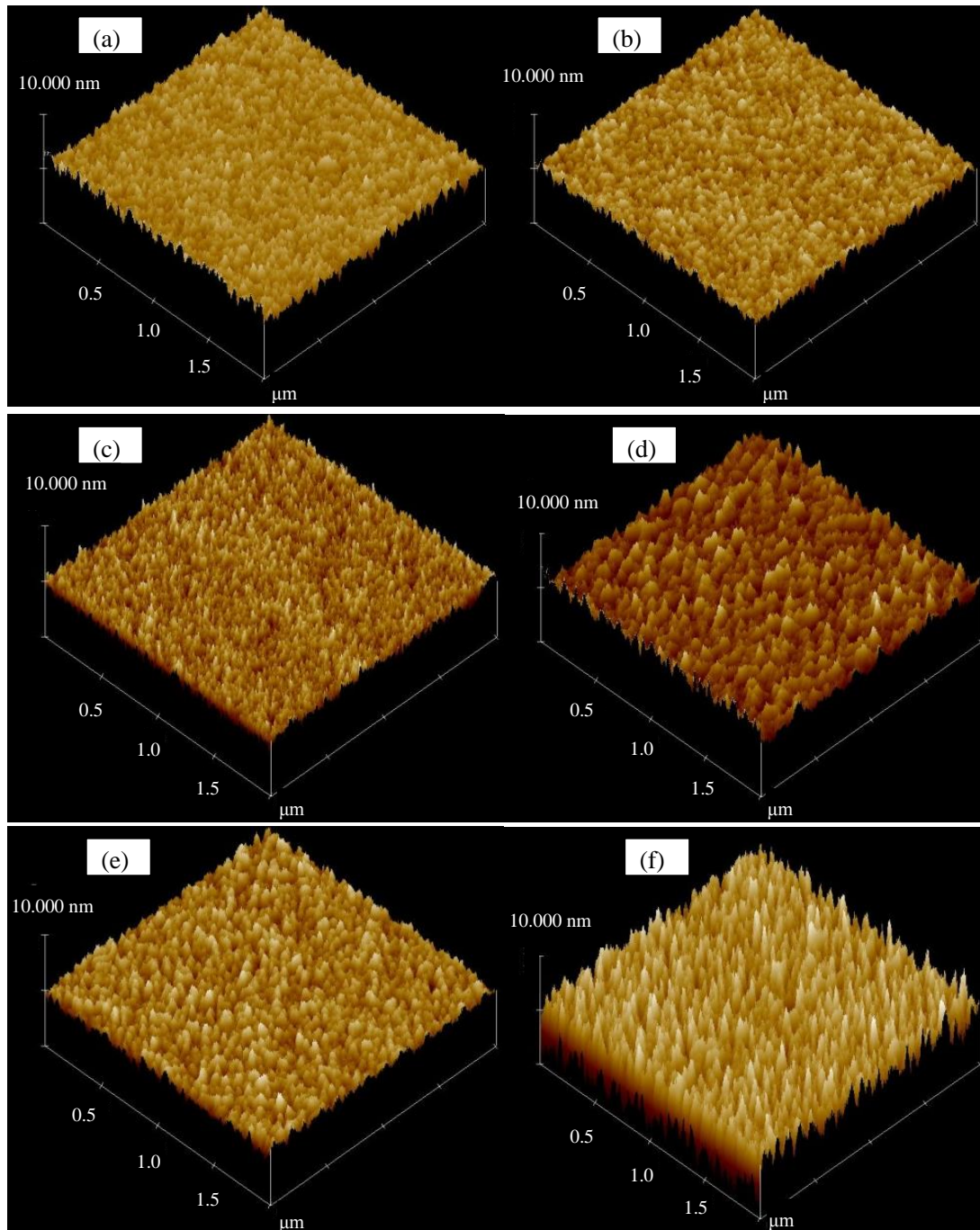


Figure 3.13 AFM images of MgZnO films grown at substrate temperatures of (a) room temperature, (b) 100 °C, (c) 200 °C, (d) 300 °C, (e) 400 °C, and (f) 500 °C, respectively.

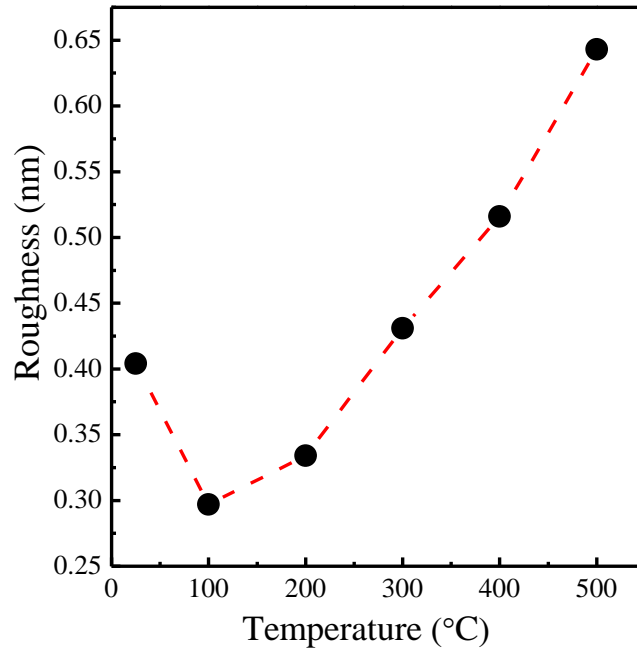


Figure 3.14 Roughness of MgZnO films prepared at different substrate temperatures.

The transmittance spectra of the cubic  $Mg_xZn_{1-x}O$  films which prepared different substrate temperatures by PLD were plotted in Figure 3.15. The transmittances of all the films were above 80% in the visible and infrared regions. The absorption edges were observed below 213 nm in deep ultraviolet region, and it is shifted to shorter wavelength direction. The band gaps of the cubic  $Mg_xZn_{1-x}O$  films can derive from a plot of  $(ahv)^2$  as a function of photon energy  $hv$ , showed in Figure 3.16. The range of bandgap changed from 5.15 to 6.07 eV depending on substrate temperature.

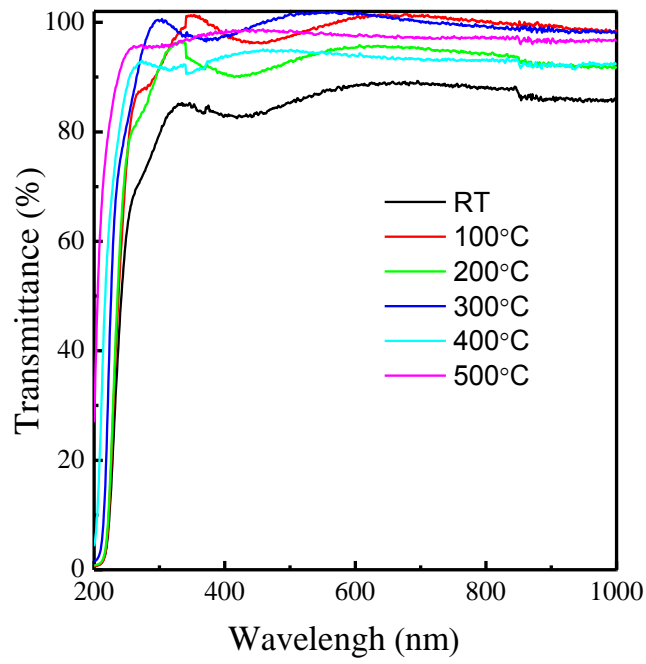


Figure 3.15 Transmittance spectra of MgZnO films grown at different substrate temperatures.

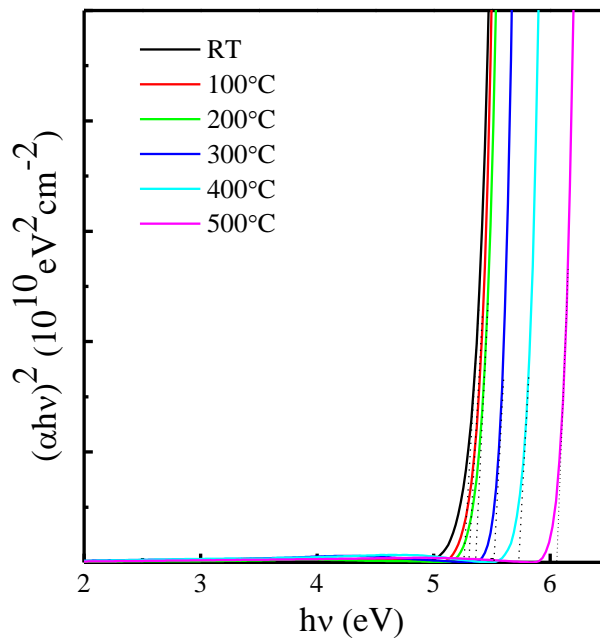


Figure 3.16  $(\alpha h\nu)^2$  vs.  $h\nu$  plot of MgZnO films grown with different substrate temperatures.

### 3.3 Oxygen pressure influence

MgZnO films were prepared by PLD using a KrF laser source ( $\lambda=248\text{nm}$ ) on *c*-plane sapphire substrates. Before the deposition, the sapphire substrates were cleaned in carbinol solution and acetone solution by an ultrasonic cleaning system, and then chemically etched in a hot  $\text{H}_3\text{PO}_4: \text{H}_2\text{SO}_4$  (1:3) solution. In the growth chamber, facing the substrate the  $\text{Mg}_x\text{Zn}_{1-x}\text{O}$  alloys target was set. The Mg content in the target was 0.5. The pulsed laser with a frequency of 2 Hz was irradiated and the distance between target and substrate was about 30 mm. The laser energy was set 190 mJ. The oxygen pressure of the growth chamber was from  $10^{-4}$  to  $10^{-1}$  Pa by introducing high purity oxygen gas (99.999%). In the deposition, the substrate temperature was 400 °C. The deposition was 40 min for all the layers.

The structural properties of the films were examined by conventional  $\theta$ - $2\theta$  XRD. The optical transmission spectra were measured with a spectrophotometer.

Figure 3.17 shows the XRD patterns of MgZnO films deposited on (0001) sapphire substrates at different oxygen pressures. The (111) diffraction peaks of MgZnO films are observed together with the peak of (0006) reflection from sapphire substrate. None of the (100), (101) and (102) peaks of MgZnO film can be detected within the searched angle ( $30^\circ \leq 2\theta \leq 80^\circ$ ), indicating that the grown MgZnO films are highly *c*-axis oriented and wurtzite in structure. The (111) diffraction peaks have no obvious shift with the increase of oxygen pressure, which indicates that oxygen pressure in the range from  $10^{-4}$  to  $10^{-1}$  Pa has a minimal effect on the structure of MgZnO films.

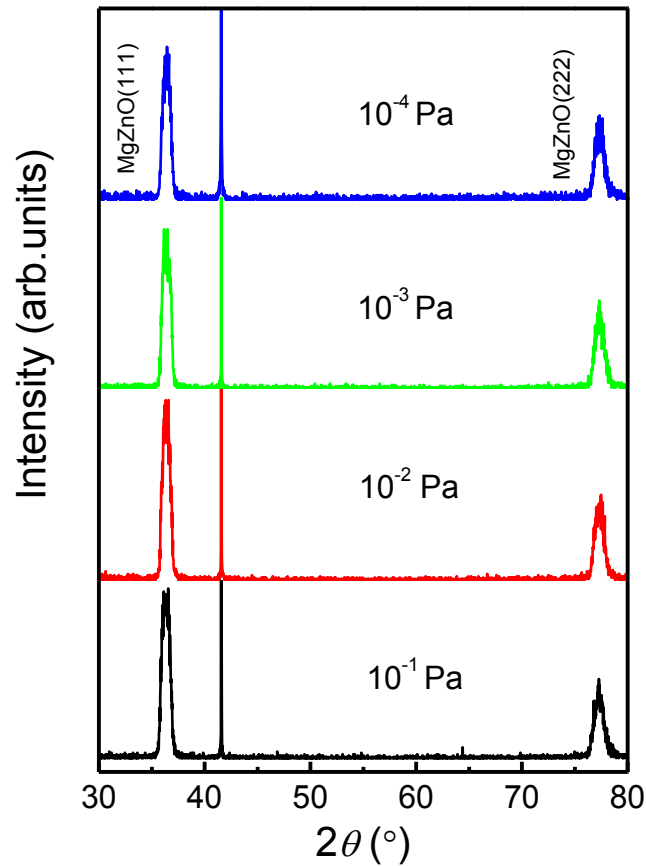


Figure 3.17 XRD patterns of the MgZnO films grown on the c-plane sapphire at different oxygen pressures.

The transmittance spectra of MgZnO films prepared at different oxygen pressures were plotted in Figure 3.18. The transmittances of all the layers were above 80% in the visible and infrared regions. The absorption edges were observed in deep ultraviolet region, and it has a small shift with the increase of oxygen pressure. The band gaps of MgZnO films at different oxygen pressures can derive from a plot of  $(ah\nu)^2$  as a function of photon energy  $h\nu$ , as shown in Figure 3.19. The bandgap energy of MgZnO films increases from 5.63 to 5.88 eV with the decrease of the oxygen pressure.

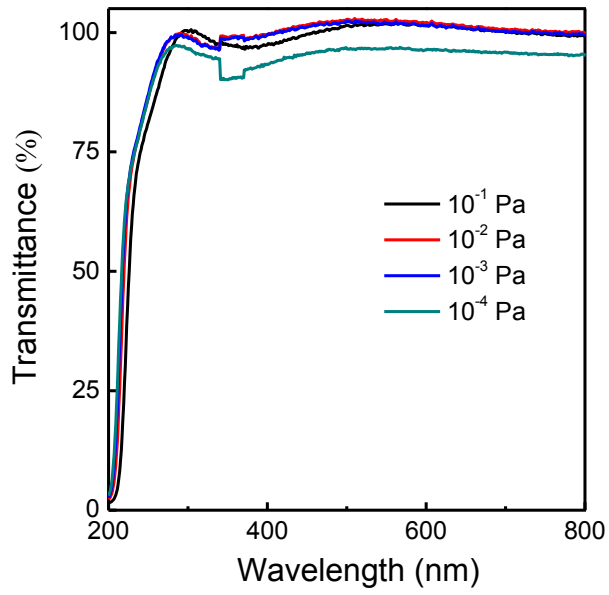


Figure 3.18 Transmittance spectra of MgZnO films grown at different oxygen pressures.

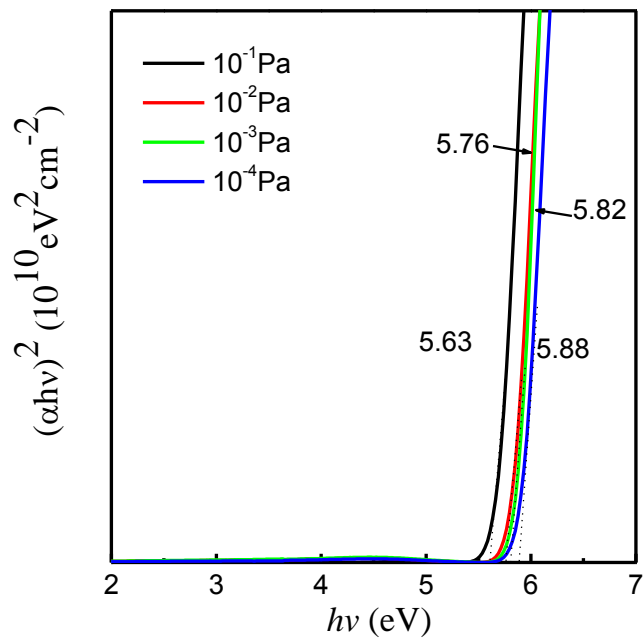


Figure 3.19  $(\alpha h\nu)^2$  vs.  $h\nu$  plot of MgZnO films grown with different substrate temperatures.

### 3.4 Conclusion

In this chapter, we have reported the Mg content, substrate temperature, and oxygen pressure on the structure and optical properties of MgZnO films grown by PLD. The following conclusions were summarized.

(1) The growth of crystalline MgZnO films on sapphire (0001) substrate by PLD has been shown. The Mg content  $x$  can be controlled by changing target Mg content and substrate temperature. Single phase MgZnO films are obtained in all Mg content range. The phase transformation from hexagonal to cubic phase is determined at the Mg content around 0.4. Optical analysis indicates that the bandgaps of MgZnO films can be tailored by controlling the Mg content in the films.

(2) The XRD patterns illustrated that the cubic phase (111) and (222) peaks appeared at the  $2\theta$  values of about  $36.26^\circ$  and  $76.87^\circ$ , and the  $\text{Mg}_x\text{Zn}_{1-x}\text{O}$  film with good crystal quality can be obtained at a substrate temperature of  $400^\circ\text{C}$ . The bandgaps of the pure cubic  $\text{Mg}_x\text{Zn}_{1-x}\text{O}$  layers were increased from 5.15 to 6.07 eV with increasing the substrate temperature. Moreover, the roughness of the cubic  $\text{Mg}_x\text{Zn}_{1-x}\text{O}$  films was negligible.

(3) The (111) diffraction peaks have no obvious shift with the increase of oxygen pressure, which indicates that oxygen pressure in the range from  $10^{-4}$  to  $10^{-1}$  Pa has a minimal effect on the structure of MgZnO films. The bandgap energy of MgZnO films increases from 5.63 to 5.88 eV with the decrease of the oxygen pressure.

## Reference

- [1] A.K. Sharma, J.Narayan, J.F. Muth, C.W. Teng, C.Jin, A. Kvit, R.M. Kolbas, and O.W. Holland, *Appl, Phys. Lett.*, 75, 3327 (1999).
- [2] J.W. Kim, H.S. Kang, J.H. Kim, S.Y. Lee, J.K. Lee, and M. Nastasi, *J. Appl. Phys.*, 100, 033701 (2006).
- [3] T. Makino, A. Obhtomo, C.H. Chia, Y. Segawa, H. Koinuma, and M. Kawasaki, *Physical E*, 216,71 (2004).
- [4] A. Ashrafi. *Appl, Phys. Lett.*, 107, 123527 (2010).
- [5] M. Stolzel, A. Muller, G. Benndorf, M. Brandt, M. Lorenz, and M. Grundmann, *Phy. Rev. B.*, 88, 045315 (2013).
- [6] H.Y. Chen, K.W. Liu, M.M. Jiang, Z.Z. Zhang, X.H. Xie, D.K. Wang, L. liu, B.H. Li, D.X. Zhao, C.X. Shan, and D.Z. Shen, *Appl. Phys. Lett.*, 104, 091119 (2014).
- [7] A. Ohtomo, M. Kawasaki, I. Ohkubo, *Appl. Phys. Lett.*, 75, 980 (1999).
- [8] E.R. Segnit, and A.E. Holland, *J. Am. Ceram. Soc.*, 48, 409 (1965).
- [9] Z. Vashaei, T. Minegishi, H. Suzuki, T. Hanada, M. W. Cho, T. Yao, and A. Setiawan, *J. Appl. Phys.*, 98, 054911 (2005).
- [10] D. Thapa, J. Huso, H. Che, M. Huso, J.L. Morrison, D. Gutierrez, M.G. Norton, and L. Bergman, *Appl. Phys. Lett.*, 102, 191902 (2013).
- [11] J. Huso, H. Che, D. Thapa, J.L. Morrison, M.G. Norton, and L. Bergman, *Appl. Phys. Lett.*, 104, 031908 (2014).
- [12] X.Q. Gu, Y. L. Zhao, Y. H. Qiang, *Superlattice Microstruct.*, 61, 168 (2013).
- [13] F.B. Zhang, K. Saito, T. Tanaka, M. Nishio, Q.X. Guo, *J. Cryst. Growth*, 387, 96

(2014).

[14] F.B. Zhang, K. Saito, T. Tanaka, M. Nishio, Q.X. Guo, *Solid State Commun.*, 186 28 (2014).

[15] A. Ohtomo, M. Kawasaki, T. Koida, K. Masubuchi, H. koinuma, Y. Sakurai, Y. Yoshida, T. Yasuda, and Y. Segawa, *Appl. Phys. Lett.*, 72, 2466 (1998).

[16] S. Choopun, R.D. Vispute, W. Yang, R.P. Sharma, T. Venkatesan, and H. Shen, *Appl. Phys. Lett.*, 80, 1529 (2002).

[17] C.Y. Liu, H.Y. Xu, L. Wang, X.H. Li, and Y.C. Liu, *J. Appl. Phys.*, 106, 073518 (2009).

[18] J.G. Yoon, and K. Kim, *Appl. Phys. Lett.*, 66, 2661 (1995).

[19] E.M. Levin, C.R. Robbins, H.F. McMurdie, M.K. Reser, *American Ceramic Society, Columbus, Ohio, 1964.*

[20] W. Yang, R.D. Vispute, S. Choopun, R.P. Sharma, and T. Venkatesan, *Appl. Phys. Lett.*, 78, 2787 (2001).

[21] I. Takeuchi, W. Yang, K.S. Chang, M.A. Aronova, and T. Venkatesan, *J. Appl. Phys.*, 94, 7336 (2003).

[22] L.K. Wang, Z.G. Ju, C.X. Shan, D.Z. Shen, B.X. Zhao, Z.Z. Zhang, B.H. Li and J.Y. Zhang, *Solid State Commun.*, 149, 2021 (2009).

## Chapter 4

### Bandgap engineering of MgZnO films

#### 4.1 Introduction

Ternary semiconducting crystals are interesting because it is possible to smoothly change many important physical properties by varying their composition.<sup>1-4</sup> In particular, the MgZnO alloy system covers a wide ultraviolet (UV) spectral range between the direct bandgaps of ~3.37 eV for ZnO and ~7.8 eV for MgO at room temperature, and is very attractive for short-wavelength optical applications such as UV detectors and UV light emitters.<sup>5,6</sup> MgZnO alloys with different bandgap energies can be used to form ZnO/MgZnO or MgZnO/MgO multilayer quantum wells (QWs) heterostructure in UV light emitting diodes and laser diodes.<sup>7,8</sup> Therefore, in order to calculate the band alignment for designing and engineering a device, it is important to investigate the fundamental bandgap of MgZnO epitaxial films in all Mg content range. Moreover, the determination of bandgap bowing parameter which characterizes the nonlinear dependence of the fundamental bandgap on the alloy composition is also needed for the design of optoelectronic devices.<sup>9</sup>

In recent years, a large number of researches on the relationship between the Mg content and the bandgap energy were reported.<sup>10-13</sup> Ohtomo *et al.*<sup>10</sup> firstly prepared the MgZnO films with the bandgap energy from 3.3 to 4.0 eV corresponding to Mg content in the range of 0-0.33. Choopun *et al.*<sup>11</sup> reported the cubic MgZnO films with the Mg content from 0.5 to 0.7 have bandgap from 4.0 to 6.0 eV. Thapa *et al.*<sup>3</sup> grew

the MgZnO films with bandgap energy varying from 3.3 to 6.0 eV in the Mg content range of 0-0.78. However, there is no experimental data on MgZnO films which has the bandgap higher than 6.0 eV up to now. As described in Chapter 3, single phase MgZnO films without phase separation in all Mg content range were prepared by PLD.<sup>12</sup> The largest bandgap of Mg<sub>0.69</sub>Zn<sub>0.31</sub>O film was measured as 6.1 eV by transmittance spectra.<sup>12</sup> However, the wavelength range of the spectrometer for this method is commonly higher than 200 nm, which restrict the measurements for material with bandgap higher than 6.2 eV. The bandgap of MgZnO film with the Mg content above 0.70 can't be evaluated and bandgap bowing parameter can't be determined due to incomplete the relationship between the bandgap energy and the Mg content. Therefore, more valid method of testing the bandgap energy is highly required.

It is known that X-ray photoelectron spectroscopy (XPS) can be used to analyze the inelastic collisions in photoexcitation and photoemission of electrons from the material.<sup>14</sup> The inelastic collisions mainly include a fast-moving charged particle in the bulk material or an electron escaping from material surface can lose energy to excite another electron from the valence band into the conduction band.<sup>15</sup> The fundamental lower limit of inelastic loss is equal to the bandgap energy. Therefore, the onset of the inelastic energy loss spectra corresponds directly to the bandgap energy.<sup>16</sup> Based on this method, Ragesh *et al.*<sup>17</sup> demonstrated ZrO<sub>2</sub> had a bandgap of 6.4 eV. Their reports indicate the bandgap of semiconductors can be obtained by XPS. In this work, we report the dependence of the energy bandgap on Mg content in all

Mg content range by analyzing the O 1s energy loss spectra obtained from XPS. The bowing parameter is calculated by the relationship between the bandgap energy and the Mg content.

## 4.2 Experiment

A series of MgZnO films were deposited by PLD using a KrF laser source ( $\lambda = 248$  nm) on (0001) sapphire substrates. The MgZnO bulks with different Mg content were used as targets. The oxygen pressure during the growth was maintained at  $1 \times 10^{-1}$  Pa while the substrate temperatures were kept at  $500^\circ\text{C}$ . The deposition time was 40 min for all samples. XRD revealed that the (0002) diffraction peaks are observed from MgZnO films together with the peak of (0006) reflection from sapphire substrate in lower Mg content films, and the appearance of (111) and (222) diffraction peaks in higher Mg content films is a sign of single cubic phase.<sup>12</sup> The atomic force microscope results show the maximum roughness of the MgZnO is below 4 nm, indicating smooth surface. The XPS measurement was performed by Mg K $\alpha$  X-ray source. The binding energy of C 1s peak was used as a standard reference. Before XPS analysis the surface of the MgZnO films was etched by Ar<sup>+</sup> ion (3 keV) for 2 min.

### 4.3 Results and discussion

Figure 4.1 (a) shows a representative scan of the O 1s core level spectrum from the MgO film grown in this work. From figure 4.1 (a), the largest signal corresponds to the primary photoelectron peak caused by the O 1s core level electrons located at binding energy 532.2 eV. The bulk plasmon loss peak is observed at 554.9 eV, corresponding to the bulk plasmon energy 22.7 eV. Moreover, a small overlapping peak observed at 523.4 eV is attributed to X-ray satellite peaks because of  $K\alpha$  transitions from the non-monochromatic Mg X-ray source. In order to verify this method for determining the bandgap energy of MgZnO films by XPS, a XPS scan of the O 1s core level spectrum from the MgO film has been obtained as shown in figure 4.1 (b). A linear fit is made to the measured loss spectra curve near the approximate location of onset of inelastic loss.<sup>15</sup> And then, the background line which is parallel to horizontal axis can be determined by subtracting the background fitting. The initial energy of inelastic loss is obtained by extrapolating the linear-fit line and calculating its intersection with the “zero” level line. The bandgap energy of MgO film is equal to the difference between the O 1s core level peak energy and the initial energy of inelastic losses. Thus, the bandgap energy is calculated to be 7.3 eV which has good agreement with the previous values for MgO<sup>3,18</sup>, indicating that the XPS is a valid way to determine the bandgap of MgZnO films.

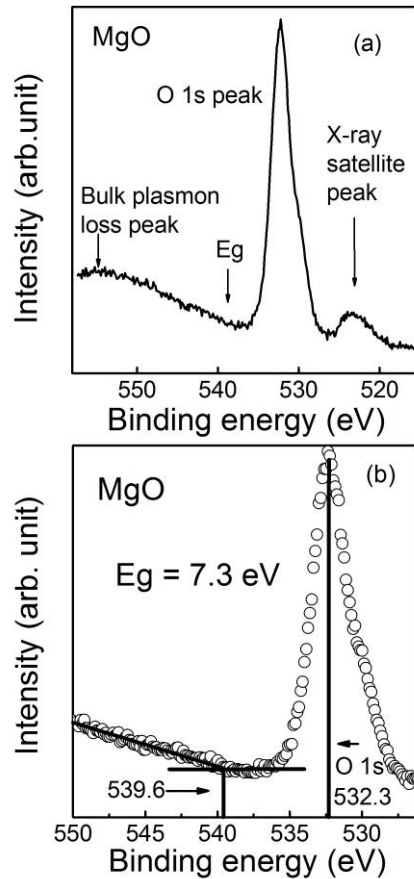


Figure 4.1 Measurement of the bandgap of MgO film by onset of electron energy loss spectra. (a), XPS scan of the O 1s core level for MgO film (b).

Figure 4.2 (a) and (b) show the XPS spectra of Mg 2p and Zn 2p core levels for MgZnO films grown with different Mg content  $x_t$  in the target. As shown in figure 4.2(a), the Mg 2p peaks of MgZnO films with different Mg content  $x_t$  exhibit a nearly Gaussian line shape, indicating a single chemical state of Mg element. The Mg 2p peaks are located at 50.2 eV which is attributed to Mg-O bonding and the intensity of Mg 2p peak increases with the increase of Mg content  $x_t$ . The Zn 2p core-level of ZnO film ( $x_t = 0$ ) has two peaks at about 1021.9 and 1044.2 eV assigned to Zn 2p<sub>3/2</sub> and Zn 2p<sub>1/2</sub>, respectively. The intensity of Zn 2p peaks decreases with the increase of Mg

content  $x_t$ .

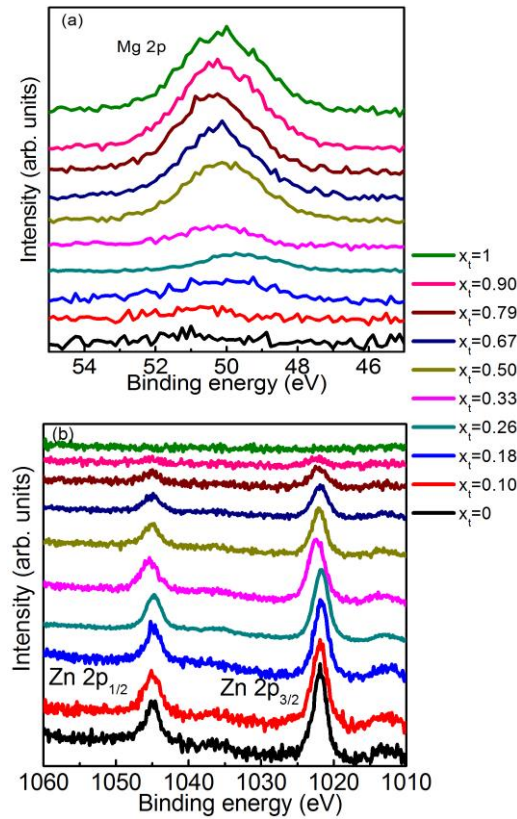


Figure 4.2 Mg 2p (a) and Zn 2p (b) core level spectra of MgZnO films with different Mg contents in targets  $x_t$ .

The Mg contents in the MgZnO films are determined from the XPS peak area after using an atomic sensitivity factor, which convert relative peak areas to relative numbers of atoms in the detected volume.<sup>20</sup> The Mg contents in the MgZnO films obtained from the XPS spectra is shown in figure 4.3 as a function of Mg content in the target  $x_t$ . The element content in the film is larger than that in the target. This phenomenon can be explained by the difference of vapor pressure between Mg and Zn species. Zn species have a higher vapor pressure and can be desorbed more easily

than that of Mg species at same growth temperature which results in the more Mg enriched films at high growth temperatures. These content results from the XPS spectra are agreed with those from Energy Dispersive Spectrometer (EDS) which have been reported in the Chapter 3. It is well known that XPS is primarily a surface technique. The analyzed depth is about 2 nm and the area of analysis is an ellipse on the surface.<sup>21</sup> Compared with XPS, the analysis depth of EDS is much deeper and the analyzed volume is shaped like a Florence flask with the narrow neck shortened due to subsurface scattering.<sup>21</sup> Therefore, the same Mg content results from two methods indicate the samples measured in this work have very uniform composition distribution in the MgZnO films.

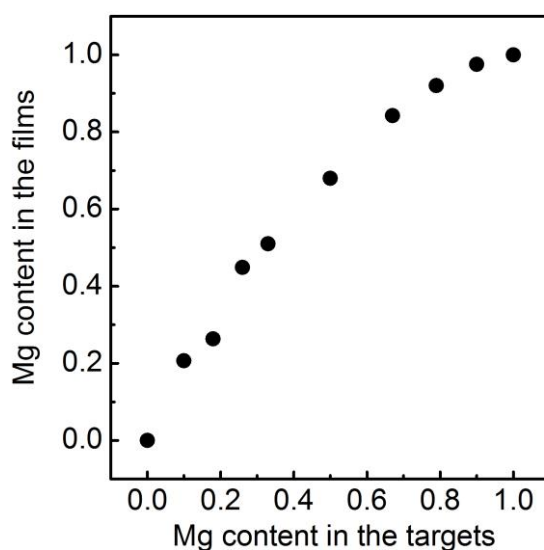


Figure 4.3 The Mg content in the films obtained by XPS.

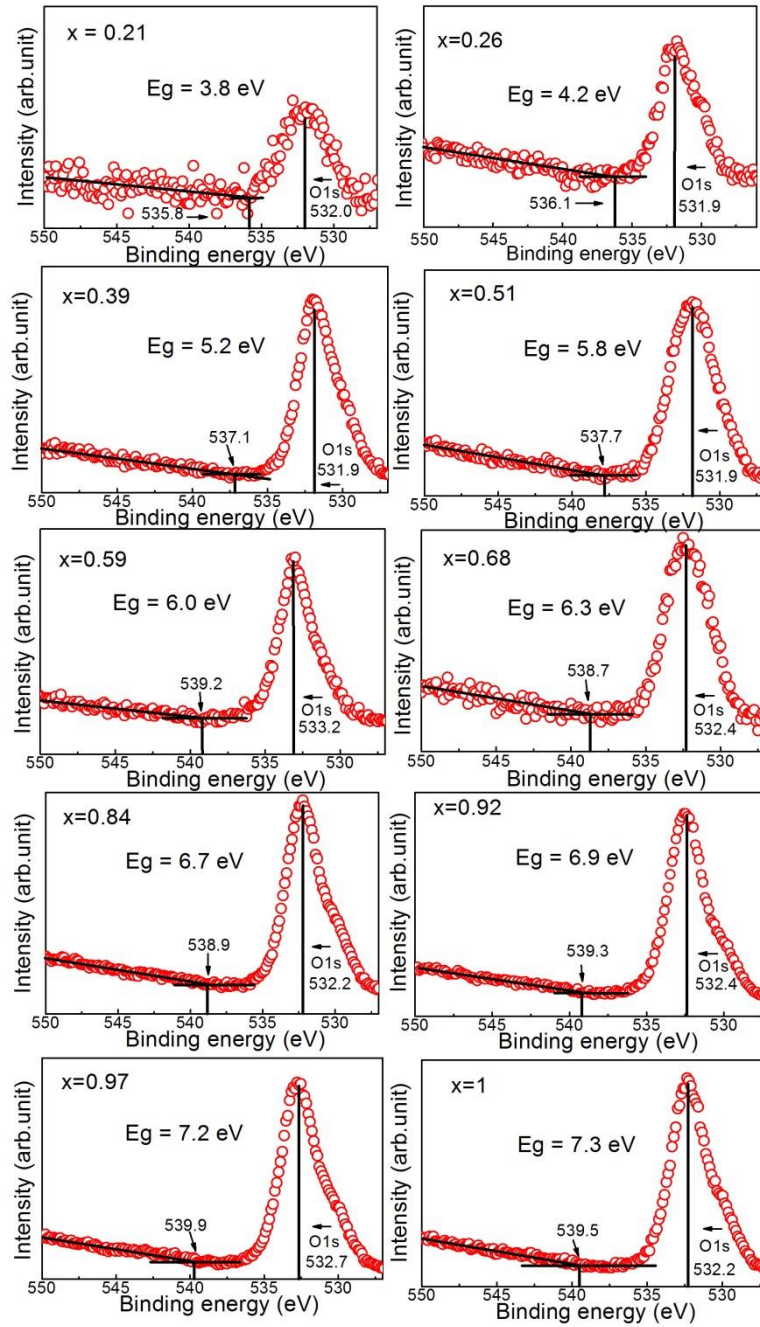


Figure 4.4 The O 1s peak and inelastic scattering loss for MgZnO films in all Mg content.

Figure 4.4 shows the O 1s core level peaks of MgZnO films with various Mg contents in the MgZnO films. The bandgap energies of MgZnO films with Mg content of 0.21, 0.26, 0.39, 0.51 and 0.59 are determined to be 3.8, 4.2, 5.2, 5.8 and 6.0 eV,

respectively. These values show good agreement with those measured from transmittance spectra in Chapter 3 as shown in figure 4.5. The O 1s core level peaks of MgZnO films in the Mg content range from 0.68 to 1 are also shown in figure 4.4 corresponding to the bandgaps from 6.3 to 7.3 eV which have been plotted in figure 4.5 together with the experimental data from transmittance spectra.

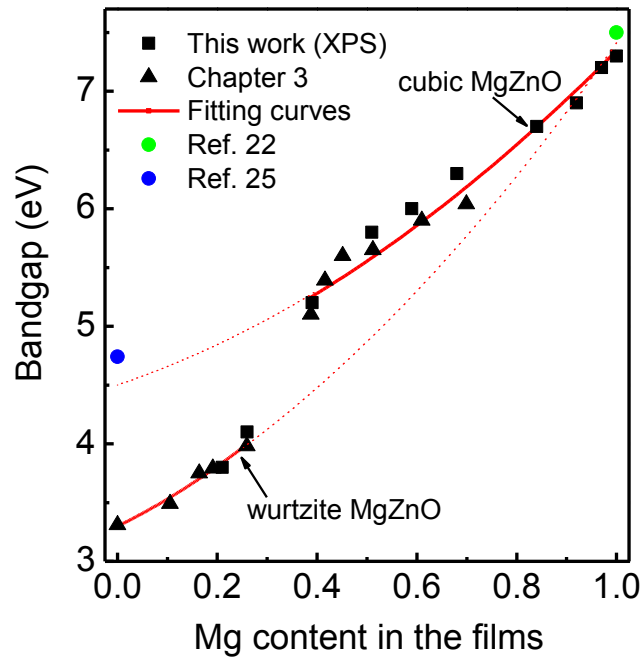


Figure 4.5 Dependence of the bandgap of MgZnO films on Mg content  $x$  in the films.

In order to describe the compositional dependence of bandgap of the MgZnO alloys, we used the standard bowing equation,

$$E_g(\text{Mg}_x\text{Zn}_{1-x}\text{O}) = (1-x) \cdot E_g(\text{ZnO}) + x \cdot E_g(\text{MgO}) - b \cdot x \cdot (1-x) \quad (1)$$

Here,  $E_g(\text{ZnO})$ ,  $E_g(\text{MgO})$  and  $E_g(\text{Mg}_x\text{Zn}_{1-x}\text{O})$  are the energy bandgaps of ZnO, MgO and MgZnO films.  $b$  is a band bowing parameter which characterizes the degree of deviation from linearity. As shown in figure 4.5, the relationship between the bandgap energy and the Mg content in all Mg content range can be fitted by quadratic function

as two red solid lines corresponding to different crystal structures.

According to figure 4.5, the lower red solid line fitted to the bandgaps of wurtzite MgZnO films shows a quadratic form:

$$E_g(\text{wurtzite Mg}_x\text{Zn}_{1-x}\text{O}) = 3.31 \cdot (1 - x) + 7.41 \cdot x - 2.01 \cdot x(1 - x) \quad (2)$$

Based on Eq. (2), the bandgap of wurtzite MgO is calculated to be 7.41 eV which agrees well with the value of 7.5 eV predicted by Jang *et al.*<sup>22</sup> using *ab initio* calculations as shown in figure 4.5. According to the analysis of fitting curve, the obtained bowing parameter  $b$  of  $(2.01 \pm 0.02)$  eV is very close to that of 2.84 eV from the calculations of Schleife *et al.*<sup>18</sup> The band bowing occurs due to volume deformation, spontaneous polarization, structural relaxation and alloy mismatch. In wurtzite MgZnO alloys, the bandgap bowing is mainly attributed to spontaneous polarization. Because the wurtzite MgZnO alloy is a polar material exhibiting a spontaneous polarization along the  $c$ -axis, increasing with Mg content. The internal field caused by piezoelectric and spontaneous polarizations, which presents along the growth axis of the system, makes the bandgap shift.<sup>23</sup> Similar phenomenon was also found in AlGaN alloys.<sup>24</sup>

For the cubic MgZnO films, the dependence of the energy bandgap on Mg content can be fitted as

$$E_g(\text{cubic Mg}_x\text{Zn}_{1-x}\text{O}) = 4.44 \cdot (1-x) + 7.30 \cdot x - 1.48 \cdot x(1-x) \quad (3)$$

The bandgap energy of cubic ZnO film is determined to be 4.44 eV from Eq. (3). This value has reasonable agreement with that (4.7 eV) calculated by Ni *et al.* using quasiparticle methods.<sup>25</sup> The value for bowing parameter  $b$  of  $(1.48 \pm 0.07)$  eV is

obtained. It is less than the value of 6.14 eV calculated by Schleife *et al.* using *ab initio* calculations, which is attributed to the lower bandgap of 2.88 eV for cubic ZnO used in their calculations.<sup>18</sup>

#### **4.4 Conclusion**

In this chapter, the bandgap bowing parameters for wurtzite and cubic MgZnO alloys in all Mg content range are reported. The Mg contents in the MgZnO films were accurately determined using EDS and XPS. The measurement of bandgap energies by examining the onset of inelastic energy loss in core-level atomic spectra from XPS was proved to be valid for determining the bandgap of MgZnO films. The dependence of the energy bandgap on Mg content was found to deviate downwards from linearity. Fitting of the bandgap energies resulted in two bowing parameters of 2.01 and 1.48 eV corresponding to wurtzite and cubic MgZnO films, respectively. These data are crucial for designing ZnO/MgZnO or MgZnO/MgO quantum wells for enhancing performance in deep UV light emitting diodes and laser diodes

## References

- [1] Y. N. Hou, Z. X. Mei, H. L. Liang, D. Q. Ye, C. Z. Gu, and X. L. Du, *Appl. Phys. Lett.*, 102, 153510 (2013).
- [2] W. Z. Liu, H. Y. Xu, J. G. Ma, C. Y. Liu, Y. X. Liu, and Y. C. Liu, *Appl. Phys. Lett.*, 100, 203101 (2012).
- [3] D. Thapa, J. Huso, H. Che, M. Huso, J. L. Morrison, D. Gutierrez, M. G. Norton, and L. Bergman, *Appl. Phys. Lett.*, 102, 191902 (2013).
- [4] L. K. Wang, Z. G. Ju, J. Y. Zhang, J. Zheng, D. Z. Shen, B. Yao, D. X. Zhao, Z. Z. Zhang, B. H. Li, and C. X. Shan, *Appl. Phys. Lett.*, 95, 131113 (2009).
- [5] M. M. Morshed, M. Suja, Z. Zuo, and J. L. Liu, *Appl. Phys. Lett.*, 105, 211107 (2014).
- [6] J. W. Kang, Y. S. Choi, B. H. Kim, C. G. Kang, B. H. Lee, C. W. Tu, and S. J. Park, *Appl. Phys. Lett.*, 104, 051120 (2014).
- [7] H. Y. Chen, K. W. Liu, M. M. Jiang, Z. Z. Zhang, X. H. Xie, D. K. Wang, L. Liu, B. H. Li, D. X. Zhao, C. X. Shan, and D. Z. Shen, *Appl. Phys. Lett.*, 104, 091119 (2014).
- [8] J. S. Wrench, I. F. Brunell, P. R. Chalker, J. D. Jin, A. Shaw, I. Z. Mitrovic, and S. Hall, *Appl. Phys. Lett.*, 105, 202109 (2014).
- [9] E. Sakalauskas, O. Tuna, A. Kraus, H. Bremers, U. Rossow, C. Giesen, M. Heuken, A. Hangleiter, G. Gobsch, and Goldhahn, *Phys Status Solidi B*, 249, 485 (2012).
- [10] A. Ohtomo, M. Kawasaki, T. Koida, K. Masubuchi, H. Koinuma, Y. Sakurai, Y. Yoshida, T. Yasuda, and Y. Segawa, *Appl. Phys. Lett.*, 72, 2466 (1998)

- [11] S. Choopun, R. D. Vispute, W. Yang, R. P. Sharma, T. Venkatesan, and H. Shen, *Appl. Phys. Lett.*, 80, 1529 (2002).
- [12] X. Wang, K. Saito, T. Tanaka, M. Nishio, and Q. X. Guo. *J. Alloys Compd.*, 627, 383 (2015).
- [13] J. Tauc, *Mater. Res. Bull.*, 3, 37 (1968).
- [14] F. B. Zhang, K. Saito, T. Tanaka, M. Nishio, M. Arita, and Q. X. Guo, *Appl. Phys. Lett.*, 105, 162107 (2014).
- [15] M. T. Nichols, W. Li, D. Pei, G. A. Antonelli, Q. Lin, S. Banna, Y. Nishi, and J. L. Shohet, *J. Appl. Phys.*, 115, 094105 (2014).
- [16] F. G. Bell and L. Ley, *Phys. Rev. B*, 37, 8383 (1988).
- [17] R. Puthenkovilakam and J. P. Chang, *Appl. Phys. Lett.*, 84, 1353 (2004).
- [18] A. Schleife, C. Rodl, J. Furthmuller and F. Bechstedt, *New J. Phys.*, 13, 085012 (2011).
- [19] H. Y. Yu, M. F. Li, B. J. Cho, C. C. Yeo, M. S. Joo, D. L. Kwong, J. S. Pan, C. H. Ang, J. Z. Zheng, and S. Ramanathan, *Appl. Phys. Lett.*, 81, 376 (2002).
- [20] C. D. Wagner, *J. Electron. Spectrosc. Relat. Phenom.*, 32, 99 (1983).
- [21] P. Sanguino, R. Schwarz, M. Wilhelm, M. Kunst, and O. Teodoro, *Vacuum*, 81, 1524 (2007).
- [22] S.-H. Jang and S. F. Chichibu, *J. Appl. Phys.*, 112, 073503 (2012).
- [23] A. Ashrafi, and Y. Segawa, *J. Appl. Phys.*, 104, 123528 (2008).
- [24] F. Bernardini and V. Fiorentini, *Phys. Rev. B*, 64, 085207 (2001).
- [25] H. Q. Ni, Y. F. Lu, and Z. M. Ren, *J. Appl. Phys.*, 91, 1339 (2002).

## Chapter 5

### Raman scattering in $(\text{Al}_x\text{Ga}_{1-x})_2\text{O}_3$ films

#### 5.1 Substrate temperature effect

Owing to its direct wide-bandgap (4.9 eV) at room temperature,  $\text{Ga}_2\text{O}_3$  has attracted much attention as the most promising materials for fabricating deep ultraviolet (DUV) optoelectronic devices such as light detectors and emitters.<sup>1-4</sup> A crucial step for designing optoelectronic devices is to develop quantum well structures according to bandgap engineering.<sup>5,6</sup> The doping into wide bandgap binary semiconductors like  $\text{Ga}_2\text{O}_3$  with selective elements provides an effective method to engineer the bandgap of alloys.<sup>7, 8</sup> Group III indium and aluminum are extensively used to tailor the bandgap of  $\text{Ga}_2\text{O}_3$ . Indium doping was studied by some researchers for narrowing the bandgap of  $\text{Ga}_2\text{O}_3$  and aluminum doping in  $\text{Ga}_2\text{O}_3$  was explored for enlarging the bandgap.  $\text{Al}_2\text{O}_3$  has a larger direct bandgap of 8.8 eV, and by alloying with  $\text{Al}_2\text{O}_3$ , the bandgap of  $\text{Ga}_2\text{O}_3$  can be modulated toward higher energy, and the luminescence of  $(\text{AlGa})_2\text{O}_3$  alloys is expected to cover a larger DUV region. Moreover, the experimental result indicates that the replacement of the proper amount of Ga by Al can't cause a significant change in lattice constant and crystal structure.<sup>9,10</sup> Therefore, the  $(\text{AlGa})_2\text{O}_3$  alloy is a promising material as the barrier layer in  $\text{Ga}_2\text{O}_3$ -based quantum well structures, which is the key elements in DUV optoelectronic devices.

Recently, we succeeded in preparing  $(\text{AlGa})_2\text{O}_3$  thin films on (0001) sapphire

substrates by pulsed laser deposition (PLD) and observed the bandgap of  $(\text{AlGa})_2\text{O}_3$  films increases continuously from about 5 to 7 eV with Al content covering the whole Al content range, paving the way for obtaining  $(\text{AlGa})_2\text{O}_3$  barrier layer of  $\text{Ga}_2\text{O}_3$ -based quantum well structure.<sup>11</sup> The  $(\text{AlGa})_2\text{O}_3$  film grown by using the 0.17 Al content target has a bandgap of around 5.5 eV which is sufficient for barrier layer in  $\text{Ga}_2\text{O}_3$ -based quantum well structure. It is well known that the crystal structure of the semiconductor thin film can be strongly influenced by substrate temperature.<sup>12, 13</sup> It has been reported that the epitaxial  $\text{Ga}_2\text{O}_3$  films grown at substrate temperature from 500 to 550 °C have a crystal structure different from that of  $\beta$ - $\text{Ga}_2\text{O}_3$  and when substrate temperature is above 600 °C, no film growth occurred due to evaporation of Ga atoms.<sup>14</sup> Therefore, in order to obtain optimized  $\text{Ga}_2\text{O}_3$ -based quantum well structure, systematically investigation about the influence of substrate temperature on the structure and properties of  $(\text{AlGa})_2\text{O}_3$  films with proper Al content is highly required. To the best of our knowledge, there is no related report up to now. In this Chapter, we have deposited  $(\text{AlGa})_2\text{O}_3$  films by using 0.17 Al content target at different substrate temperatures. The effects of substrate temperature on structure, surface morphology, and optical properties were systematically investigated, which will provide an experimental basis for realizing the  $\text{Ga}_2\text{O}_3$ -based quantum well.

$(\text{AlGa})_2\text{O}_3$  films were performed by PLD using a KrF laser source ( $\lambda=248$  nm) on (0001) sapphire substrates. The bulk with the Al content of 0.17 (mole ratio of Al/(Ga+Al)) was used as target. Before growth, the sapphire substrates were cleaned in organic solvents by in an ultrasonic cleaning system, and then chemically etched in a

hot  $\text{H}_3\text{PO}_4$ :  $\text{H}_2\text{SO}_4$  (1:3) solution. In the growth chamber, facing the substrate, the target was set. The pulsed laser with a frequency of 2 Hz was irradiated and the distance between target and substrate was about 30 mm. The laser energy was set 225 mJ. The oxygen pressure of the growth chamber was set at  $1 \times 10^{-1}$  Pa by introducing high purity oxygen gas (99.999%) while the substrate temperature was varied from 300 to 600 °C. The deposition time was 3 h for all the  $(\text{AlGa})_2\text{O}_3$  films.

After the growth, the thickness of  $(\text{AlGa})_2\text{O}_3$  films was measured by using a surface step profile analyzer. The surface morphology and root mean square (RMS) roughness of the  $(\text{AlGa})_2\text{O}_3$  films were studied by AFM. The optical transmission spectra were measured with a spectrophotometer. The crystal structure and crystal quality of the  $(\text{AlGa})_2\text{O}_3$  films were evaluated by using x-ray diffraction (XRD) and x-ray rocking curve (XRC). Raman measurements were performed on a micro-Raman system with a classic charge-coupled device detector.

The growth rate of  $(\text{AlGa})_2\text{O}_3$  films grown at different substrate temperatures is shown in figure 5.1. The growth rate decreases with increasing the substrate temperature from 300 to 400 °C and then is about 1.3 nm/min in the substrate temperature range from 400 to 500 °C. When the substrate temperature is higher than 500 °C, the growth rate decreases rapidly, which can be attributed to reevaporation of the absorbed species on the surface of the substrate.<sup>13</sup>

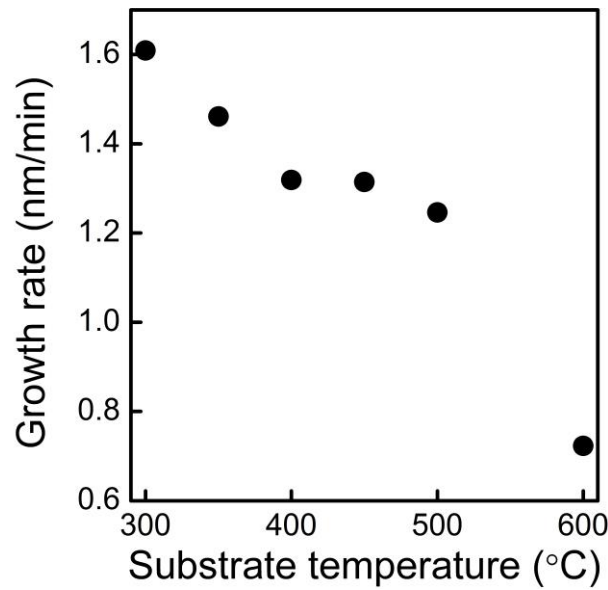


Figure 5.1 Dependence of the growth rate of  $(\text{AlGa})_2\text{O}_3$  films on the substrate temperatures.

Figure 5.2 shows AFM images of the  $(\text{AlGa})_2\text{O}_3$  films grown at different substrate temperatures. It is clear that the surface morphology changes with the increase of substrate temperature. The grain-like morphology can be observed in the  $(\text{AlGa})_2\text{O}_3$  films grown at the substrate temperature higher than  $350\text{ }^\circ\text{C}$ , while the  $(\text{AlGa})_2\text{O}_3$  films grown at  $300\text{ }^\circ\text{C}$  exhibits a smooth surface morphology. It is worth noting that the  $(\text{AlGa})_2\text{O}_3$  films grown at  $400$  and  $450\text{ }^\circ\text{C}$  have the more obvious grain-like surface morphology. The RMS surface roughness of  $(\text{AlGa})_2\text{O}_3$  films is shown in figure 5.3 as a function of the substrate temperature. The surface roughness of  $(\text{AlGa})_2\text{O}_3$  films initially increases with increasing the substrate temperature up to  $400\text{ }^\circ\text{C}$  and then gradually decreases with a further increase in the substrate temperature.

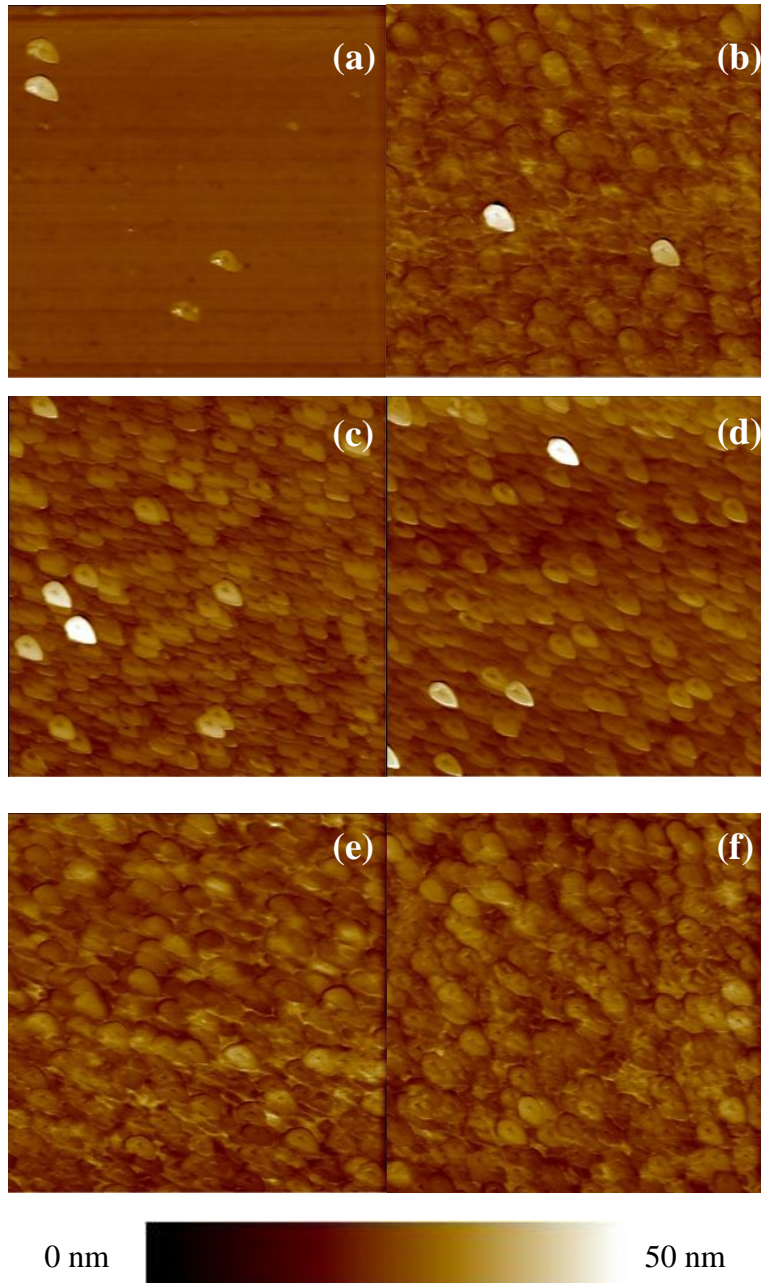


Figure 5.2 AFM morphologies of  $(\text{AlGa})_2\text{O}_3$  films grown at different substrate temperatures of (a) 300 °C, (b) 350 °C, (c) 400 °C, (d) 450 °C, (e) 500 °C, and (f) 600 °C, respectively. The scan area is  $4 \times 4 \mu\text{m}^2$ .

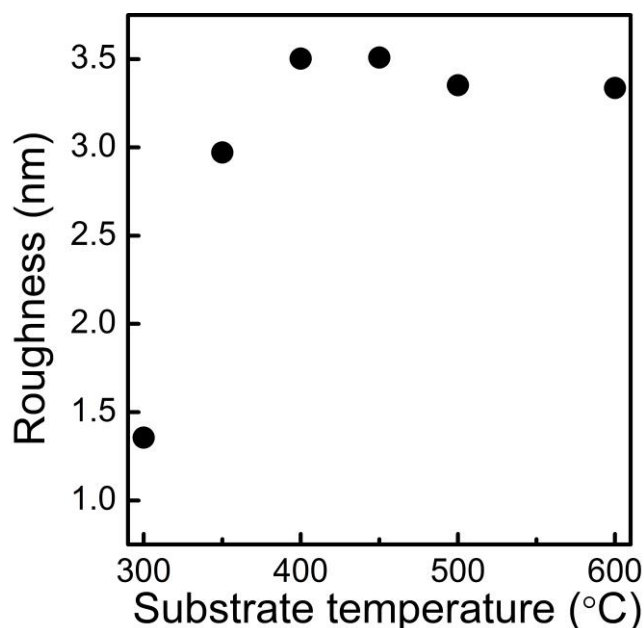


Figure 5.3 Dependence of the surface roughness of  $(\text{AlGa})_2\text{O}_3$  films on the substrate temperatures.

The transmittance spectra of  $(\text{AlGa})_2\text{O}_3$  films with different substrate temperatures are shown in Figure 5.4, which exhibit above 75% transmittance in the wavelength range from 300 to 800 nm. The  $(\text{AlGa})_2\text{O}_3$  films show slight variation in transparency due to surface roughness and scattering of incident light. It is well known that for the film with direct bandgap, the absorption follows the equation (1) (see page 49).

The plot of  $(\alpha h\nu)^2$  as a function of photon energy was shown in figure 5.5. Compared with the  $(\text{AlGa})_2\text{O}_3$  film grown at substrate temperature of 300 °C, the  $(\text{AlGa})_2\text{O}_3$  film grown at substrate temperature of 400 °C has a larger optical bandgap, which can be ascribed to the increase of Al content with increasing the substrate temperature. When the substrate temperature reaches to 450 °C, the decrease in optical bandgap can be associated with a decrease in transition tail width. The bandgap increases with a further increase in the substrate temperature, which is

caused by the increase of Al content due to difference of vapor pressure between Ga and Al species at higher substrate temperature. The similar phenomenon has been confirmed in our previous work about MgZnO films.<sup>16</sup>

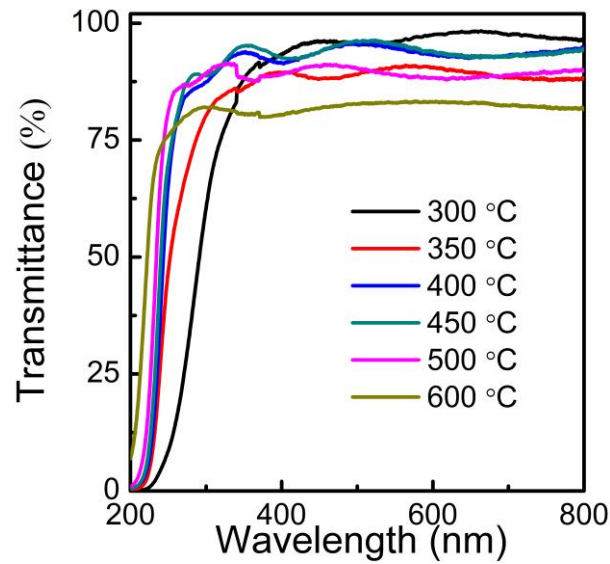


Figure 5.4 Transmittance spectra of  $(\text{AlGa})_2\text{O}_3$  films grown at different substrate temperatures.

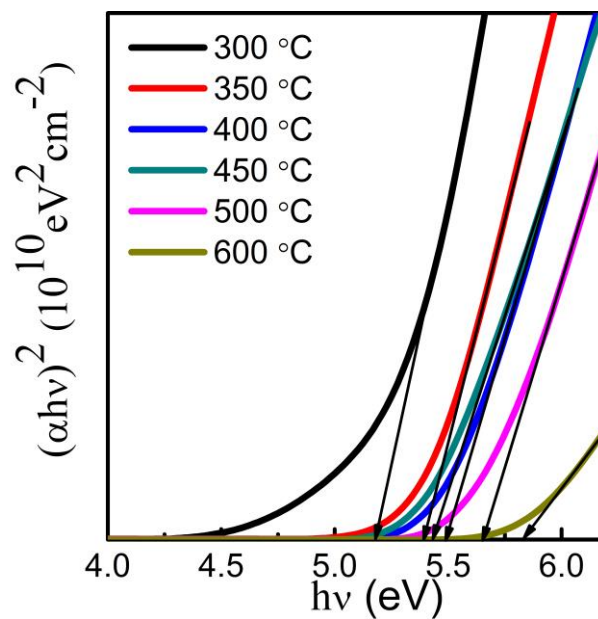


Figure 5.5  $(\alpha h\nu)^2$  vs.  $h\nu$  plot of  $(\text{AlGa})_2\text{O}_3$  films grown at different substrate temperatures.

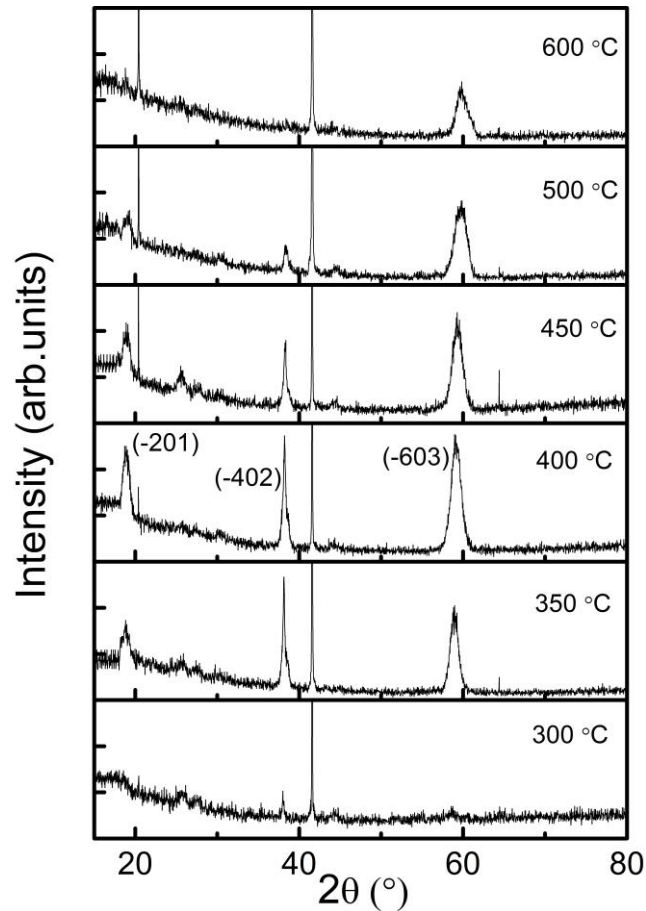


Figure 5.6 XRD patterns of  $(\text{AlGa})_2\text{O}_3$  films grown at different substrate temperatures.

In order to investigate the effect of the substrate temperature on crystal structure, we measured the XRD patterns of the  $(\text{AlGa})_2\text{O}_3$  films as shown in figure 5.6. When the substrate temperature is 300 °C, there is almost no peak except the (0006) peak from sapphire substrate. The  $(\text{AlGa})_2\text{O}_3$  films grown in the substrate temperature range from 350 to 500 °C exhibit three peaks at 18.97°, 38.27°, and 59.18° which are ascribed to the patterns of monoclinic  $\beta$ - $(\text{AlGa})_2\text{O}_3$  can be assigned as the (-201), (-402), and (-603) faces, respectively.<sup>11</sup> None of the (111), (001), and (-101) peaks of

$\beta$ -(AlGa)<sub>2</sub>O<sub>3</sub>, which have a stronger diffraction peaks than that of (-201), can be detected within the searched angle ( $15^\circ \leq 2\theta \leq 80^\circ$ ). It indicates that (-201) oriented  $\beta$ -(AlGa)<sub>2</sub>O<sub>3</sub> can be epitaxially prepared on (0001) sapphire substrates. It is worth noting that the  $2\theta$  angle of (-603) peak increases with the increase of the substrate temperature due to the decrease of lattice distance induced by the increase of Al content.

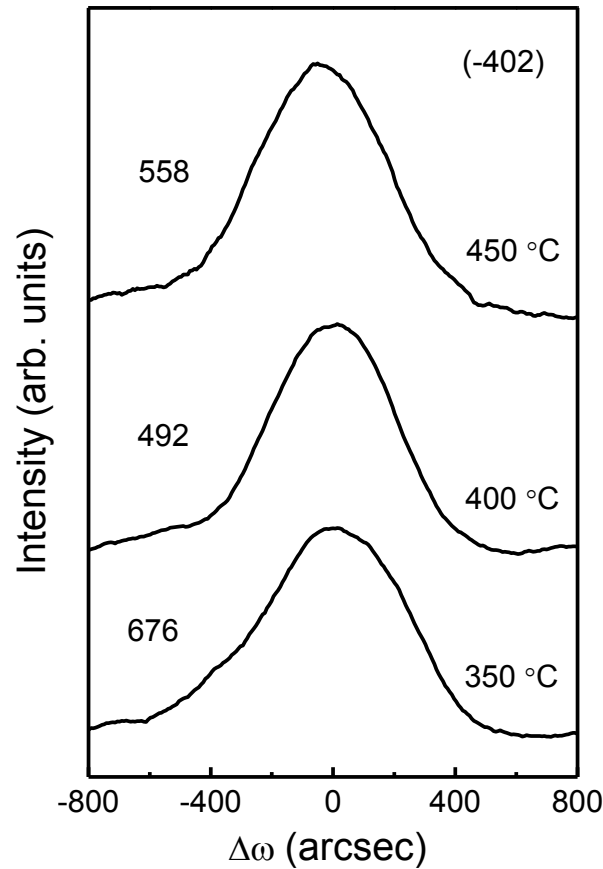


Figure 5.7 XRCs for (-402) reflection from (AlGa)<sub>2</sub>O<sub>3</sub> films grown at different substrate temperatures.

It is well known that the  $\theta$ - $2\theta$ -mode measurement can't precisely detect the quality of the epilayers, because the variation in the lattice spacing mainly broadens the full-width at half maximum (FWHM) in this mode. Therefore, we measured the

diffraction profiles of the (-402) reflection for  $(\text{AlGa})_2\text{O}_3$  films grown at the substrate temperature of 350, 400, and 450 °C in the  $\omega$  mode in order to investigate the crystal quality of the films. Figure 5.7 presents the XRCs from (-402) reflection for  $(\text{AlGa})_2\text{O}_3$  films grown at the substrate temperature of 350, 400, and 450 °C. The FWHM value decreases with the substrate temperature up to 400 °C and then increases. The  $(\text{AlGa})_2\text{O}_3$  film grown at the substrate temperature of 400 °C has the smallest full-width at half maximum of 492 arcsec. The result indicates that the substrate temperature has an effect on the crystal quality of  $(\text{AlGa})_2\text{O}_3$  films and the  $(\text{AlGa})_2\text{O}_3$  film grown at the substrate temperature of 400 °C has the good crystal quality.

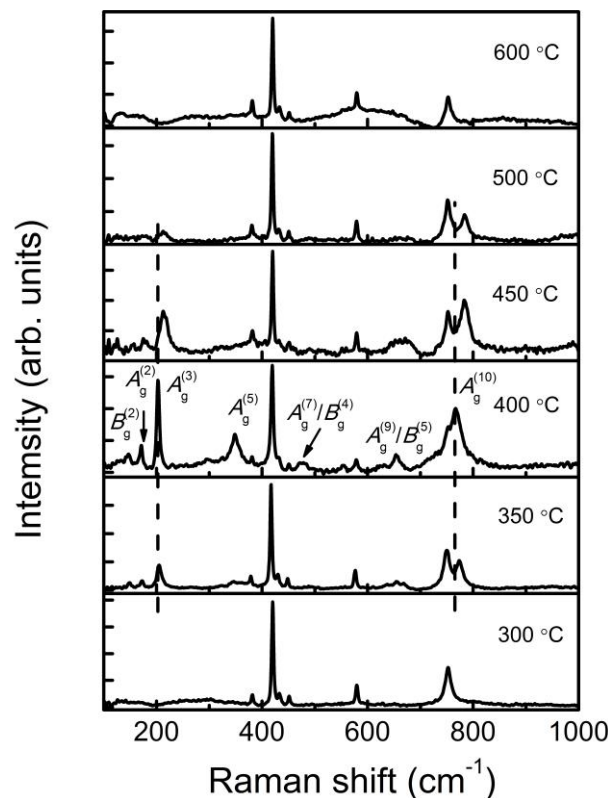


Figure 5.8 Raman spectra of  $(\text{AlGa})_2\text{O}_3$  films grown at different substrate temperatures.

Raman scattering is considered to be a powerful nondestructive and sensitive technique to study the crystal quality in the alloy materials because the extended defects can broaden the Raman peaks. Figure 5.8 shows the Raman spectra obtained at room temperature for (AlGa)<sub>2</sub>O<sub>3</sub> films grown at different substrate temperatures. Raman scattering was recorded in the back-scattering geometry of the z (x, -)  $\bar{z}$  configuration<sup>17</sup> using an Ar laser at 488 nm. When the substrate temperature is 300 °C, no peak from  $\beta$ -(AlGa)<sub>2</sub>O<sub>3</sub> can be observed in the Raman shift range from 100 to 1000 cm<sup>-1</sup> except the peaks at 418, 580, and 754 cm<sup>-1</sup> caused by sapphire substrate. For (AlGa)<sub>2</sub>O<sub>3</sub> film grown at the substrate temperature from 350 to 500 °C, nine Raman mode peaks can be observed. It is well known that the monoclinic Ga<sub>2</sub>O<sub>3</sub> belongs to the space group C2/m/C<sub>2h</sub><sup>3</sup>. The phonon modes of  $\beta$ -Ga<sub>2</sub>O<sub>3</sub> can be classified into three groups: low-frequency libration and translation (below 200 cm<sup>-1</sup>) of tetrahedra-octahedra chains, mid-frequency deformation of Ga<sub>2</sub>O<sub>6</sub> octahedra (~310-480 cm<sup>-1</sup>), and high-frequency stretching and bending of GaO<sub>4</sub> tetrahedra (~500-770 cm<sup>-1</sup>).<sup>18</sup> Therefore, these peaks can be assigned to B<sub>g</sub><sup>(2)</sup>, A<sub>g</sub><sup>(2)</sup>, A<sub>g</sub><sup>(3)</sup>, A<sub>g</sub><sup>(5)</sup>, A<sub>g</sub><sup>(7)</sup>/B<sub>g</sub><sup>(4)</sup>, A<sub>g</sub><sup>(9)</sup>/B<sub>g</sub><sup>(5)</sup>, and A<sub>g</sub><sup>(10)</sup> phonon modes, respectively. The peak of A<sub>g</sub><sup>(7)</sup>/B<sub>g</sub><sup>(4)</sup> phonon modes as well as A<sub>g</sub><sup>(9)</sup>/B<sub>g</sub><sup>(5)</sup> can't be unambiguously assigned to one of the mode peaks A<sub>g</sub><sup>(7)</sup> or B<sub>g</sub><sup>(4)</sup> because Raman shifts of A<sub>g</sub><sup>(7)</sup> (A<sub>g</sub><sup>(9)</sup>) modes is very close to that of B<sub>g</sub><sup>(4)</sup> (B<sub>g</sub><sup>(5)</sup>) modes. Moreover, compared with the Raman shifts of Ga<sub>2</sub>O<sub>3</sub>, all the phonon modes of (AlGa)<sub>2</sub>O<sub>3</sub> films have a shift toward the direction of large Raman shift, which can be attributed to the cooperation of Al atom. In order to investigate the effect of growth temperature, the Raman shifts and linewidth of A<sub>g</sub><sup>(3)</sup>

and  $A_g^{(10)}$  phonon modes are analyzed as shown in figure 5.9(a) and (b), respectively, because these two phonon modes have the higher intensity. As shown in figure 5.9(a), the  $A_g^{(3)}$  phonon modes of  $(AlGa)_2O_3$  film grown at the substrate temperature from 350, 400, 450, and 500 °C have Raman shifts of 204.23, 202.87, 211.05, and 212.77  $cm^{-1}$ , respectively. In order to obtain more accurate information of the linewidth broadening, a curve fitting program by using the Lorentz equation was employed to fit the experimental Raman spectra, which has been used in our previously work.<sup>18</sup> The linewidth broadening of the  $A_g^{(3)}$  phonon modes with the substrate temperature are shown in figure 5.9(a). The smallest linewidth broadening of around 6.83  $cm^{-1}$  can be obtained. The similar results can also be found for the  $A_g^{(10)}$  phonon modes of  $(AlGa)_2O_3$  films as shown in figure 5.9(b).

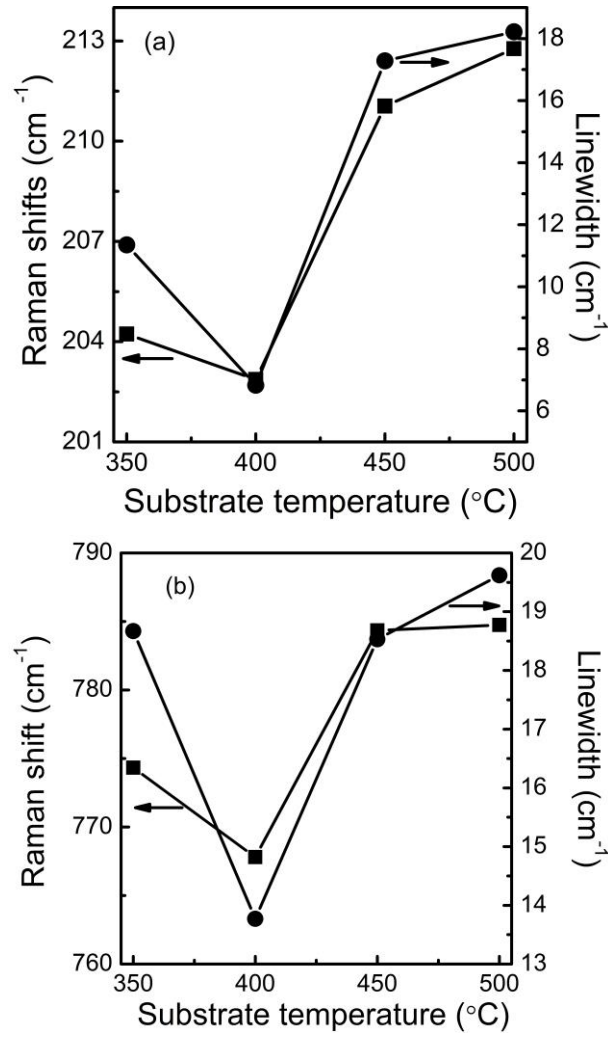


Figure 5.9 Raman shift and linewidth of (a)  $A_g^{(3)}$  and (b)  $A_g^{(10)}$  phonon modes in  $(AlGa)_2O_3$  films grown at different substrate temperatures.

The difference of the Raman shifts is due to the lattice defect and structural disorder induced by different substrate temperatures. The lattice defect and structural disorder bring on an increase of phonon density of states which leads to the enhancement of the probability of inelastic scattering between the phonons and substitutional atoms.<sup>19</sup> As a result, the different Raman shift can be observed with varying substrate temperatures. The linewidth ( $\Gamma$ ) is related to the lifetime ( $\tau$ ) of the involved phonon, which can be expressed by the simple relation  $\tau = 1/(\pi c\Gamma)$ , where  $c$

is velocity of light. The smaller linewidth results in a larger decay lifetime, and so the more phonon free paths exist.<sup>20</sup> It reflects the higher crystal quality of the (AlGa)<sub>2</sub>O<sub>3</sub> film as observed by XRC measurements as shown in figure 5.7. It is obvious from the above experimental results that the substrate temperature has a dramatic effect of the growth of (AlGa)<sub>2</sub>O<sub>3</sub> films and the (AlGa)<sub>2</sub>O<sub>3</sub> film with the good crystal quality can be obtained at the substrate temperature of 400 °C which is much lower than the growth temperature by other methods. In general, high growth temperature is better for crystal growth. However, for PLD process, high growth temperature induces the reevaporation of the adsorbed species on the surface of the substrate. The evaporation of Ga atoms from the growing film became dominant and no film growth occurred at high growth temperature in the work of Kosuke *et al.*<sup>14</sup>. The large lattice mismatch between sapphire and epitaxial film generates a high density of threading dislocations, which leads to non-radiative recombination centers and thereby limits the emission efficiency.<sup>21</sup> One way to suppress threading dislocations is known to be reduction of the growth temperature.<sup>22</sup> Moreover, the determination of the optimal growth temperature for (AlGa)<sub>2</sub>O<sub>3</sub> film will provide an experimental basis for realizing Ga<sub>2</sub>O<sub>3</sub>-based quantum well.

## 5. 2 Raman scattering

Deep ultraviolet optoelectronic devices such as light detectors and emitters are paid more and more attention for their potential applications in biological and chemical agent detection, environmental protection, solar blind detection and high-density data

storage.<sup>23-26</sup> As a wide variable bandgap semiconductor, ternary  $(\text{AlGa})_2\text{O}_3$  is a promising candidate for deep ultraviolet optoelectronic device applications because  $(\text{AlGa})_2\text{O}_3$  has an advantage of large tunable bandgaps from 4.8 eV ( $\text{Ga}_2\text{O}_3$ ) to 8.6 eV ( $\text{Al}_2\text{O}_3$ ) at room temperature.<sup>8,9</sup> In order to realize  $(\text{AlGa})_2\text{O}_3$  application in deep ultraviolet optoelectronic devices, great efforts have made remarkable progress for growing this alloy.<sup>27</sup> In our previous experiment,  $(\text{AlGa})_2\text{O}_3$  thin films were successfully deposited by PLD, and  $\beta$ - $(\text{AlGa})_2\text{O}_3$  thin film could be obtained in the Al content range of 0-0.72.<sup>11</sup> For further development of  $(\text{AlGa})_2\text{O}_3$ -based optoelectronic device, detailed and reliable experimental data on the optical properties of  $\beta$ - $(\text{AlGa})_2\text{O}_3$  thin films must be clearly investigated.

Compared with other spectroscopic techniques, Raman spectroscopy has a great of advantages such as nondestructive, no special sample preparation, and contactless.<sup>28-31</sup> Therefore, it has been widely employed in semiconductors. Kranert *et al.*<sup>10</sup> have reported Raman spectra of  $(\text{AlGa})_2\text{O}_3$  films with different Al content (0-0.55) at room temperature. However, in contrast to the comprehensive investigation of temperature effect of Raman scattering for other semiconductors,<sup>19,32</sup> temperature dependence of phonon behavior in  $\beta$ - $(\text{AlGa})_2\text{O}_3$  thin films has not been reported up to now. The temperature dependent Raman linewidths and shifts can be interpreted in the terms of anharmonic processes which results in a better understanding of electronic properties of  $(\text{AlGa})_2\text{O}_3$  at different temperature.<sup>33</sup> Moreover, it has been demonstrated that the anharmonic constant which was extracted by analyzing anharmonic processes is very important for the  $\text{MgZnO}$ -based light emission device applications.<sup>19</sup> In this work, we

reported on the temperature-dependence Raman scattering of  $\beta$ -(AlGa)<sub>2</sub>O<sub>3</sub> thin films with different Al content (0-0.72) in the temperature range from 77 to 300 K. In combination with detailed theoretical modellings for the frequency downshift and linewidths broadening, we can clearly illustrate the temperature effect on the Raman shift and linewidths in the  $\beta$ -(AlGa)<sub>2</sub>O<sub>3</sub> thin films, which provides an experimental basis for realization of (AlGa)<sub>2</sub>O<sub>3</sub>-based optoelectronic device applications.

The (AlGa)<sub>2</sub>O<sub>3</sub> films used for present research were deposited by PLD using a KrF laser source ( $\lambda = 248$  nm) on (0001) sapphire substrates. The (AlGa)<sub>2</sub>O<sub>3</sub> bulks with Al content in the range of 0-0.72 were used as targets. The oxygen pressure during the growth was maintained at  $1 \times 10^{-1}$  Pa while the substrate temperature was kept at 400°C.<sup>11</sup> The XRD revealed that the (-201), (-402), and (-603) diffraction peaks are observed from (AlGa)<sub>2</sub>O<sub>3</sub> films together with the peak of (0006) reflection from sapphire substrate, indicating the patterns of monoclinic  $\beta$ -(AlGa)<sub>2</sub>O<sub>3</sub>.<sup>11</sup> The atomic concentrations were estimated from XPS element peak area by using an atomic sensitivity factor.<sup>11</sup> The thickness of these (AlGa)<sub>2</sub>O<sub>3</sub> films measured by using a surface step profile analyzer are between 200 and 300 nm. The surface morphologies and root mean square (RMS) roughness of (AlGa)<sub>2</sub>O<sub>3</sub> films were characterized by atomic force microscope (AFM) as shown in figure 5.10.

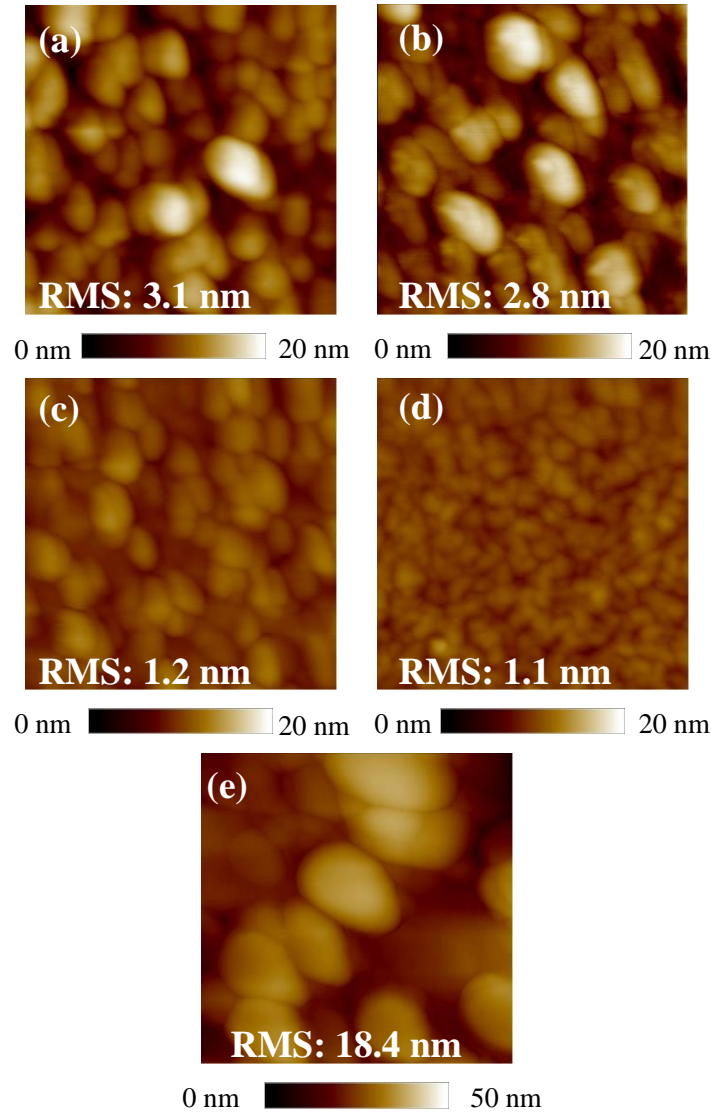


Figure 5.10 AFM images of  $(\text{Al}_x\text{Ga}_{1-x})_2\text{O}_3$  films with different Al content  $x$  of (a) 0, (b) 0.11, (c) 0.22, (d) 0.53, and (e) 0.72, respectively. The scan area is  $1 \times 1 \mu\text{m}^2$ .

The Raman spectra were recorded in the back-scattering geometry of the  $z(x, -)\bar{z}$  configuration<sup>34</sup> by using a Horiba Jobin Yvon LabRAM HR 800 system equipped with an Andor DU420 classic charge-coupled device detector. The 488 nm line of Ar laser was used to excite the samples. The employment of a  $50 \times$  optical microscopy objective with a numerical aperture of 0.5 will yield a laser spot size of  $\sim 0.8 \mu\text{m}$ . A Microstat<sup>HE</sup> hot/cold stage (Oxford instruments) with a quartz window was used to

heat the samples from 77 K to 300 K under flowing nitrogen. The temperature was controlled by a K-type thermocouple which has an accuracy of better than  $\pm 1$  K. For each measurement point, the temperature was kept for 10 min to avoid temperature fluctuations before acquiring a spectrum for 15 min. The power of the laser was set to about 2 mW to avoid thermal contributions coming from the laser.

The monoclinic  $\beta$ -Ga<sub>2</sub>O<sub>3</sub> belongs to the space group  $C2/m/C^3_{2h}$ . The Raman-active modes of  $\beta$ -Ga<sub>2</sub>O<sub>3</sub> can be classified into three groups: low-frequency libration and translation (below 200 cm<sup>-1</sup>) of tetrahedra-octahedra chains, mid-frequency deformation of Ga<sub>2</sub>O<sub>6</sub> octahedra (~310-480 cm<sup>-1</sup>), and high-frequency stretching and bending of GaO<sub>4</sub> tetrahedra (~500-770 cm<sup>-1</sup>).<sup>18</sup> It has 27 optical phonon modes belonging to the irreducible representation

$$\Gamma^{\text{opt}} = 10A_g + 5B_g + 4A_u + 8B_u \quad (1)$$

Where symmetry  $A_g$  and  $B_g$  phonon modes are Raman active while phonon modes with  $A_u$  and  $B_u$  symmetry are infrared active.<sup>36</sup>

Figure 5.11 shows Raman spectra of (Al<sub>x</sub>Ga<sub>1-x</sub>)<sub>2</sub>O<sub>3</sub> films with Al content  $x$  in the range of 0-0.72 measured at room temperature. For Ga<sub>2</sub>O<sub>3</sub> film, six  $A_g$  and three  $B_g$  Raman active modes can be observed. The Raman peaks at 146.2, 169.6, 201.6, 351.3, 483.3, 656.4, and 767.4 cm<sup>-1</sup> correspond to  $B_g^{(2)}$ ,  $A_g^{(2)}$ ,  $A_g^{(3)}$ ,  $A_g^{(5)}$ ,  $A_g^{(7)}/B_g^{(4)}$ ,  $A_g^{(9)}/B_g^{(5)}$ , and  $A_g^{(10)}$  phonon modes, respectively. The peak of  $A_g^{(7)}/B_g^{(4)}$  phonon modes as well as

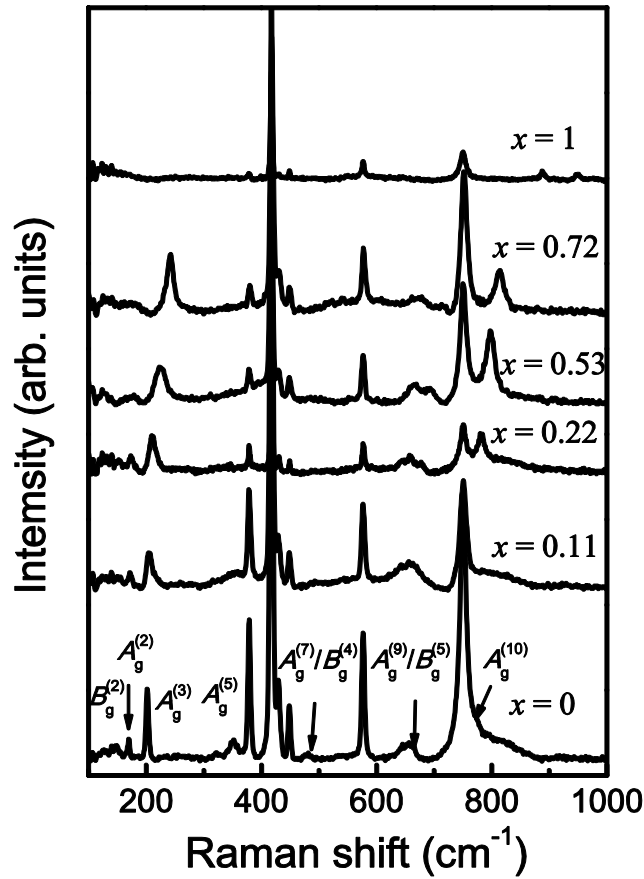


Figure 5.11 Raman spectra of  $\beta$ -(AlGa)<sub>2</sub>O<sub>3</sub> thin film with different Al content at room temperature.

$A_g^{(9)}/B_g^{(5)}$  can't be unambiguously assigned to one of the mode peaks  $A_g^{(7)}$  or  $B_g^{(4)}$  because Raman shifts of  $A_g^{(7)}$  modes is very close to that of  $B_g^{(4)}$  modes. The positions of these mode peaks have good agreements with those of Ga<sub>2</sub>O<sub>3</sub> bulk and nanowires reported by other researchers.<sup>35,36</sup> With the increase of Al content, the Raman active modes of (AlGa)<sub>2</sub>O<sub>3</sub> films have a clear right shift. The Raman spectra also exhibit a line broadening for (AlGa)<sub>2</sub>O<sub>3</sub> films at higher Al content. This broadening is particularly true for the Raman modes in mid-spectral range between 310 and 480 cm<sup>-1</sup>, which is contributed to the more Al atoms entering into the crystal lattices of Ga<sub>2</sub>O<sub>3</sub> to form ternary solid solution. For Al<sub>2</sub>O<sub>3</sub> film, almost no peak can be observed

except the Raman peak of sapphire substrates. Figure 5.12 shows the dependence of the spectral positions of  $A_g^{(3)}$ ,  $A_g^{(9)}/B_g^{(5)}$ , and  $A_g^{(10)}$  phonon modes on the Al content. As shown in figure 5.12, for the Al content range of 0-0.72, the  $A_g^{(3)}$  phonon mode exhibits a shift of  $\sim 41 \text{ cm}^{-1}$ , the  $A_g^{(9)}/B_g^{(5)}$  phonon mode has a shift of  $\sim 65 \text{ cm}^{-1}$ , and the shift is  $A_g^{(10)}$  phonon modes is  $\sim 46 \text{ cm}^{-1}$ .

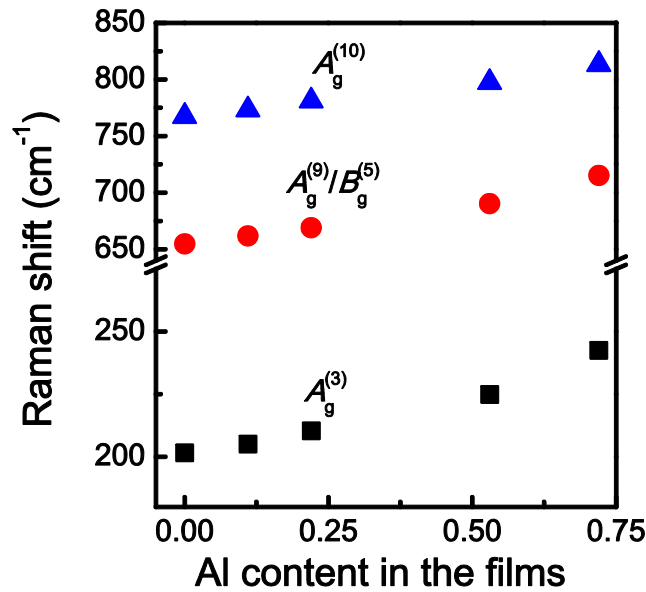


Figure 5.12 Raman shifts of  $A_g^{(3)}$ ,  $A_g^{(9)}/B_g^{(5)}$ , and  $A_g^{(10)}$  phonon modes as a function of Al content.

Next, we measured the temperature-dependent Raman spectra of  $(\text{AlGa})_2\text{O}_3$  films by keeping samples on the stage. Figure 5.13 presents the temperature-dependent Raman spectra of  $(\text{AlGa})_2\text{O}_3$  films with Al content in the range of 0-0.72. The sharp Raman peaks of  $\text{Ga}_2\text{O}_3$  films located at  $201.6$  and  $767.4 \text{ cm}^{-1}$  are attributed to the  $A_g^{(3)}$  and  $A_g^{(10)}$  phonon modes, respectively, while peaks at  $418$ ,  $580$ , and  $754 \text{ cm}^{-1}$  are caused by sapphire substrate. Here, we note that in temperature-dependent Raman measurement process, some of Raman modes disappeared due to absorption of the

window of the stage. These peaks can only be observed at lower temperature. In order to observe the temperature effect on the phonon modes in  $(\text{AlGa})_2\text{O}_3$  films, the enlarged Raman shift spectra of  $A_g^{(3)}$  and  $A_g^{(10)}$  phonon modes were shown in figure 5.14(a) and (b). The black solid curves are experimental Raman spectra. In order to obtain the more accurate information, a curve fitting program by using the Lorentz equation was employed to fit the experimental Raman spectra to determine the Raman shifts and linewidth broadening. The fitting curves are shown as red dash curves in figure 5.14(a) and (b). This approach has been shown to be very powerful for analyzing the contributions of different phonon modes in compound semiconductors such as  $\text{AlInN}$  and  $\text{MgZnO}$ .<sup>19,32</sup>

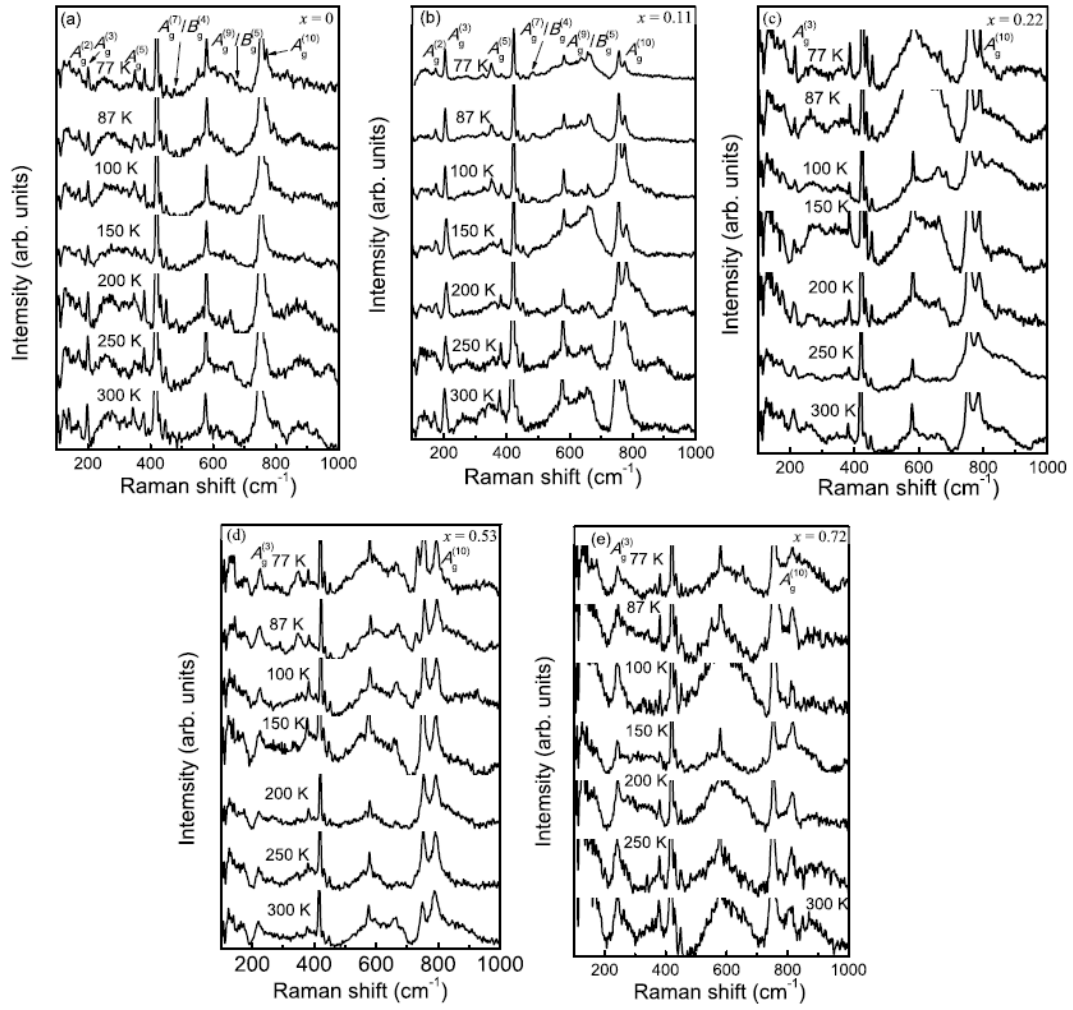


Figure 5.13 Temperature dependence Raman spectra of  $\beta$ -(AlGa)<sub>2</sub>O<sub>3</sub> thin film with different Al content.

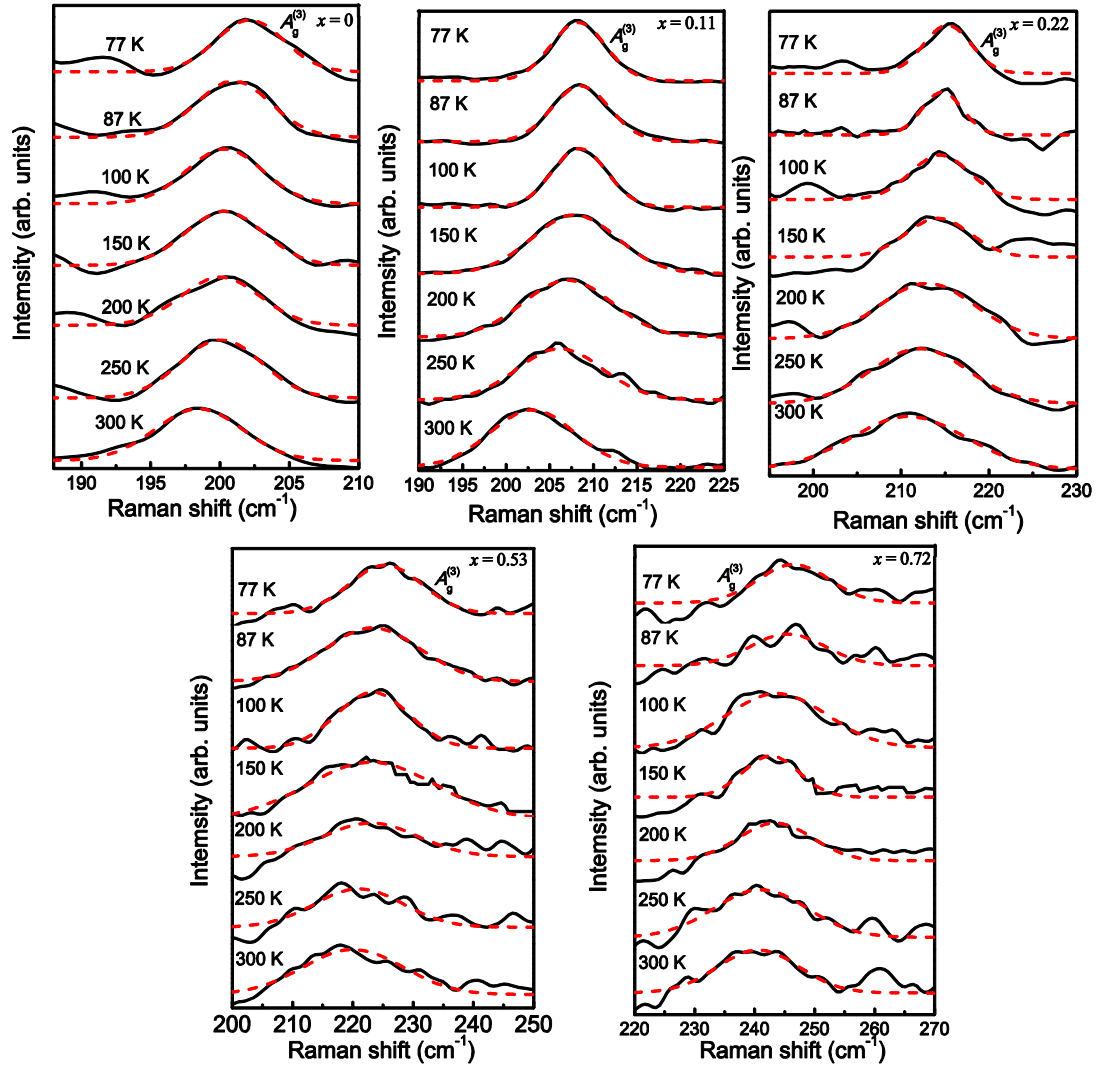


Figure 5.14(a) Enlarge Raman spectra of  $A_g^{(3)}$  modes in  $\beta$ -(AlGa) $_2$ O $_3$  thin films with different Al content.

Figure 5.15 shows the Raman shift of  $A_g^{(3)}$  and  $A_g^{(10)}$  phonon modes with temperature. It is clear that the  $A_g^{(3)}$  and  $A_g^{(10)}$  structure shifts to lower frequency with the increase of temperature. The temperature dependence of Raman shifts exhibit nonlinear behavior at the temperature from 77 to 300 K. In general, several factors are responsible for temperature-dependent Raman shift such as electron-phonon, anharmonic phonon-phonon interactions, and thermal expansion.<sup>37,38</sup> However, for the

effect of thermal expansion, the experimental structural information of  $(\text{AlGa})_2\text{O}_3$ , such as Grüneisen parameters and phonon deformation potentials, was not established up to now. Therefore, there is no generally accurate method to describe the downshift of phonon frequencies in  $(\text{AlGa})_2\text{O}_3$  films with the increase of temperature at this moment.

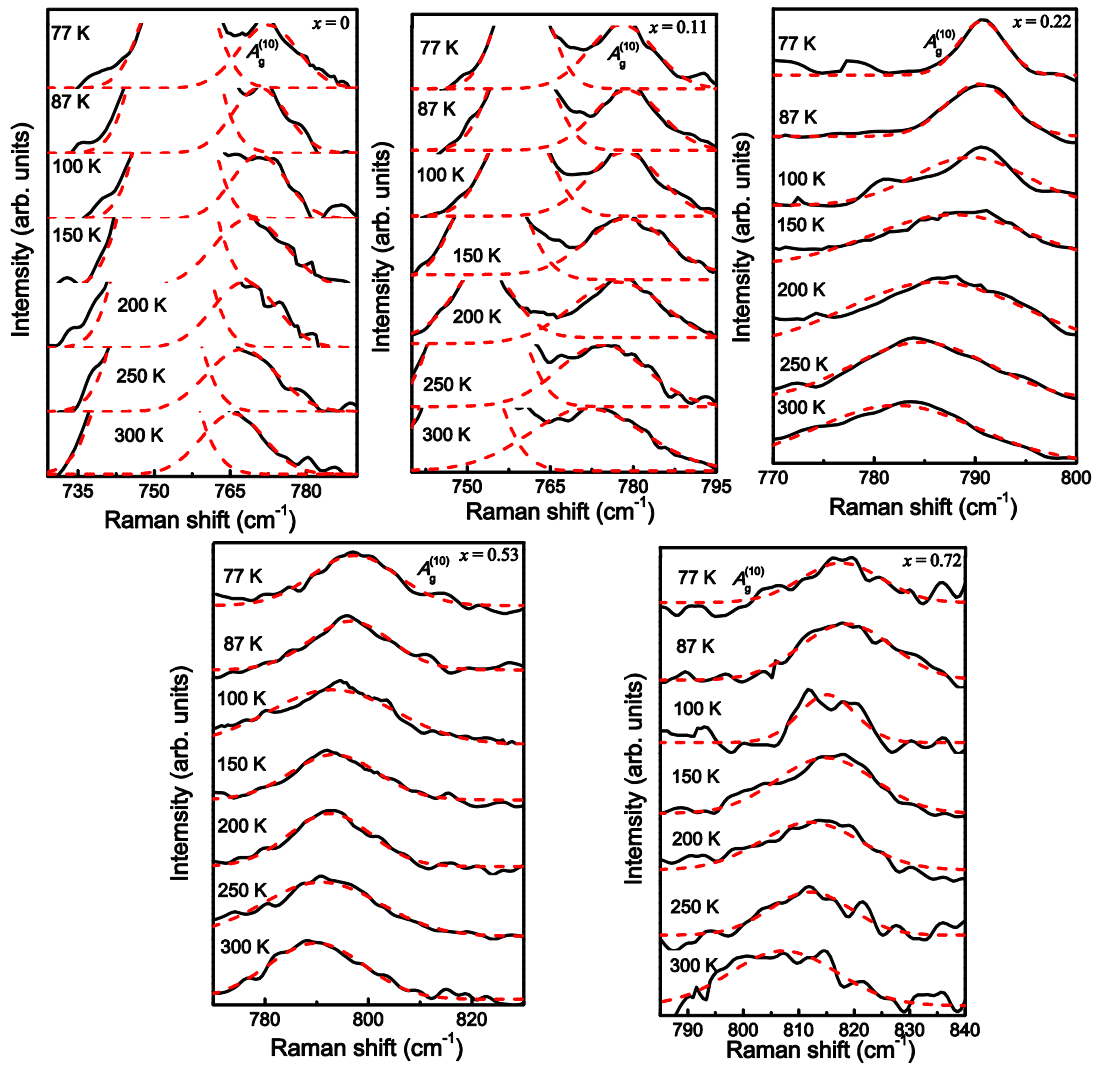


Figure 5.14(b) Enlarge Raman spectra of  $A_g^{(10)}$  modes in  $\beta$ - $(\text{AlGa})_2\text{O}_3$  thin films with different Al content.

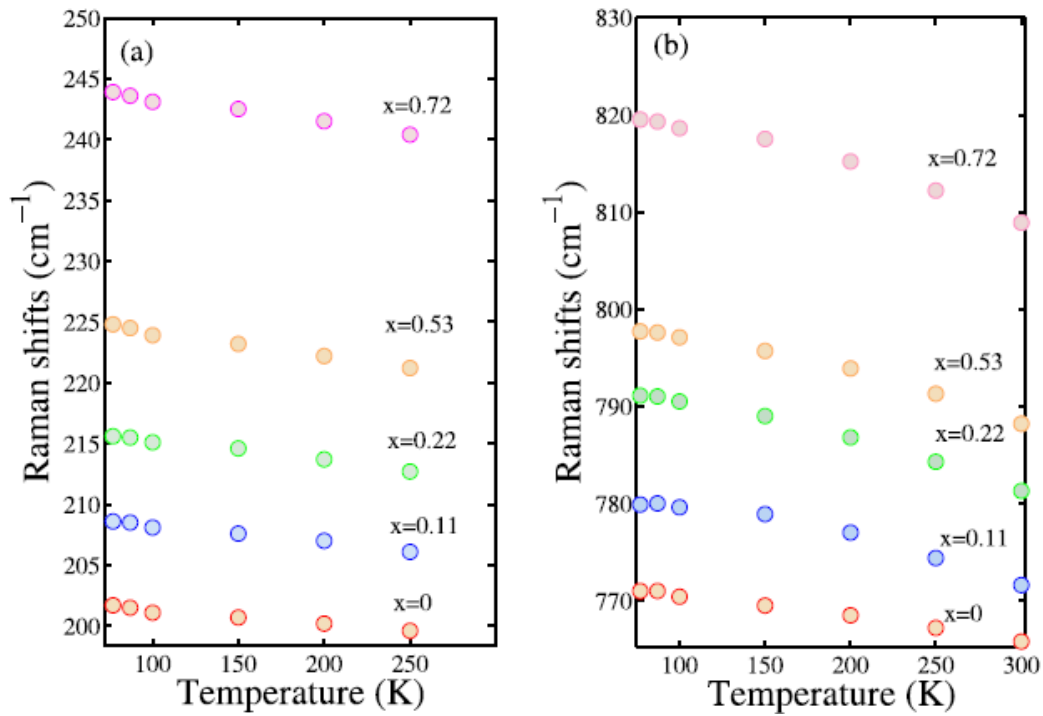


Figure 5.15 Temperature dependence Raman shifts of (a)  $A_g^{(3)}$  and (b)  $A_g^{(10)}$  modes in  $\beta$ -(AlGa) $_2$ O $_3$  thin film with different Al content.

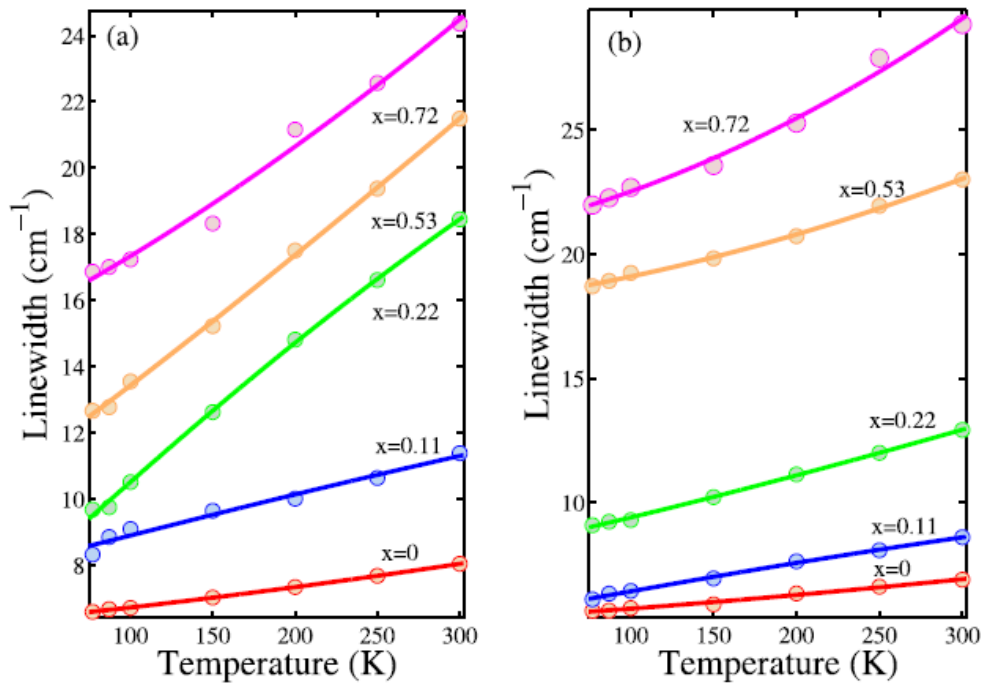


Figure 5.16 Temperature dependence Raman linewidths of (a)  $A_g^{(3)}$  and (b)  $A_g^{(10)}$  modes in  $\beta$ -(AlGa) $_2$ O $_3$  thin film with different Al content.

Figure 5.16 shows the linewidths broadening of  $A_g^{(3)}$  and  $A_g^{(10)}$  phonon modes with temperature. It is clear that the linewidths broadening of  $A_g^{(3)}$  and  $A_g^{(10)}$  phonon modes increase with the increase of the temperature. With the increase of temperature, the thermal agitation increases, giving rise to a decrease in the phonon mean free path, and so the decay lifetime ( $\tau$ ) decreases.<sup>39</sup> The relation between decay lifetime and full width at half maximum (FWHM:  $\Gamma$ ) can be written as  $\tau = 1/(\pi c\Gamma)$ , where  $c$  is velocity of light. Thus, FWHM increases with increasing temperature. Here, the approach developed by Guo *et al.*<sup>40</sup> was employed to explain linewidths broadening of  $A_g^{(3)}$  and  $A_g^{(10)}$  phonon modes. The temperature dependence of linewidths broadening is caused by phenomenon of the optical phonon decay into two (three phonon process) or three (four phonon process) acoustic phonons with equal energies stemming from lattice potential cubic and quartic anharmonicity. The equation can be written as:

$$\begin{aligned}\Gamma(T) &= \Gamma_0 + \Gamma_1 + \Gamma_2 \\ \Gamma_1 &= A [1 + n(T, \omega_1) + n(T, \omega_2)] \\ \Gamma_2 &= B [1 + 3n(T, \omega_0/3) + 3n^2(T, \omega_0/3)]\end{aligned}\quad (2)$$

where  $\Gamma_0$  is the linewidth at 0 K, and the fitting parameter  $A$  and  $B$  are anharmonic constants corresponding to the relative probability of the occurrence of each process.  $n(T, \omega) = [\exp(\hbar\omega/k_B T) - 1]^{-1}$  is the Bose-Einstein function with  $\hbar$  (Planck's constant divided by  $2\pi$ ) and  $k_B$  Boltzmann constant. In equation (2),  $\Gamma_1$  results from the decay of the zone-center phonons into two phonons considered as three phonon process, with  $\omega_1 + \omega_2 = \omega_0$ . In general, the simplest three phonon process for optical phonon decay, proposed by Klemens,<sup>41</sup> is decay into acoustic phonons of equal energy,  $\omega_1 =$

$\omega_2$ , and opposite. And  $\Gamma_2$  corresponds to the decay into three phonons (four phonon process), with the frequency  $\omega_0/3$ .  $\omega_0$  is the harmonic frequency of phonon mode. The solid curves shown in figure 5.16 are the fit of Eq. (2) for the temperature-dependent linewidths broadening of  $A_g^{(3)}$  and  $A_g^{(10)}$  phonon modes. The agreement between the theoretical fit and experimental data is very good. In addition, it is clear that the gradient of fitting curves increases with the increase of the Al content. Similar phenomena were also observed in AlInN and MgZnO alloy materials.<sup>19,32</sup> The fitting parameters  $\Gamma_0$ ,  $A$ , and  $B$  have been obtained as shown in Table 6.1. It is obvious that there is a rapid increase in  $\Gamma_0$  with the increase of Al content because of the formation of lattice defect and structural disorder after Al implantation. Moreover, the dependence of  $\Gamma_0$  on Al content play the closely related behavior with that of Urbach band tail according to report of Jiang, *et al.* In pure Ga<sub>2</sub>O<sub>3</sub> film,  $\Gamma_0$  of  $A_g^{(3)}$  phonon mode is larger than that of  $A_g^{(10)}$  phonon mode, implying that  $A_g^{(3)}$  phonon mode is more strongly affected by impurity and/or defect scattering than that of  $A_g^{(10)}$  phonon mode. However,  $\Gamma_0$  of  $A_g^{(10)}$  phonon mode increases much more rapidly with the increase of Al content than that of  $A_g^{(3)}$  phonon mode. As we know,  $A_g^{(10)}$  phonon mode belongs to high-frequency stretching and bending modes of GaO<sub>4</sub> tetrahedra.<sup>36</sup> The stretching and bending modes involve the shortest Ga-O bonds (1.80 Å) which lead to more lattice defect and structural disorder when Al was implanted. These defects and disorders will result in strong enhancement of the impurity scattering in  $A_g^{(10)}$  phonon mode of (AlGa)<sub>2</sub>O<sub>3</sub> films.<sup>32</sup> It is well known that the constants  $A$  and  $B$  can be related to the lifetime of the optical phonon decay into two (three phonon

process) and three (four phonon process) acoustic phonons, respectively. It has been confirmed the inverse relation between the lifetime and the anharmonic constants.<sup>39</sup> From Table 5.1, it is obvious that the constants  $A$  and  $B$  increase with the increase of Al content. It can be explained that Al atom incorporation makes the more lattice defect and structural disorder which lead to shorten lifetime of decay process.

Table 5.1 Fitting parameters for linewidth broadening of  $A_g^{(3)}$  and (b)  $A_g^{(10)}$  in

$\beta$ -(AlGa)<sub>2</sub>O<sub>3</sub> thin film.

Raman modes	$x$	$\Gamma_0$	$A$	$B$
$A_g^{(3)}$	0	6.17	0.1676	0.0026
	0.11	8.50	0.4655	0.0030
	0.22	9.52	1.396	0.0976
	0.53	12.57	0.8681	0.0363
	0.72	16.61	1.262	0.0459
$A_g^{(10)}$	0	5.24	0.1481	0.0025
	0.11	6.08	0.4573	0.0034
	0.22	8.74	0.5135	0.0049
	0.53	17.87	0.6054	0.0674
	0.72	20.52	0.9693	0.0949

In order to better understand the contributions of the three phonon and four phonon processes in (AlGa)<sub>2</sub>O<sub>3</sub> films, the ratios of  $A$  and  $B$  were calculated. Figure 5.17 displays the ratios of  $A$  and  $B$  for  $A_g^{(3)}$  and  $A_g^{(10)}$  phonon modes of Ga<sub>2</sub>O<sub>3</sub> and (AlGa)<sub>2</sub>O<sub>3</sub> films. It is obvious that the ratios of  $A$  and  $B$  are much larger than 1.0, indicating that the decay into two phonons is the prevailing process while the contribution from the four phonon processes is minor in the anharmonic coupling of  $A_g^{(3)}$  and  $A_g^{(10)}$  phonon modes. This result has a well agreement with the report on Ga<sub>2</sub>O<sub>3</sub> bulk,<sup>35</sup> which further indicates the reliability of our results estimated by

theoretical fitting. For  $(\text{AlGa})_2\text{O}_3$  films, with the increasing of Al content, the ratios of  $A$  and  $B$  for  $A_g^{(3)}$  and  $A_g^{(10)}$  phonon modes decrease, indicating that the contribution from the three phonon process decreases after Al implantation. It can be explained by the increase of  $\omega_0$  in  $(\text{AlGa})_2\text{O}_3$  films leads to larger values of  $\omega_1$  and  $\omega_2$ , which brings on the decrease of the contribution from the four phonon process.<sup>19</sup> Moreover, it should be noted that three phonon process always dominates the linewidths broadening of  $A_g^{(3)}$  and  $A_g^{(10)}$  phonon modes in  $(\text{AlGa})_2\text{O}_3$  films.

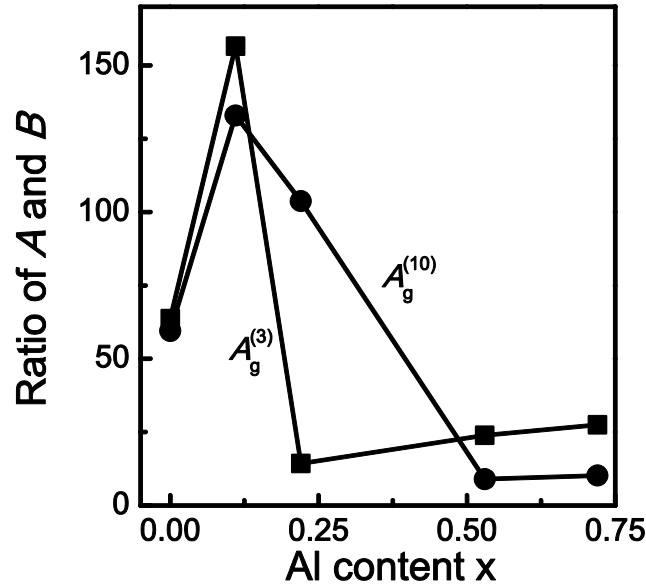


Figure 5.17 Dependence of  $A/B$  on the Al content in  $\beta$ - $(\text{AlGa})_2\text{O}_3$  thin films.

The above results permit us to have a well understanding of the temperature effect on the Raman shift and linewidth in  $(\text{AlGa})_2\text{O}_3$  films, which establishes an experimental base for micro-Raman as a contactless, nondestructive, and fast method to monitor the local temperature during the operation of  $(\text{AlGa})_2\text{O}_3$ -based devices with submicrometer spatial resolution.<sup>32</sup> The obtained temperature and Al content dependence of Raman shift and linewidth can be used for deriving calibration curves

as reported in MgZnO layer.<sup>42</sup> The local temperature for the (AlGa)<sub>2</sub>O<sub>3</sub>-based devices in operation can thus be determined by the calibration curve.<sup>32</sup> Moreover, the information about the anharmonic effect is also important for the (AlGa)<sub>2</sub>O<sub>3</sub>-based device applications, because the degree of lattice disorder in mirrors by Raman microprobe spectroscopy correlates to the strength of facet heating and to the power limit at optical mirror damage.<sup>43,44</sup>

### 5.3 Conclusion

We investigated in detail the substrate temperature influenced on the surface roughness, optical properties and crystal quality of (AlGa)<sub>2</sub>O<sub>3</sub> films grown on (0001) sapphire substrates by PLD. AFM and transmission spectra indicate the (AlGa)<sub>2</sub>O<sub>3</sub> films have smooth surface and high transmittance. XRD, XRC, and Raman spectra analysis shows (AlGa)<sub>2</sub>O<sub>3</sub> film with the good crystal quality can be obtained at substrate temperature of 400 °C. These results will provide an experimental basis for realizing Ga<sub>2</sub>O<sub>3</sub>-based quantum well.

The temperature-dependent Raman shifts and linewidths of the  $A_g^{(3)}$  and  $A_g^{(10)}$  phonon modes were obtained by employing Lorentz fitting. Through the aid of a model involving the contributions of lattice-mismatch-induced strain, thermal expansion, and three and four phonon coupling, the effects of temperature on linewidths broadening were clearly illustrated. We demonstrated the dependence of the linewidths and decay process on the Al content in  $\beta$ -(AlGa)<sub>2</sub>O<sub>3</sub> thin films. It is clearly observed that the three phonon process always dominates the linewidths

broadening of  $A_g^{(3)}$  and  $A_g^{(10)}$  phonon modes in  $(\text{AlGa})_2\text{O}_3$  films. These results will provide an experimental basis for realization of  $(\text{AlGa})_2\text{O}_3$ -based optoelectronic device applications.

## References

- [1] Y. Kokubun, K. Miura, F. Endo, S. Nakagomi, *Appl. Phys. Lett.*, 90, 031912 (2007).
- [2] K. Shimanura, E. Villora, T. Ujiie, and K. Aoki, *Appl. Phys. Lett.*, 92, 021914 (2008).
- [3] R. Suzuki, S. Nakagomi, Y. Kokubun, N. Arai, and S. Ohira, *Appl. Phys. Lett.*, 94, 222102 (2009).
- [4] Y. Li, T. Tokizono, M. Liao, M. Zhong, Y. Koide, I. Yamada, and J. Delaunay, *Adv. Funct. Mater.*, 20, 3972 (2010).
- [5] Y. Sui, Y. Yue, Y. Cao, B. Yao, X. Liu, J. Lang, M. Gao, X. Li, X. Li, and L. Yang, *Ceram. Int.*, 40, 9189 (2014).
- [6] V. Devi, M. Kumar, R. Kumar, B. Joshi, *Ceram. Int.*, 41, 6269 (2015).
- [7] T. Oshima, T. Okuno, N. Arai, Y. Kobayashi, and S. Fujita, *Jpn. J. Appl. Phys.*, 48, 070202 (2009).
- [8] H. Ito, K. Kaneko, and S. Fujita, *Jpn. J. Appl. Phys.*, 51, 1002047 (2012).
- [9] R. Grund, C. Kranert, H. Wenckstern, V. Zviagin, M. Lorenz, and M. Grundmann, *J. Appl. Phys.*, 117, 165371 (2015).
- [10] C. Kranert, M. Jenderka, J. Lenzner, M. Lorenz, H. Wenckstern, R. S. Grund, and M. Grundmann, *J. Appl. Phys.*, 117, 125703 (2015).
- [11] F. Zhang, K. Satio, T. Tanaka, M. Nishio, M. Arita, and Q. Guo, *Appl. Phys. Lett.*, 105, 162107 (2014).

- [12] K. Satio, Y. Inoue, Y. Hayashida, T. Tanaka, Q. Guo, and M. Nishio, *Appl. Surf. Sci.*, 258, 2137 (2012).
- [13] F. Zhang, K. Saito, T. Tanaka, M. Nishio, and Q. Guo, *J. Cryst. Growth*, 387, 96 (2014).
- [14] K. Matsuzaki, H. Hiramatsu, K. Nomura, H. Yanagi, T. Kamiya, M. Hirano, and H. Hosono, *Thin solid films*, 496, 37 (2006).
- [15] X. Wang, K. Saito, T. Tanaka, M. Nishio, and Q. Guo, *J. Aollys Compd.*, 627, 383 (2015).
- [16] X. Wang, K. Saito, T. Tanaka, M. Nishio, T. Nagaoka, M. Arita, and Q. Guo, *Appl. Phys. Lett.*, 107, 022111 (2015).
- [17] Q. Guo, M. Nada, Y. Ding, T. Tanaka, and M. Nishio, *J. Appl. Phys.*, 107, 123525 (2010).
- [18] X. Wang, Z. Chen, F. Zhang, K. Satio, T. Tanaka, M. Nishio, and Q. Guo, *AIP Adv.*, 6, 015111 (2016).
- [19] J. Kong, W. Shen, Y. Zhang, X. Li, and Q. Guo, *Solid State Commun.*, 149,10 (2009).
- [20] P. Verma, S. Abbi, and K. Jain, *Phys. Rev. B*, 51,16660 (1995).
- [21] R. G. Banal, Y. Taniyasu, and H. Yamamoto, *Appl. Phys. Lett.*, 105, 053104 (2014).
- [22] D. J. Eaglesham, and M. Cerullo, *Appl. Phys. Lett.*, 58, 2276 (1991).
- [23] M. Khizar, Z. Y. Fan, K. H. Kim, J. Y. Lin and H. X. Jiang, *Appl. Phys. Lett.*, 86, 173504 (2005).

- [24] Z. Ren, Q. Sun, S. Y. Kwon, J. Han, K. Davitt, Y. K. Song, A. V. Nurmikko, H. K. Cho, W. Liu, J. A. Smart, and L. J. Schowalter, *Appl. Phys. Lett.*, 91, 051116 (2007).
- [25] L. Wang, H. Xu, C. Zhang, X. Li, Y. Liu, X. Zhang, Y. Tao, Y. Huang, and D. chen, *J. Alloys Compd.*, 513, 399 (2012).
- [26] L. Wang, J. Ma, H. Xu, C. Zhang, X. Ling, and Y. Liu, *Appl. Phys. Lett.*, 102, 031905 (2013).
- [27] G. L. Li, F. B. Zhang, Y. T. Cui, H. Oji, J. Y. Son, and Q. X. Guo, *Appl. Phys. Lett.*, 107, 022109 (2015).
- [28] J.R. Shealy and G. W. Wicks, *Appl. Phys. Lett.*, 50, 1173 (1987).
- [29] I. Calizo, A. A. Balandin, W. Bao, F. Miao, C. N. R. Rao, *Nano Lett.*, 7, 2645 (2007).
- [30] T. T. Kang, A. Hashimoto, and A. Yamamoto, *Phys. Rev. B*, 79, 033301 (2009).
- [31] A.A. Balandin, *Nature Mater.*, 10, 569 (2011).
- [32] L. F. Jiang, J. F. Kong, W. Z. Shen, and Q. X. Guo. *J. Appl. Phys.*, 109, 113514 (2011).
- [33] M. S. Liu, L. A. Bursill, S. Prawer, and K. W. Nugent, *Appl. Phys. Lett.*, 74, 3125 (1999).
- [34] Q. X. Guo, M. Nada, Y. Ding, T. Tanaka, and M. Nishio, *J. Appl. Phys.*, 107, 123525 (2010).
- [35] R. Rao, A. M. Rao, B. Xu, J. Dong, S. Sharma, M. K. Sunkara, *J. Appl. Phys.*, 98, 094312 (2005).
- [36] D. Dohy, and J. Gavarri, *J. Solid State Chem.*, 45, 180(1982).

- [37] W. S. Li, Z. X. Shen, Z. C. Feng, and S. J. Chua, *J. Appl. Phys.*, **87**, 3332 (2000).
- [38] X. D. Pu, J. Chen, and W. Z. Shen, H. Ogawa, and Q. X. Guo, *J. Appl. Phys.*, **98**, 033527 (2005).
- [39] P. Verma, S. C. Abbi, and K. P. Jain, *Phys. Rev. B*, **51**, 16660 (1995).
- [40] L. L. Guo, Y. H. Zhang, and W. Z. Shen, *Appl. Phys. Lett.*, **89**, 161920 (2006).
- [41] P. G. Klemecs, *Phys. Rev. B*, **148**, 845 (1966).
- [42] A. Link, K. Bitzer, W. Limmer, R. Sauer, C. Kirchner, V. Schwegler, M. Kamp, D. G. Ebling, K. W. Benz, *J. Appl. Phys.*, **86**, 6256 (1999).
- [43] P. W. Eppwelein, P. Buchmann, A. Jakubowicz, *Appl. Phys. Lett.*, **62**, 455 (1993).
- [44] J. Jimenez, E. Martin, A. Torres, J. P. Landesman, *Phys. Rev. B*, **58**, 10463 (1998).

## Chapter 6

### Raman scattering in $(\text{In}_x\text{Ga}_{1-x})_2\text{O}_3$ films

#### 6.1. Introduction

$(\text{InGa})_2\text{O}_3$  alloys have attracted considerable attention as promising materials for ultraviolet (UV) optoelectronic applications such as light emitters and detectors,<sup>1-4</sup> because their bandgaps are content tunable in a wide range of energies (3.7-4.9 eV depending on the In content).<sup>5,6</sup> A crucial step for optoelectronic applications is to develop quantum well (QW) structure following the bandgap engineering.<sup>7,8</sup> In our previous work,  $(\text{InGa})_2\text{O}_3$  films were successfully deposited by pulsed laser deposition (PLD) in all In content range and the difference of bandgap energies between  $\text{In}_2\text{O}_3$  and  $(\text{In}_{0.83}\text{Ga}_{0.17})_2\text{O}_3$  films has been confirmed as 0.25 eV which is suited for designing the  $\text{In}_2\text{O}_3$ -based QW.<sup>9</sup> In order to realize high-efficiency  $\text{In}_2\text{O}_3$ -based QW, the detailed and reliable information on the structural characteristics of both well and barrier layers must be clearly investigated.

Raman spectroscopy, as a convenient, effective, and nondestructive method for studying the lattice vibration characteristics, has been widely employed for  $(\text{InGa})_2\text{O}_3$  films.<sup>10,11</sup> Kranert *et al.*<sup>10</sup> have reported Raman spectra of  $(\text{InGa})_2\text{O}_3$  films with different In content (0-0.33) at room temperature. Regoutz *et al.*<sup>11</sup> have presented typical Raman peaks related the disorder-active modes of cubic  $(\text{InGa})_2\text{O}_3$  films grown in the high In content range (0.9-1) at room temperature and the major phonon modes have blueshift due to the strain caused by defects and the broadened linewidth

to the deterioration of crystal structure in comparison with the Raman scattering of  $\text{In}_2\text{O}_3$ . Though great efforts have been made in the investigation of  $(\text{InGa})_2\text{O}_3$  alloy by Raman spectroscopy, temperature-dependent Raman scattering of cubic  $(\text{InGa})_2\text{O}_3$  thin films have not been reported up to now. It is well known that temperature-dependent Raman scattering can be used to obtain the information of phonon decay which is an essential aspect to understand the phonon behaviors.<sup>12</sup> Moreover, the particular temperature coefficients for different Raman active modes can also be estimated by temperature-dependent Raman scattering, which can be used to obtain structural information.<sup>13</sup> In this chapter, we report the temperature-dependent Raman scattering of cubic  $(\text{In}_{0.83}\text{Ga}_{0.17})_2\text{O}_3$  and  $\text{In}_2\text{O}_3$  thin films in the temperature range from 77 to 500 K. In combination with detailed theoretical modellings for the Raman downshift and linewidths broadening, we can clearly illustrate the influence of temperature on the Raman shifts and linewidths in the cubic  $(\text{InGa})_2\text{O}_3$  and  $\text{In}_2\text{O}_3$  thin films.

## 6.2 Experiment

$(\text{InGa})_2\text{O}_3$  thin films were grown by pulsed laser deposition (PLD) using a KrF laser source ( $\lambda=248$  nm) on (0001) sapphire substrates. Before growth, the sapphire substrates were cleaned in organic solvents by in an ultrasonic cleaning system, and then chemically etched in a hot  $\text{H}_3\text{PO}_4$ :  $\text{H}_2\text{SO}_4$  (1:3) solution.<sup>14</sup> In the growth chamber, facing the substrate, the bulks with the In contents of 0.9 and 1 (mole ratio of In / (Ga + In)) were set as the target. The pulsed laser with a frequency of 1 Hz was irradiated

and the distance between target and substrate was about 30 mm. The energy of the pulsed laser was set 225 mJ for deposition. The oxygen pressure of the growth chamber was  $1 \times 10^{-1}$  Pa by introducing high purity oxygen gas (99.999%). In the deposition, the substrate temperature was set as 500 °C and the deposition time was 3 h for these films.

After deposition, energy dispersive X-ray spectroscopy results revealed that the  $(\text{InGa})_2\text{O}_3$  thin films grown with the In contents of 0.9 and 1 in the targets have the In contents of 0.83 and 1 in the films, respectively.<sup>9</sup> The surface morphology and RMS roughness of  $(\text{InGa})_2\text{O}_3$  thin films were studied by AFM. The crystal structures of  $(\text{InGa})_2\text{O}_3$  thin films were evaluated by using XRD. Raman scattering was performed on a Horiba Jobin Yvon LabRAM HR 800 system equipped with an Andor DU420 classic charge-coupled detector. Raman experiments were carried out by using an argon ion laser (488 nm) as the excitation source. A Microstat<sup>HE</sup> hot/cold stage (Oxford instruments) with quartz window was used to heat the films from 77 to 500 K under flowing nitrogen. The temperature was controlled by a K-type thermocouple which has an accuracy of better than  $\pm 1$  K. For each measurement point, the temperature was kept for 10 min to avoid temperature fluctuations before acquiring a spectrum for 10 min.<sup>15</sup>

### 6.3. Results and discussion

Fig. 6.1 shows AFM images of  $\text{In}_2\text{O}_3$  and  $(\text{In}_{0.83}\text{Ga}_{0.17})_2\text{O}_3$  films. The surface morphologies of both  $\text{In}_2\text{O}_3$  and  $(\text{In}_{0.83}\text{Ga}_{0.17})_2\text{O}_3$  films are very flat as seen in figure.

The RMS roughness of  $(\text{InGa})_2\text{O}_3$  films are also marked in Fig. 6.1. It is well known that the exciton localization effect in quantum well structure is enhanced by increasing the thickness of well layer up to a certain value. If the thickness of well layer is further increased to above this value, the exciton localization effect becomes weak.<sup>16</sup> Finally, the exciton localization effect cannot be observed. According to previous reports, the value is about 2.5 nm for GaN/InGaN QW<sup>16</sup> and 4 nm for ZnO/MgZnO QW.<sup>17</sup> The smaller roughness of both well and barrier layer is essential for quantum well structure. In this work, thicknesses of cubic  $\text{In}_2\text{O}_3$  and  $(\text{In}_{0.83}\text{Ga}_{0.17})_2\text{O}_3$  films measured by a surface step profile analyzer are 352 and 346 nm, respectively. The roughness of the  $\text{In}_2\text{O}_3$  and  $(\text{In}_{0.83}\text{Ga}_{0.17})_2\text{O}_3$  films are 1.24 and 2.57 nm, respectively. The roughness of both  $\text{In}_2\text{O}_3$  and  $(\text{In}_{0.83}\text{Ga}_{0.17})_2\text{O}_3$  films is small enough to meet the requirement of  $\text{In}_2\text{O}_3$ -based QW.

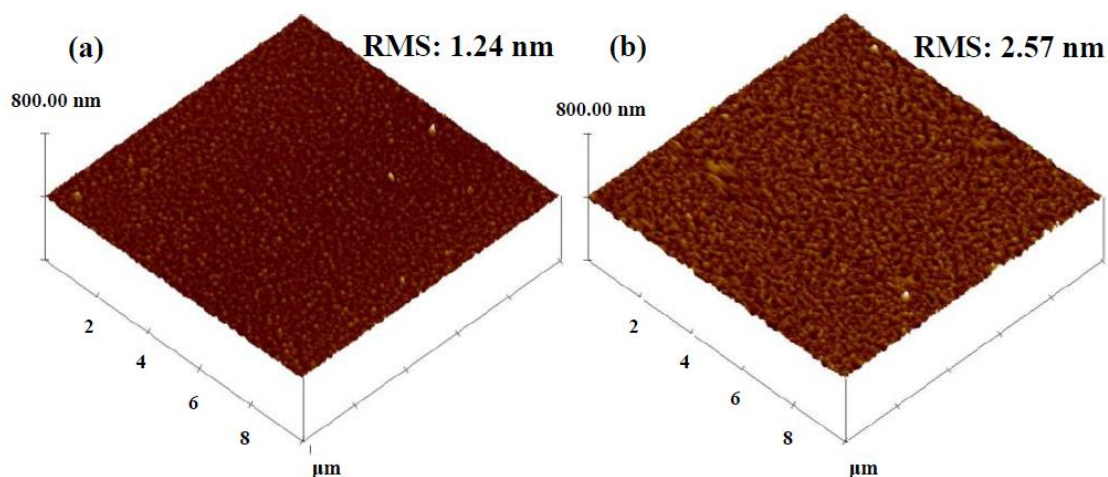


Figure 6.1 AFM morphologies of  $(\text{InGa})_2\text{O}_3$  films grown with the In content of (a) 1 and (b) 0.83. The scan area is  $10 \times 10 \mu\text{m}^2$ .

Next, we investigate the crystal structure of  $\text{In}_2\text{O}_3$  and  $(\text{In}_{0.83}\text{Ga}_{0.17})_2\text{O}_3$  films by

XRD in the  $\theta$ - $2\theta$ -mode as shown in Fig. 6.2. Both  $\text{In}_2\text{O}_3$  and  $(\text{In}_{0.83}\text{Ga}_{0.17})_2\text{O}_3$  films exhibit two peaks (111) and (222) in XRD patterns together with the peak of the (0006) reflection from (0001) sapphire substrate, indicating that the (111) axis of these two samples is perpendicular to the surface of the sapphire substrate. The lattice constants of  $(\text{InGa})_2\text{O}_3$  films grown with the In content of 1 and 0.83 are 5.10 and 5.07 Å, respectively, at room temperature, giving a lattice mismatch of 0.5% between  $\text{In}_2\text{O}_3$  and  $(\text{In}_{0.83}\text{Ga}_{0.17})_2\text{O}_3$  films, which is expressed by  $(a_{\text{In}_2\text{O}_3} - a_{(\text{In}_{0.83}\text{Ga}_{0.17})_2\text{O}_3}) / a_{(\text{In}_{0.83}\text{Ga}_{0.17})_2\text{O}_3}$ .<sup>18</sup> Since threading dislocation induced by lattice mismatch between well and barrier layers can limit the emission efficiency, this small lattice mismatch between  $\text{In}_2\text{O}_3$  and  $(\text{In}_{0.83}\text{Ga}_{0.17})_2\text{O}_3$  films indicates that the  $(\text{InGa})_2\text{O}_3$  films grown in this work are well suited to form  $\text{In}_2\text{O}_3$ -based QW.

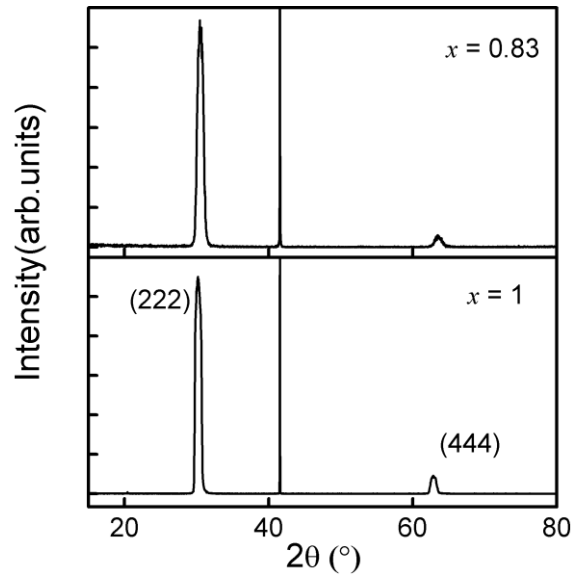


Figure 6.2 XRD patterns of  $\text{In}_2\text{O}_3$  and  $(\text{In}_{0.83}\text{Ga}_{0.17})_2\text{O}_3$  films.

Since the primitive cell of cubic  $\text{In}_2\text{O}_3$  contains eight formula units, group theory predicts the cubic  $\text{In}_2\text{O}_3$  have 120 vibrational modes with the following

representation<sup>19,20</sup>:

$$\Gamma^{\text{opt}} = 4 A_g + 4 E_g + 14 T_g + 5 A_u + 5 E_u + 16 T_u,$$

where  $A_g$ ,  $E_g$ , and  $T_g$  are Raman-active modes,  $A_u$  and  $E_u$  represent silent modes, and  $T_u$  is infrared-active modes. Fig. 6.3 shows the Raman spectra measured at room temperature for  $\text{In}_2\text{O}_3$  and  $(\text{In}_{0.83}\text{Ga}_{0.17})_2\text{O}_3$  films. The peaks at 376.1, 415.4, 428.8, 447, 576.4, and 749.5  $\text{cm}^{-1}$  marked by cross symbols are caused by sapphire substrate as seen in figure.<sup>21</sup> For  $\text{In}_2\text{O}_3$  film, three  $A_g$  and three  $T_g$  Raman active modes can be observed. The Raman peaks at 131.9, 309.4, 367.8, 500.2, and 636.3  $\text{cm}^{-1}$  correspond to  $A_g^{(1)}$ ,  $A_g^{(2)}/T_g^{(2)}$ ,  $T_g^{(3)}$ ,  $A_g^{(3)}$ , and  $T_g^{(4)}$  phonon modes, respectively. The peak of  $A_g^{(2)}/T_g^{(2)}$  phonon modes can't be unambiguously assigned to one of the mode peaks  $A_g^{(2)}$  or  $T_g^{(2)}$  because peak position of  $A_g^{(2)}$  mode is very close to that of  $T_g^{(2)}$  mode. The peak at 131.9  $\text{cm}^{-1}$  is assigned to the In-O vibration of  $\text{InO}_6$  structure units. The scattering feature at 309.4  $\text{cm}^{-1}$  is usually interpreted as the bending vibration of octahedrons. The other two peaks at 500.2, and 636.3  $\text{cm}^{-1}$  are the stretching vibrations of the same octahedrons, whereas the peak at 367.8  $\text{cm}^{-1}$  is assigned to the stretching vibrations of the In-O-In, which also reflects the oxygen vacancies in the  $\text{In}_2\text{O}_3$  film.<sup>22</sup> The positions of these mode peaks are in good agreements with those of  $\text{In}_2\text{O}_3$  bulk and nanostructure reported by other groups.<sup>20,23</sup> In comparison with the  $\text{In}_2\text{O}_3$  film, the Raman active modes of  $(\text{In}_{0.83}\text{Ga}_{0.17})_2\text{O}_3$  film have clear blueshift and a linewidth broadening, which can be contributed to the Ga atoms entering into the crystal lattices of  $\text{In}_2\text{O}_3$  to form ternary solid solution. The relative intensity of the peak at 367.8  $\text{cm}^{-1}$  for  $(\text{InGa})_2\text{O}_3$  film is lower than that for  $\text{In}_2\text{O}_3$  films, implying

(InGa)<sub>2</sub>O<sub>3</sub> film possess less oxygen vacancy.<sup>24</sup>

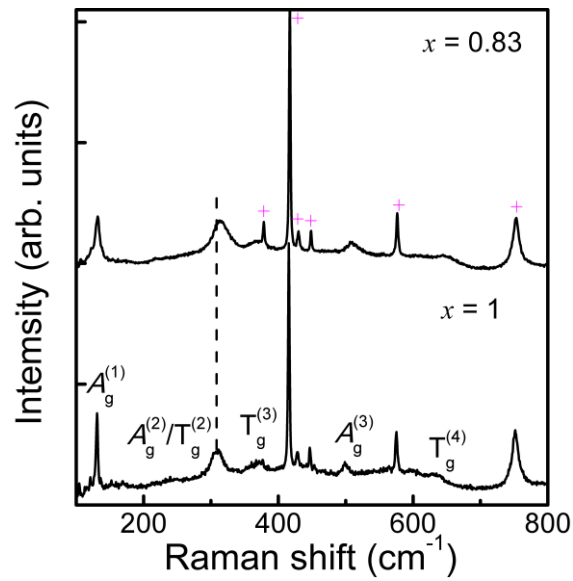


Figure 6.3 Raman spectra of In<sub>2</sub>O<sub>3</sub> and (In<sub>0.83</sub>Ga<sub>0.17</sub>)<sub>2</sub>O<sub>3</sub> films at room temperature.

Peaks marked by cross symbols belong to sapphire substrate.

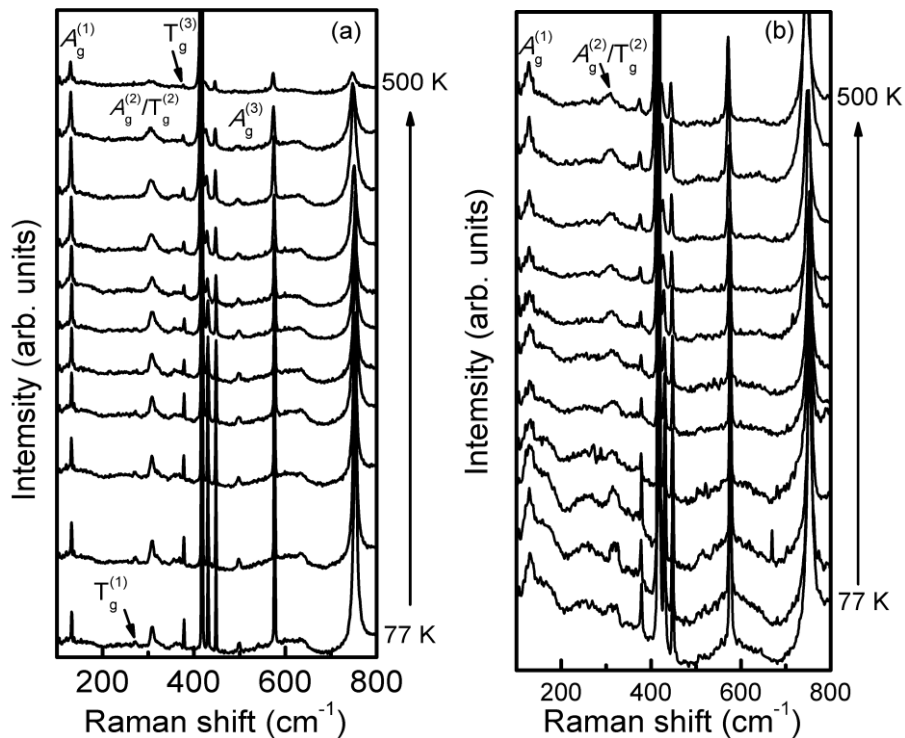


Figure 6.4 Temperature-dependent Raman spectra of cubic (a) In<sub>2</sub>O<sub>3</sub> and (b)

(In<sub>0.83</sub>Ga<sub>0.17</sub>)<sub>2</sub>O<sub>3</sub> films.

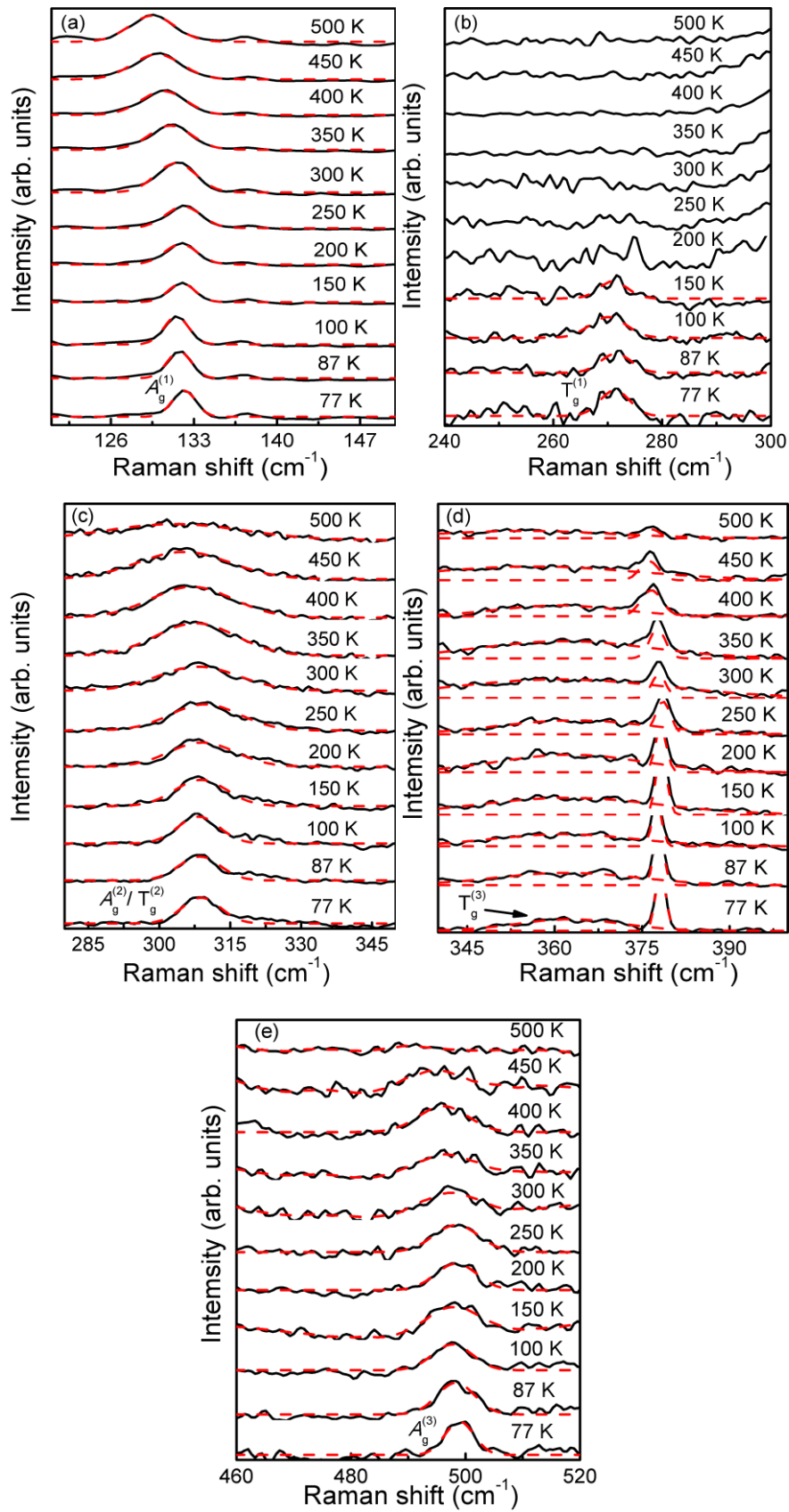


Figure 6.5 Enlarge Raman spectra of (a)  $A_g^{(1)}$ , (b)  $T_g^{(1)}$ , (c)  $A_g^{(2)}/T_g^{(2)}$ , (d)  $T_g^{(3)}$ , and (e)

$A_g^{(3)}$  modes in cubic  $\text{In}_2\text{O}_3$  film.

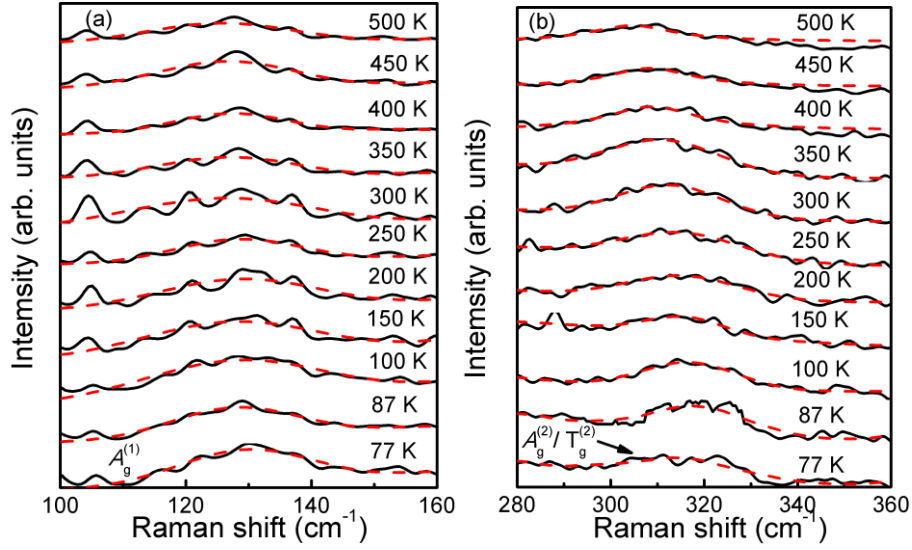


Figure 6.6 Enlarge Raman spectra of (a)  $A_g^{(1)}$ , and (b)  $A_g^{(2)}/T_g^{(2)}$  modes in cubic

$(\text{In}_{0.83}\text{Ga}_{0.17})_2\text{O}_3$  film.

Next, the temperature-dependent Raman spectra of  $\text{In}_2\text{O}_3$  and  $(\text{In}_{0.83}\text{Ga}_{0.17})_2\text{O}_3$  films were measured by keeping sample on the stage. In Fig. 6.4(a) and (b), the measured Raman spectra are shown for selected temperatures between 77 and 500 K. For  $\text{In}_2\text{O}_3$  film, in spectra measured at 77 K, six Raman peaks are observed at 132.3, 270.5, 308.6, 362.6, and 499.0  $\text{cm}^{-1}$  corresponding to  $A_g^{(1)}$ ,  $T_g^{(1)}$ ,  $A_g^{(2)}/T_g^{(2)}$ ,  $T_g^{(3)}$ , and  $A_g^{(3)}$  modes, respectively. For  $(\text{In}_{0.83}\text{Ga}_{0.17})_2\text{O}_3$  films, three main Raman modes  $A_g^{(1)}$  and  $A_g^{(2)}/T_g^{(2)}$  are observed at 133.6 and 316.1  $\text{cm}^{-1}$ , respectively. Here, we note that the  $T_g^{(4)}$  mode disappears owing to absorption of the window of the stage in temperature-dependent Raman measurement process. In order to observe the temperature effect on the phonon modes in  $\text{In}_2\text{O}_3$  and  $(\text{In}_{0.83}\text{Ga}_{0.17})_2\text{O}_3$  films, enlarged Raman spectra of Raman active modes of  $\text{In}_2\text{O}_3$  and  $(\text{In}_{0.83}\text{Ga}_{0.17})_2\text{O}_3$  films are presented in Fig. 6.5 and Fig. 6.6, respectively. The black solid curves are

experimental Raman spectra. A curve fitting program operated in commercial software is used to fit Raman spectra to determine the Raman shift and linewidth broadening. This program allows peak fitting using combination of Gauss or Lorentz peak profiles and the subtraction of a background. A pure Lorentz profile and a linear background were selected in this fitting, because it has been demonstrated that a better fit to data can be obtained by using Lorentz peak profiles in the report of Smit et al.<sup>25</sup>. The standard error of the peak position varies from 0 to 0.4 cm<sup>-1</sup> in the process of peak fitting. The fitting curves are shown as red dash curves in figures. This method has been demonstrated to be very powerful for analyzing the contributions of different modes in (AlGa)<sub>2</sub>O<sub>3</sub> films.<sup>15</sup> It is clear that all the Raman active modes of In<sub>2</sub>O<sub>3</sub> and (In<sub>0.83</sub>Ga<sub>0.17</sub>)<sub>2</sub>O<sub>3</sub> films exhibit downshift and linewidth broadening with the increase of temperature.

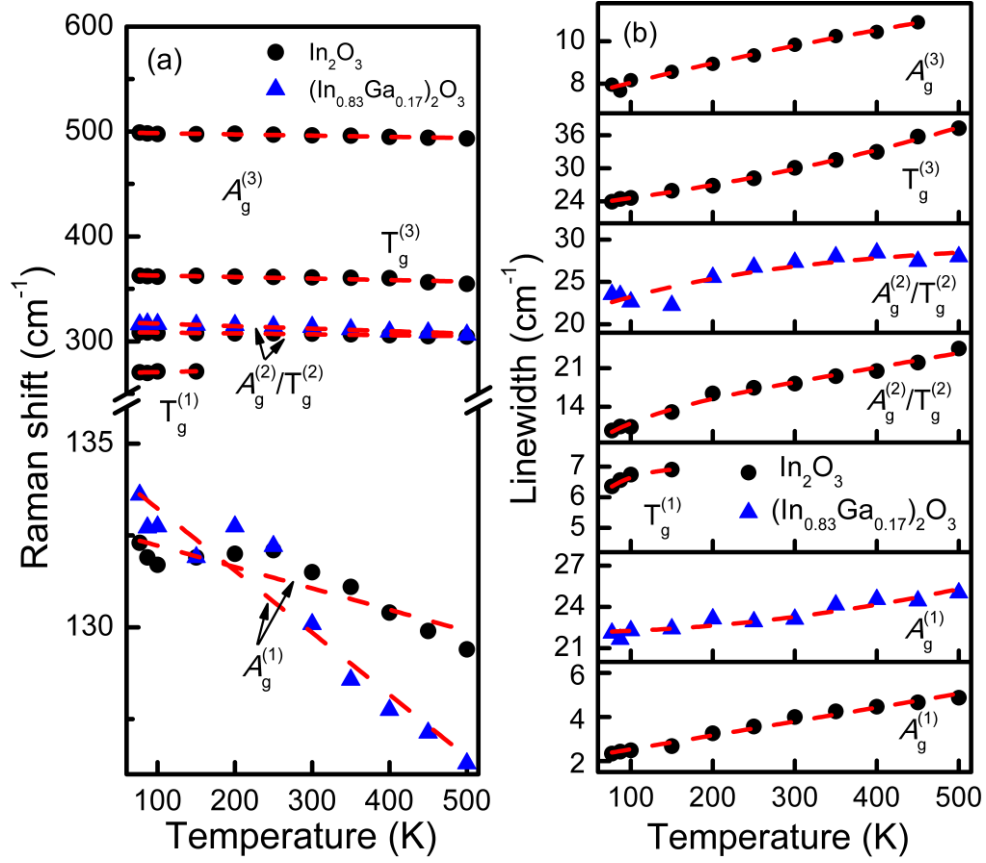


Figure 6.7 Temperature-dependent (a) Raman shifts and (b) linewidths of different modes in cubic  $\text{In}_2\text{O}_3$  and  $(\text{In}_{0.83}\text{Ga}_{0.17})_2\text{O}_3$  films. The data represented by black circle belong to  $\text{In}_2\text{O}_3$  film while that represented by blue triangle belong to  $(\text{In}_{0.83}\text{Ga}_{0.17})_2\text{O}_3$  film. The red dash lines are fitting curves.

In the following, we focus on the temperature dependence of Raman active modes. The Raman shift and linewidth broadening of  $A_g^{(1)}$ ,  $T_g^{(1)}$ ,  $A_g^{(2)}/T_g^{(2)}$ ,  $T_g^{(3)}$ , and  $A_g^{(3)}$  modes in  $\text{In}_2\text{O}_3$  film are displayed as a function of the temperature in Fig. 6.7. The Raman shifts of these six modes vary linearly with temperature as shown in Fig. 6.7(a), which can be described by first order temperature coefficient. The data of Raman shift are fitted by using the following equation<sup>26</sup>:

$$\omega(T) = \omega_0 + \chi \times T \quad (1)$$

where  $\omega_0$  is the Raman shift of phonon mode at zero Kelvin temperature and  $\chi$  is the first order temperature coefficient of the phonon mode. The plot of each mode versus temperature gives straight line as shown in Fig. 6.7(a) and the slope of the fitted line is the value of temperature coefficient  $\chi$ . On the other side, some factors are responsible for temperature-dependent linewidth broadening of different modes in  $\text{In}_2\text{O}_3$  film like electron-phonon, anharmonic phonon-phonon interactions, and thermal expansion.

Table 6.1 Fitting parameters for Raman shift [Eq. (1)] and linewidth [Eq. (2)] of cubic  $\text{In}_2\text{O}_3$  film.

Phonon modes	$A_g^{(1)}$	$T_g^{(1)}$	$A_g^{(2)}/T_g^{(2)}$	$T_g^{(3)}$	$A_g^{(3)}$
$\omega_0$ (cm <sup>-1</sup> )	133.5 ± 0.3	269.4 ± 1.2	309.2 ± 0.3	364.5 ± 0.08	499.8 ± 0.3
$\chi$ (cm <sup>-1</sup> /K)	-0.006 ± 0.001	0.012 ± 0.006	-0.009 ± 0.001	-0.014 ± 0.003	-0.012 ± 0.001
$\Gamma_0$ (cm <sup>-1</sup> )	1.566 ± 0.016	5.968 ± 0.002	5.546 ± 0.025	22.585 ± 0.010	7.020 ± 0.009
$A$ (cm <sup>-1</sup> )	-0.0100 ± 0.0005	-1.2530 ± 0.0024	-0.0196 ± 0.0021	-0.0183 ± 0.0014	-0.0105 ± 0.0006
$B$ (cm <sup>-1</sup> )	-0.0017 ± 0.0001	0.0493 ± 0.0015	-0.0022 ± 0.0001	-0.0018 ± 0.0002	-0.0010 ± 0.0001

Here, in order to describe linewidth broadening with temperature, the method developed by Balkanski *et al.*<sup>12</sup> is employed to explain linewidth broadening of  $A_g^{(1)}$ ,  $T_g^{(1)}$ ,  $A_g^{(2)}/T_g^{(2)}$ ,  $T_g^{(3)}$ , and  $A_g^{(3)}$  modes. The temperature-dependent linewidth broadening is induced by phenomenon of the optical phonon decay into two (three phonon process) or three (four phonon process) acoustic phonons with equal energies stemming from lattice potential cubic and quartic anharmonicity. The data of linewidth broadening can be explained by the following equation<sup>15</sup>:

$$\Gamma(T) = \Gamma_0 + A [1 + 2 / (e^x - 1)] + B \{1 + [3 / (e^y - 1)] + [3 / (e^y - 1)^2]\} \quad (2)$$

where  $\Gamma_0$  is the linewidth at zero Kelvin temperature,  $A$  and  $B$  are anharmonic

constants corresponding to three phonon process and four phonon process, respectively,  $x = \hbar\omega_0/2k_B T$ ,  $y = \hbar\omega_0/3k_B T$ ,  $\hbar$  is Planck's constant divided by  $2\pi$  and  $k_B$  is Boltzmann constant. The red dash curves shown in Fig. 6.7(b) are the fit of Eq. (2) for the temperature-dependent linewidths broadening of different phonon modes. The fitting parameters  $\omega_0$ ,  $\chi$ ,  $\Gamma_0$ ,  $A$ , and  $B$  have been obtained as shown in Table 6.1 for  $\text{In}_2\text{O}_3$  film. It is obvious that a large difference is observed between the temperature-dependent Raman downshifts for phonon modes of  $\text{In}_2\text{O}_3$  film. The most intensive peak of  $A_g^{(1)}$  phonon modes is shifted by about  $3.15 \text{ cm}^{-1}$  for the temperature increase from 77 to 500 K and the value of temperature coefficient is about  $0.006 \text{ cm}^{-1}/\text{K}$ . This value of temperature coefficient is smaller than those of GaN film ( $0.017 \text{ cm}^{-1}/\text{K}$  for  $A_g^{(1)}$  mode)<sup>13</sup> and GaAs film ( $0.018 \text{ cm}^{-1}/\text{K}$  for  $A_{\text{LO1}}$  mode),<sup>27</sup> which are widely employed as well layer in QW structure. The smaller temperature coefficient suggests lower anharmonicity of Raman-active mode in  $\text{In}_2\text{O}_3$  film. The thermal expansion of the crystal is technically considered an anharmonic effect, it is a distinct physical phenomenon from the anharmonic coupling between phonons.<sup>28</sup> It is expected that thermal expansion to play a minimal role in quantum well structure. The maximum value of temperature coefficient  $\chi$  can be observed for  $T_g^{(3)}$  phonon mode is  $-0.014 \text{ cm}^{-1}/\text{K}$  and the Raman peak is redshift by about  $7.39 \text{ cm}^{-1}$  in the temperature range from 77 to 500 K. Moreover, the anharmonic constant  $B$  is several times smaller than  $A$  constant, indicating that the probability of the three phonon process is greater than that of four phonon process.

Table 6.2 Fitting parameters for Raman shift [Eq. (1)] and linewidth [Eq. (2)] of cubic

(In<sub>0.83</sub>Ga<sub>0.17</sub>)<sub>2</sub>O<sub>3</sub> film.

Phonon modes	$A_g^{(1)}$	$A_g^{(2)}/T_g^{(2)}$
$\omega_0$ (cm <sup>-1</sup> )	135.5 ± 0.5	319.2 ± 0.6
$\chi$ (cm <sup>-1</sup> /K)	-0.017 ± 0.002	-0.024 ± 0.002
$\Gamma_0$ (cm <sup>-1</sup> )	20.341 ± 0.032	23.147 ± 1.564
$A$ (cm <sup>-1</sup> )	-0.0709 ± 0.0012	-0.0197 ± 0.0036
$B$ (cm <sup>-1</sup> )	-0.0205 ± 0.0025	-0.0068 ± 0.0011

Fig. 6.7 also shows the temperature-dependent Raman shifts and linewidths broadening of  $A_g^{(1)}$  and  $A_g^{(2)}/T_g^{(2)}$  phonon modes in (In<sub>0.83</sub>Ga<sub>0.17</sub>)<sub>2</sub>O<sub>3</sub> film as well as the fitting curves obtained by employing Eqs. (1) and (2). The fitting parameters  $\omega_0$ ,  $\chi$ ,  $\Gamma_0$ ,  $A$ , and  $B$  of these two modes are presented in Table 6.2. For (In<sub>0.83</sub>Ga<sub>0.17</sub>)<sub>2</sub>O<sub>3</sub> film, Raman shifts of  $A_g^{(1)}$  and  $A_g^{(2)}/T_g^{(2)}$  modes decrease by about 7.31 and 9.89 cm<sup>-1</sup> when temperature is increased from 77 to 500 K. The temperature coefficients of these two modes are 0.017 and 0.024 cm<sup>-1</sup>/K, which are several times larger than those of In<sub>2</sub>O<sub>3</sub> film. It indicates that these modes are more sensitive to the change of temperature than in the case of In<sub>2</sub>O<sub>3</sub> film because the more lattice defect and structural disorder are induced when Ga was implanted. The three phonon process dominates the line broadening of  $A_g^{(1)}$  and  $A_g^{(2)}/T_g^{(2)}$  modes in (In<sub>0.83</sub>Ga<sub>0.17</sub>)<sub>2</sub>O<sub>3</sub> film. However, in comparison with the cause of In<sub>2</sub>O<sub>3</sub> film, the ratios of  $A$  and  $B$  for  $A_g^{(1)}$  and  $A_g^{(2)}/T_g^{(2)}$  modes decrease, suggesting that the contribution from the four-phonon process increase after Ga implantation.

The detailed information of temperature coefficient for different Raman active modes is important in thermal metrology based on the Raman spectroscopy, which

was used for monitoring of local temperature of operating device.<sup>26</sup> Moreover, the information of the anharmonic effect is significant for the  $\text{In}_2\text{O}_3$ -based device applications, since the degree of lattice disorder in mirrors by Raman microprobe spectroscopy correlates to the strength of facet heating and to the power limit at optical mirror damage.<sup>29</sup>

### 6.3. Conclusions

The temperature-dependent Raman shifts and linewidths of six modes for  $\text{In}_2\text{O}_3$  and three modes for  $(\text{In}_{0.83}\text{Ga}_{0.17})_2\text{O}_3$  are analyzed. We noticed linear behavior of Raman shifts of phonon modes with temperature. Among modes in  $\text{In}_2\text{O}_3$  film, the most sensitive to the temperature is  $T_g^{(3)}$  mode with temperature coefficient of  $0.014 \text{ cm}^{-1}/\text{K}$ , while temperature coefficients of  $A_g^{(1)}$  and  $A_g^{(2)}/T_g^{(2)}$  modes in  $(\text{In}_{0.83}\text{Ga}_{0.17})_2\text{O}_3$  films are  $0.017$  and  $0.024 \text{ cm}^{-1}/\text{K}$ . Through the aid of a model involving three- and four-phonon coupling, the effects of temperature on linewidths are clearly illustrated. It is obvious that the three phonon process dominates in the decay process for all the modes of  $\text{In}_2\text{O}_3$  and  $(\text{In}_{0.83}\text{Ga}_{0.17})_2\text{O}_3$  films. These basic properties are very important for improving the quality of  $\text{In}_2\text{O}_3$  and  $(\text{In}_{0.83}\text{Ga}_{0.17})_2\text{O}_3$  films, which can be used as well and barrier layers in  $\text{In}_2\text{O}_3$ -based quantum well.

## References

- [1] P. D. C. King, T. D. Veal, D. J. Payne, A. Bourlange, R. G. Egdell, and C. F. McConville, *Phys. Rev. Lett.*, 101, 116808 (2008).
- [2] F. Yang, J. Ma, C. Luan, L. Kong, *Appl. Surf. Sci.*, 255, 4401 (2009).
- [3] Y. Kokubun, T. Abe, and S. Nakagomi, *Phys. Status Solidi A*, 207, 1741 (2010).
- [4] Z. Zhang, H. Wenckstern, J. Lenzner, M. Lorenz, and M. Grundmann, *Appl. Phys. Lett.*, 108, 123503 (2016).
- [5] F. Zhang, K. Satio, T. Tanaka, M. Nishio, Q. Guo, *J. Aollys Compd.*, 614, 173 (2014).
- [6] H. Peelaers, D. Steiauf, J. Varley, A. Janotti, and C. G. V. Walle, *Phys. Rev. B*, 92, 085206 (2015).
- [7] Y. Sui, Y. Yue, Y. Cao, B. Yao, X. Liu, J. Lang, M. Gao, X. Li, X. Li, and L. Yang, *Ceram. Int.*, 40, 9189 (2014).
- [8] X. Wang, K. Saito, T. Tanaka, M. Nishio, T. Nagaoka, M. Arita, and Q. Guo, *Appl. Phys. Lett.*, 107, 022111 (2015).
- [9] F. Zhang, K. Saito, T. Tanaka, M. Nishio, Q. Guo, *Solid State Commun.*, 186, 28 (2014).
- [10] C. Kranert, J. Lenzner, M. Jenderka, M. Lorenz, H. Wenckser, R. S. Grund, and M. Grundmann, *J. Appl. Phys.*, 87, 013505 (2000).
- [11] A. Regoutz, R. G. Egdell, D. J. Morgan, R. G. Palgrave, H. Tellez, S. J. Skinner, D. J. Payne, G. W. Watson, D. O. Scanlon, *Appl. Surf. Sci.*, 349, 970 (2015).

- [12] M. Balkanski, R. F. Wallis, and E. Haro, *Phys. Rev. B*, 28, 1928 (1983).
- [13] W. S. Li, Z. X. Shen, Z. C. Feng, and S. J. Chua, *J. Appl. Phys.*, 87, 3332 (2000).
- [14] X. Wang, K. Saito, T. Tanaka, M. Nishio, and Q. Guo, *J. Aollys Compd.*, 627, 383 (2015).
- [15] X. Wang, Z. Chen, F. Zhang, K. Satio, T. Tanaka, M. Nishio, and Q. Guo, *AIP Adv.*, 6, 015111 (2016).
- [16] J. Bai, T. Wang, and S. Sakai, *J. Appl. Phys.*, 88, 4729 (2000).
- [17] T. Makino, K. Tamura, C. H. Chia, Y. Segawa, M. Kawasaki, and A. Ohtomo, *Appl. Phys. Lett.*, 81, 2355 (2002).
- [18] Q. Guo, M. Nada, Y. Ding, T. Tanaka, and M. Nishio, *J. Appl. Phys.*, 107, 123525 (2010).
- [19] J. Qi, J. F. Liu, Y. He, W. Chen, and C. Wang, *J. Appl. Phys.*, 109, 063520 (2011).
- [20] B. G. Domene, H. M. Ortiz, O. Gomis, J. A. Sans, and F. J. Manjon, *J. Appl. Phys.*, 112, 123511 (2012).
- [21] X. Wang, Z. Chen, F. Zhang, K. Saito, T. Tanaka, M. Nishio, T. Nagaoka, and Q. Guo, *Ceram. Int.*, 42, 12783 (2016).
- [22] A. Baszczuk, M. Jasiorshi, M. Nyk, J. Hanuza, M. Maczka, and W. Strek, *J. Alloy. Compd.*, 394, 88 (2005).
- [23] O. M. Berengue, A. D. Rodrigues, C. J. Dalmaschio, A. J. C. Lanfredi. E. R. Leite, and A. J. Chiquito, *J. Phys. D: Appl. Phys.*, 43, 045401 (2010).
- [24] J. Gan, X. Lu, J. Wu, S. Xie, T. Zhai, M. Yu, Z. Zhang, Y. Mao, S. C. Wang. Y. Shen, and T. Tong, *Sci. Rep.*, 3, 1021 (2013).

- [25] C. Smit, R. A. C. M. M. van Swaaij, H. Donker, A. M. H. N. Petit, W. M. M. Kessels and M. C. M. van de Sanden, *J. Appl. Phys.*, 87, 3582 (2003).
- [26] A. Taube, A. Lapinska, J. Judek, and M. Zdrojek, *Appl. Phys. Lett.*, 107, 013105 (2015).
- [27] J. Jimenez, E. Martin, and A. Torres, and J. P. Landesman, *Phys. Rev. B*, 58 10463 (1998).
- [28] I. Calizo, A. A. Balandin, W. Bao, F. Miao, and C. N. Lau, *Nano Lett.*, 7, 2645 (2007).
- [29] J. Kong, W. Shen, Y. Zhang, X. Li, and Q. Guo, *Solid State Commun.*, 149, 10 (2009).

## Chapter 7

### Summary

Wide bandgap oxide semiconductor has attracted considerable attention owing to its application in ultraviolet (UV) optoelectronic devices, especially in deep UV light emitters and detectors, due to their potential application in Ozone hole detection, chemical-biological agent sensors, missile plume sensors and space-to-space communications. Among all the wide bandgap oxide semiconductors, MgZnO, (AlGa)<sub>2</sub>O<sub>3</sub>, and (InGa)<sub>2</sub>O<sub>3</sub> alloy films are ideal materials for developing the deep UV optoelectronic devices because of their wide bandgap.

In Chapter 1, the review of studies on wide bandgap oxide semiconductor was described. The purpose of this study was also presented.

In Chapter 2, film growth and characterization methods were introduced.

In Chapter 3, we have investigated the effect of the oxygen pressure, growth temperature and substrate on the crystal structure and properties of MgZnO films grown by using pulsed laser deposition (PLD) method. The influence of Mg content was also been discussed. Single phase MgZnO films were successfully obtained in all Mg content. The structural transition from hexagonal to cubic phase has been observed at the Mg content around 0.4. Optical analysis indicated that the bandgap of the MgZnO films could be tailored by controlling the Mg content in the films.

In Chapter 4, We reported on bandgap bowing parameters for wurtzite and cubic MgZnO alloys from a study of high quality and single phase films in all Mg content

range. The Mg contents in the MgZnO films were accurately determined using the Energy dispersive spectrometer and X-ray photoelectron spectroscopy (XPS). The measurement of bandgap energies by examining the onset of inelastic energy loss in core-level atomic spectra from XPS was proved to be valid for determining the bandgap of MgZnO films. The dependence of the energy bandgap on Mg content was found to deviate downwards from linearity. Fitting of the bandgap energies resulted in two bowing parameters of 2.01 and 1.48 eV corresponding to wurtzite and cubic MgZnO films, respectively.

In Chapter 5, (1)  $(\text{AlGa})_2\text{O}_3$  thin films were deposited on (0001) sapphire substrates by pulsed laser deposition at different substrate temperatures. The influence of substrate temperature on surface morphology, optical properties, and crystal quality has been systematically investigated by atomic force microscope, transmission spectra, X-ray diffraction, and Raman spectroscopy. The results revealed that all the  $(\text{AlGa})_2\text{O}_3$  films had smooth surface and high transmittance. The  $(\text{AlGa})_2\text{O}_3$  film with the better crystal quality can be obtain at a substrate temperature of 400 °C. (2) We also report a detailed investigation on temperature-dependent Raman scattering of  $\beta$ - $(\text{AlGa})_2\text{O}_3$  thin films with different Al content (0-0.72) under the temperature range of 77-300 K. The temperature-dependent Raman shifts and linewidths of the phonon modes were obtained by employing Lorentz fitting. The linewidths broadening of phonon modes with the temperature can be well explained by a model involving the effects of thermal expansion, lattice-mismatch-induced strain, and decay of optical phonon into two and three phonons. It is clearly demonstrated dependence of the

linewidths and decay process on the Al content in  $\beta$ -(AlGa)<sub>2</sub>O<sub>3</sub> thin films.

In Chapter 6, we reported the measurements of Raman scattering of cubic In<sub>2</sub>O<sub>3</sub> and (In<sub>0.83</sub>Ga<sub>0.17</sub>)<sub>2</sub>O<sub>3</sub> films grown on sapphire substrates by pulsed laser deposition as a function of temperature (77-500 K). We analyzed the temperature-dependent Raman shifts and linewidths of six Raman modes in In<sub>2</sub>O<sub>3</sub> film and  $A_g^{(1)}$  and  $A_g^{(2)}/T_g^{(2)}$  modes in (In<sub>0.83</sub>Ga<sub>0.17</sub>)<sub>2</sub>O<sub>3</sub> film. The Raman shifts of phonon modes were found to vary linearly with temperature. The temperature coefficients for six Raman modes of In<sub>2</sub>O<sub>3</sub> film were in the range of -0.014 and -0.006 cm<sup>-1</sup>/K, while temperature coefficients of  $A_g^{(1)}$  and  $A_g^{(2)}/T_g^{(2)}$  modes in (In<sub>0.83</sub>Ga<sub>0.17</sub>)<sub>2</sub>O<sub>3</sub> film were -0.017 and -0.024 cm<sup>-1</sup>/ K, respectively. Through the aid of a model involving three- and four-phonon coupling, the effects of temperature on linewidths were clearly illustrated, which demonstrated that three-phonon process always dominated in the decay process for all the modes in both In<sub>2</sub>O<sub>3</sub> and (In<sub>0.83</sub>Ga<sub>0.17</sub>)<sub>2</sub>O<sub>3</sub> films.

## **Acknowledgements**

Grateful acknowledgement is made to my supervisor Professor Qixin Guo who gave me considerable help by means of suggestion, comments and criticism. His encouragement and unwavering support has sustained me through frustration and depression. Without his pushing me ahead, the completion of this thesis would be impossible.

I also owe a special debt of gratitude to Professor Mitsuhiro Nishio, Professor Tooru Tanaka, and Doctor Katsuhiko Saito for their help on the discussions and experiments. I also would like to show my deepest gratitude to Professor Kazutoshi Takahashi for his help on the review and revise of this dissertation.

I want to express my thanks to Doctor Fabi Zhang and Doctor Zhengwei Chen for their helps. I also would like to express my gratitude to Doctor Makoto Arita and Doctor Takashi Nagaoka in Kyushu University.

## List of publications

### A Original paper related to this dissertation

1. **X. Wang**, Z. Chen, K. Satio, T. Tanaka, M. Nishio, Q. Guo, Temperature-dependent Raman scattering in cubic (InGa)<sub>2</sub>O<sub>3</sub> thin films, Journal of Alloys and Compounds, 690 (2017) 287-292.
2. **X. Wang**, Z. Chen, F. Zhang, K. Satio, T. Tanaka, M. Nishio, Q. Guo, Influence of substrate temperature on the properties of (AlGa)<sub>2</sub>O<sub>3</sub> thin films prepared by pulsed laser deposition, Ceramics International, 42 (2016) 12783-12788.
3. **X. Wang**, Z. Chen, K. Satio, T. Tanaka, M. Nishio, Q. Guo, Temperature dependence Raman scattering in  $\beta$ -(AlGa)<sub>2</sub>O<sub>3</sub> thin films, AIP advances, 6 (2016) 015111.
4. **X. Wang**, K. Satio, T. Tanaka, M. Nishio, T. Nagaoka, Makoto Arita, Q. Guo, Energy band bowing parameter in MgZnO alloys, Applied Physics Letters, 107 (2015) 022111.
5. **X. Wang**, K. Satio, T. Tanaka, M. Nishio, Q. Guo, Lower temperature growth of single phase MgZnO films in all Mg content range, Journal of Alloys and Compounds, 627 (2015) 383-387.

## **B Original papers on other subjects**

1. F. Zhang, M. Arita, **X. Wang**, Z. Chen , K. Saito, T. Tanaka, M. Nishio, T. Motooka, Q. Guo, Toward controlling the carrier density of Si doped Ga<sub>2</sub>O<sub>3</sub> films by pulsed laser deposition, Applied Physics Letters, in press, 2016.
2. Z. Chen, K. Nishihagi, **X. Wang**, K. Saito , T. Tanaka , M. Nishio , M. Arita , Q. Guo, Band alignment of Ga<sub>2</sub>O<sub>3</sub>/Si heterojunction interface measured by X-ray photoelectron spectroscopy, Applied Physics Letters, in press, 2016.
3. Z. Chen, **X. Wang**, F. Zhang, S. Noda, K. Saito , T. Tanaka , M. Nishio , M. Arita , Q. Guo, Observation of low voltage driven green emission from erbium doped Ga<sub>2</sub>O<sub>3</sub> light-emitting devices, Applied Physics Letters, 109 (2016) 022107.
4. Z. Chen, **X. Wang**, F. Zhang, S. Noda, K. Saito , T. Tanaka , M. Nishio , M. Arita , Q. Guo, Temperature dependence of luminescence spectra in europium doped Ga<sub>2</sub>O<sub>3</sub> film, Journal of Luminescence, 177 (2016) 48-53.
5. Z. Chen, **X. Wang**, S. Noda, K. Saito , T. Tanaka , M. Nishio , M. Arita , Q. Guo, Effects of dopant contents on structural, morphological and optical properties of Er doped Ga<sub>2</sub>O<sub>3</sub> films, Superlattices and Microstructures, 90 (2016) 207-214.

6. X.H. Wang, L.Q. Huang, L.J. Niu, R.B. Li, D.H. Fan, F.B. Zhang, Z.W. Chen, **X. Wang** and Q.X. Guo, The impacts of growth temperature on morphologies, compositions and optical properties of Mg-doped ZnO nanomaterials by chemical vapor deposition, *Journal of Alloys and Compounds*, 622 (2015) 440-445.